TOWARDS FAST COHERENT ANTI-STOKES RAMAN SCATTERING MICROSPECTROSCOPY

A Dissertation

by

YUJIE SHEN

Submitted to the Office of Graduate and Professional Studies of
Texas A&M University
in partial fulfillment of the requirements for the degree of

DOCTOR OF PHILOSOPHY

Chair of Committee,	Marlan O. Scully
Co-Chair of Committee,	Alexei V. Sokolov
Committee Members,	Edward S. Fry
	Philip Hemmer
	Aleksei M. Zheltikov
	Vladislav V. Yakovlev
Head of Department,	Grigory Rogachev

December 2018

Major Subject: Physics

ABSTRACT

Coherent anti-Stokes Raman scattering (CARS) microspectroscopy is a nonlinear spectroscopy and imaging technique that probes the vibrational and rotational modes of the molecule, enabling chemical-selective microscopy. Over the past years, CARS has found applications in a wide range of fields such as tumor imaging, gas sensing, and flow cytometry. More recently, commercial components and even a microscopic solution dedicated to CARS has become available. This research is devoted to the development of a high-speed, high-sensitivity CARS microspectroscopy system for chemical and biomedical analysis.

We started with an easy-to-implement CARS scheme based on ultrafast pulse shaping of single laser beam. We demonstrated an improved setup that achieved higher epi-detection efficiency as compared to earlier experiment, and allowed low-wavenumber Raman band detection below 100 cm^{-1}. We further simplified our setup by adopting a folded pulse-shaper design, and incorporated the femtosecond adaptive spectroscopic technique (FAST) developed earlier in the group to achieve versatile single-beam CARS detection with significant nonresonant background suppression. Finally, through utilizing the phase information contained in the signal, we devised and implemented an upgraded system by adopting heterodyne detection in the single-beam CARS setup to achieve high speed spectral detection with background suppression. We have also combined spectral detection and pulse shaping in the setup so as to achieve a one-box-solution for CARS measurement.

To further extend the Raman detection range, it is necessary to incorporate means of wavelength extension to achieve broadband excitation. We studied the supercontinuum (SC) generation in large mode area photonic crystal fiber pumped by an industrial picosecond laser. Such an extension unit allowed a simultaneous Raman excitation bandwidth of over 3000 cm^{-1}. We built a multiplex CARS system based on this SC source, and demonstrated its applicability through imaging standard samples. We further constructed a laser-scanning CARS microscope that can provide high spectral resolution and acquisition speed, and showed its capability in 3-dimensional scanning CARS microscopy.

In order to boost CARS imaging speed, we also experimented with the wide-field CARS scheme, in which CARS excitation was performed over a large area simultaneously. Using the high-power SC source, we combined the wide-field CARS with multiplex CARS excitation scheme, such that a broad range of Raman modes over a significant spatial region were excited, and CARS image was obtained by applying a corresponding filter. We showed chemical-selective imaging using standard polymer microsphere samples, and demonstrated video-rate CARS microscopy using this setup.

DEDICATION

To my parents.

ACKNOWLEDGMENTS

During the past seven years here at Texas A&M, I have learned a great deal both in and out of my professional study, and have developed necessary skills that helped preparing me for my future career. Of course, this could not have been possible without the assistance from the many wonderful people around me.

My deepest gratitude goes to my thesis advisor, and my committee chair Prof. Marlan Scully. He was my hero since my college time, when I first learned quantum optics using his well-known textbook. His enthusiasm and ingenuity have always been the spiritual inspiration in my research, and his wisdom and support have guided me along my PhD path. I would also like to thank Prof. Alexei Sokolov. He was my mentor in experimental physics, and I am grateful for his assistance in both my experiments and my career path. In addition, I want to thank the rest of my committee members: Prof. Aleksei Zheltikov, Prof. Vladislav Yakovlev, Prof. Philip Hemmer and Prof. Edward Fry, for their support during my research and inspiring discussions during my course of study, which are indispensable factors in the completion of my degree.

My gratitude also goes to my colleagues. Dr. Dmitri Voronine and Dr. Alexander Sinyukov had introduced me to the basement lab in the MPHY building, and had offered great help in my research these years. I have also learned a lot from Dr. Zhenhuan Yi, Dr. Xia Hua, Dr. Miaochan Zhi, Dr. Kai Wang, and Dr. Feng Zhu, and would like to thank them for the great discussions and collaborations. Moreover, I am grateful for the working experience with Dr. Jonathan Thompson, Dr. Alexandra Zhdanova, Dr. Tao Peng, Zehua Han, Anton Shutov, Mariia Shutova, Jizhou Wang, Zhe He, Aysan Bahari, Fu Li and Xingchen Zhao. The time in the lab will always be something to cherish.

Furthermore, I would like to thank the members at IQSE: Dr. Anatoly Svidzinsky, Dr. Luqi Yuan, Dr. Ziyun Di, Dr. Charles Ballman, Dr. Dawei Wang, Dr. Ben Stryker, Dr. Han Cai, Dr. Ariunbold Gombojav, Dr. Narangerel Altangerel, and many others for their help in life and

research. Thanks to Dr. Alexander Voronin for his assistance in fiber simulations, and to Prof. Zhengrong Zhang and Prof. Howard Lee for the collaborations on our Raman and CARS projects.

Last but not least, many thanks to the staff at IQSE, especially to Kim Chapin, for their wonderful work and great assistance, without which our researches could not have happened. I would also like to thank the staff at the department of physics, the physics machine shop, and the physics electronics shop, for their support and guidance. Finally, thanks to Dr. Chen Sun, Zhidong Yang, Minjie Lu, and many other Aggies for making my life here enjoyable.

CONTRIBUTORS AND FUNDING SOURCES

Contributors

This work was supported by a dissertation committee consisting of Professors Marlan O. Scully, Alexei V. Sokolov, Edward S. Fry, and Aleksei M. Zheltikov of the Department of Physics and Astronomy, and Professor Philip Hemmer of the Department of Electrical and Computer Engineering, and Professor Vladislav V. Yakovlev of the Department of Biomedical Engineering.

The theoretical simulation in Chapter 4 was provided by Doctor Alexander A. Voronin of the Russian Quantum Center and Professor Aleksei M. Zheltikov. The nanodiamond samples used in Chapter 4 and Chapter 5 were provided by Professor Philip Hemmer's group.

All other work conducted for the dissertation was completed by the student independently.

Funding Sources

Graduate study was supported by the Herman F. Heep and Minnie Belle Heep Texas A&M University Endowed Fund held/administered by the Texas A&M Foundation.

NOMENCLATURE

PMT	Photomultiplier tube
CCD	Charge-coupled device
SERS	Surface enhanced Raman spectroscopy
CARS	Coherent anti-Stokes Raman scattering
N.A.	Numerical aperture
FWM	Four-wave mixing
NIR	Near infrared
SC	Supercontinuum
PCF	Photonic crystal fiber
CMOS	Complementary metal-oxide-semiconductor
OPA	Optical parametric amplifier
FAST	Femtosecond adaptive spectroscopic technique
LO	Local oscillator
LMA	Large-mode area
SLM	Spatial light modulator
LCM	Liquid crystal modulator
AOM	Acousto-optic modulator
DM	Deformable mirror
RF	Radio frequency
FWHM	Full width half maximum
ND	Neutral density
CCl_4	Carbon tetrachloride

TeCA	1,1,2,2-tetrachloroethane
MoS_2	Molybdenum disulfide
CM	Concave mirror
DQSI	Double quadrature spectral interferometry
PMMA	Poly(methyl methacrylate)
ZDW	Zero dispersion wavelength
GVD	Group velocity dispersion
PS	Polystyrene
SNR	signal-to-noise ratio
LDPE	Low-density polyethylene
PET	Polyethylene terephthalate
SPM	self phase modulation
HC	Hollow-core

TABLE OF CONTENTS

Page

LIST OF FIGURES

FIGURE Page

LIST OF TABLES

TABLE Page

1. INTRODUCTION: FROM SPONTANEOUS RAMAN SCATTERING TO COHERENT RAMAN SCATTERING

1.1 Spontaneous Raman scattering spectroscopy and applications

During his trip through the Mediterranean sea in 1921, C. V. Raman proposed that sunlight scattered from the ocean contained, besides the normal elastic Rayleigh scattering, an additional portion that arose from the water molecules [1]. Over the next seven years, Raman and his students had conducted theoretical as well as experimental investigations on this scattering phenomenon, and had published the well-known Nature paper in 1928 [2]. An interesting fact is that during the same time, other groups of scientists around the world had also worked on the same problem, including the theoretical works done by Smekal [3] and Rocard [4], and the experimental demonstrations by Cabannes [5] and Mandelstam [6]. Raman was soon awarded the Nobel Prize for his contribution, and the newly discovered effect was named after him. Numerous studies were conducted in the following decades, with more than 2500 chemical compounds tested using the new Raman spectroscopy [1]. Still, the Raman scattering is in general much feebler than Rayleigh scattering [7], with approximately 1 in 10^7 incident photons being scattered due to the Raman effect. Therefore, further development of Raman spectroscopy for chemical analysis was hindered until the advent of laser technology [8, 9].

In 1961, the first laser-based Raman spectroscopy experiment was demonstrated [10], and since then the practice of Raman spectroscopy had been revolutionized. Benefiting from the high brightness of the powerful laser sources, improved efficiency of the spectrograph, and development of sensitive detectors like photomultiplier tube (PMT) and charge-coupled device (CCD) [11], there had been an upsurge in applying the Raman spectroscopy to biochemical research [12, 13]. Moreover, advancement in technologies had led to novel schemes in implementing Raman spectroscopy, such as Fourier transform Raman, resonance Raman, and surface enhanced Raman spectroscopy (SERS) [14]. Also, Raman spectroscopy was combined with high-resolution microscopy tools

to achieve Raman microspectroscopy and confocal Raman microscopy, enabling the detection of chemical distribution and dynamics at the microscopic scale [15, 16]. Commercial benchtop Raman systems had also become available since the 90s [11]. Nowadays, Raman spectroscopy has been applied to a variety of disciplines. Examples include structure determination and active substance identification in drug analysis [17], characterization of 2D materials [18], mapping mineral phases in petrographic analysis [19], study of pigments and dyes on historical art works [20], and even chemical analysis in outer space projects [21].

Besides molecular sensitivity, there are other advantages that make Raman spectroscopy a popular technology. It is intrinsically noninvasive, and the excitation laser wavelength can be chosen to minimize damage to samples like cells and tissues. By using visible or near infrared lasers, the examination spot can be focused down to sub-micron level, enabling microspectroscopy of tiny structures. Also, unlike IR spectroscopy, Raman spectroscopy is capable of analyzing aqueous solution, as water does not present significant signals or absorption. Last but not least, the implementation of Raman spectroscopy has been greatly facilitated thanks to the advancement in lasers and optics. A common Raman spectroscopy setup includes: an excitation laser, optional light focusing and collection element, a spectrograph, and a multichannel detector. These can be configured into a high-end table-top microscope system that provides excellent spectral and spatial resolution, or into a handheld system with a high degree of integration that can be applied for field analysis [11, 15, 22]. Figures 1.1a and 1.1b are pictures showing the latest commercial table-top and handheld Raman systems, respectively.

But even with the assistance of lasers, the low scattering cross-section of the spontaneous Raman effect still requires in relatively long integration time on the detector, typically from seconds to hours. Techniques like line-scanning or wide-field imaging have been applied to improve the throughput, yet they suffer from other problems like field-curvature artifacts and spatial resolution, and the imaging speed is still not enough for most clinical applications [23]. Another major drawback of the spontaneous Raman spectroscopy is the commonly-presented fluorescent background, which is often strong and therefore veils the weak Raman signals— especially when detecting

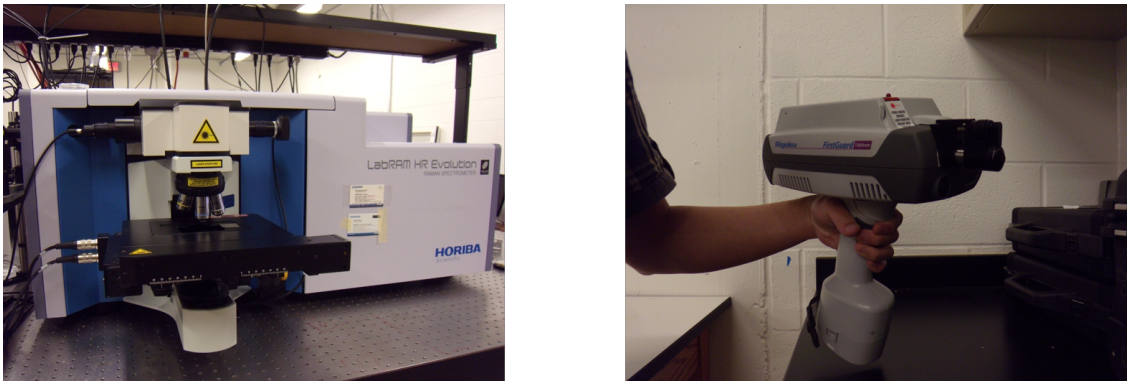

Figure 1.1: Commercial (a) table-top (LabRAM HR Evolution, Horiba) and (b) handheld (First-Guard, Rigaku) Raman systems.

samples with complicated molecular structures such as biological cells and tissues. Therefore, people started researching on other methods that can overcome these issues, such as plasmonic enhancement and nonlinear Raman techniques.

1.2 Coherent anti-Stokes Raman scattering

1.2.1 Brief review

Coherent anti-Stokes Raman scattering (CARS) was first reported in 1965 by Maker and Terhune at the Ford Motor Company [24]. They observed a blue-shifted signal generated in benzene when tuning the two incident lasers such that their frequency difference matched the benzene Raman mode. However, the more commonly used acronym 'CARS' was not coined until a decade later [25, 26]. A CARS-based microscope was demonstrated in 1982 [27], followed by a few other CARS implementations in the following years [28, 29, 30], but further adoption of the technology by the wider scientific society was hindered due to the limitation in laser technology at the time, as well as the complication in satisfying phase-matching condition in the target sample.

It was not until 1999 when Zumbusch and Xie demonstrated that phase-matching condition could be satisfied under tight-focusing using high numerical aperture (N.A.) objective [31]. Together with the advancement in ultrafast laser technologies, CARS microspectroscopy has become

practical and popular, and the following decade had witnessed an astonishing growth of the field. On one hand, novel schemes continued to expand the technology— improving the detection range [32, 33, 34], enhancing the signal level and pushing the acquisition rate to the limit [35, 36, 37], and in the meantime suppressing the unwanted background signals [38, 39, 40]. On the other hand, CARS has found applications in a wide range of studies, such as biochemical imaging of cells and tissues [41], gas-phase analysis [42], and characterization of new materials [43]. Some excellent review articles that focused on the implementations and applications of the technology are available for further reading [44, 45].

1.2.2 Theoretical treatment

CARS is a third-order nonlinear process, and is a special type of four-wave mixing (FWM) process. In the following, we will follow a perturbative treatment of the CARS process [46]. This assumes the excitation field are much weaker than the molecular binding field, otherwise a non-perturbative deduction is required [47]. From the semi-classical nonlinear optics theory, the density matrix equation can be written as:

$$\frac{d\rho_{nm}}{dt} = \frac{-i}{\hbar}[\hat{H}, \hat{\rho}]_{nm} - \gamma_{nm}\left(\rho_{nm} - \rho_{nm}^{\text{eq}}\right). \tag{1.1}$$

Here ρ_{nm} represents the entry of the density matrix $\hat{\rho}$ of the target system, and $\hat{H}$ is the Hamiltonian that indicates system evolution and interaction with external fields. We have also added a phenomenological damping term, with γ_{nm} being the decay rate and ρ_{nm}^{eq} the entry value at equilibrium. We assume that $\gamma_{nm} = \gamma_{mn}$, and $\rho_{nm}^{\text{eq}} = 0$ for $n \neq m$. Then we can write the external-field-interaction as a perturbation term in the Hamiltonian:

$$\hat{H} = \hat{H}_0 + \hat{V}(t) = \hat{H}_0 - \vec{\mu} \cdot \vec{E}(t), \tag{1.2}$$

where $\vec{\mu}$ is the dipole operator and $\vec{E}(t)$ is the external field. Denoting the internal energy levels of the target sample as E_i, we have, for the unperturbed Hamiltonian $\hat{H}_0$:

$$[\hat{H}_0, \hat{\rho}]_{nm} = \left(\hat{H}_0\hat{\rho} - \hat{\rho}\hat{H}_0\right)_{nm} = (E_n - E_m)\,\rho_{nm}. \tag{1.3}$$

Further, we denote the transition frequency $\omega_{nm} = \frac{E_n - E_m}{\hbar}$, then Eq. 1.1 can be written as:

$$\frac{d\rho_{nm}}{dt} = -i\omega_{nm}\rho_{nm} - \frac{i}{\hbar}\sum_s \left(V_{ns}\rho_{sm} - \rho_{ns}V_{sm}\right) - \gamma_{nm}\left(\rho_{nm} - \rho_{nm}^{\text{eq}}\right). \tag{1.4}$$

Following the perturbation theory, we expand the density matrix as $\hat{\rho} = \hat{\rho}^{(0)} + \hat{\rho}^{(1)} + \hat{\rho}^{(2)} + ...$, with the superscript number representing the order of perturbation. Therefore the evolution of the density matrix can be separated according to this order:

$$\frac{d\rho_{nm}^{(0)}}{dt} = -i\omega_{nm}\rho_{nm}^{(0)} - \gamma_{nm}\left(\rho_{nm}^{(0)} - \rho_{nm}^{\text{eq}}\right), \tag{1.5}$$

$$\frac{d\rho_{nm}^{(1)}}{dt} = -\left(i\omega_{nm} + \gamma_{nm}\right)\rho_{nm}^{(1)} - \frac{i}{\hbar}[\hat{V}, \hat{\rho}^{(0)}]_{nm}, \tag{1.6}$$

$$\frac{d\rho_{nm}^{(2)}}{dt} = -\left(i\omega_{nm} + \gamma_{nm}\right)\rho_{nm}^{(2)} - \frac{i}{\hbar}[\hat{V}, \hat{\rho}^{(1)}]_{nm}, \tag{1.7}$$

$$\frac{d\rho_{nm}^{(3)}}{dt} = -\left(i\omega_{nm} + \gamma_{nm}\right)\rho_{nm}^{(3)} - \frac{i}{\hbar}[\hat{V}, \hat{\rho}^{(2)}]_{nm}. \tag{1.8}$$

Ignoring the zeroth-order effect and set $\rho_{nm}^{(0)} = \rho_{nm}^{\text{eq}}$, we can reach a solution for the first order perturbation by integrating both sides of Eq. 1.6:

$$\rho_{nm}^{(1)}(t) = \int_{-\infty}^{t} \frac{-i}{\hbar}[\hat{V}(t'), \hat{\rho}^{(0)}]_{nm} e^{(i\omega_{nm} + \gamma_{nm})(t'-t)} dt'. \tag{1.9}$$

Expressing the interaction term as $V_{ns}(t) = \mu_{ns} \cdot \tilde{E}(t)$, the above integration can be carried out and simplified:

$$\rho_{nm}^{(1)}(t) = \frac{\rho_{mm}^{(0)} - \rho_{nn}^{(0)}}{\hbar} \sum_s \frac{\vec{\mu}_{nm} \cdot \vec{E}(\omega_s) e^{-i\omega_s t}}{(\omega_{nm} - \omega_s) - i\gamma_{nm}}, \tag{1.10}$$

where we have assumed the external field has a discrete spectrum $\vec{E}(t) = \sum_s \vec{E}(\omega_s) e^{-i\omega_s t}$. Then,

by using the polarizability relation $\vec{P} = N\text{tr}(\vec{\mu}\hat{\rho}) = \epsilon_0\vec{\chi}^{(1)} \cdot \vec{E}$, we can obtain the susceptibility tensor as:

$$\chi_{ij}^{(1)}(\omega_s) = \frac{N}{\epsilon_0\hbar}\sum_{nm}\left(\rho_{mm}^{(0)} - \rho_{nn}^{(0)}\right)\frac{\mu_{mn}^i\mu_{nm}^j}{(\omega_{nm} - \omega_s) - i\gamma_{nm}}. \tag{1.11}$$

In a similar fashion, the second-order density matrix element can be calculated:

$$\begin{aligned}\rho_{nm}^{(2)}(t) =& \sum_l\sum_{rs} e^{-i(\omega_r+\omega_s)t}\left\{\frac{\rho_{mm}^{(0)} - \rho_{ll}^{(0)}}{\hbar^2}\frac{[\vec{\mu}_{nl}\cdot\vec{E}(\omega_s)][\vec{\mu}_{lm}\cdot\vec{E}(\omega_r)]}{[(\omega_{nm} - \omega_r - \omega_s) - i\gamma_{nm}][(\omega_{lm} - \omega_r) - i\gamma_{lm}]}\right. \\ &\left. - \frac{\rho_{ll}^{(0)} - \rho_{nn}^{(0)}}{\hbar^2}\frac{[\vec{\mu}_{nl}\cdot\vec{E}(\omega_s)][\vec{\mu}_{lm}\cdot\vec{E}(\omega_r)]}{[(\omega_{nm} - \omega_r - \omega_s) - i\gamma_{nm}][(\omega_{nl} - \omega_r) - i\gamma_{nl}]}\right\} \\ \equiv& \sum_l\sum_{rs} K_{nml}^{rs}e^{-i(\omega_r+\omega_s)t},\end{aligned} \tag{1.12}$$

and for the third-order:

$$\begin{aligned}\rho_{nm}^{(3)}(t) =& \frac{1}{\hbar}\sum_{lk}\sum_{rsq} e^{-i(\omega_r+\omega_s+\omega_q)t}\left\{\frac{[\vec{\mu}_{nl}\cdot\vec{E}(\omega_q)]K_{lmk}^{rs}}{(\omega_{nm} - \omega_r - \omega_s - \omega_q) - i\gamma_{nm}}\right. \\ &\left. - \frac{[\vec{\mu}_{lm}\cdot\vec{E}(\omega_q)]K_{nlk}^{rs}}{(\omega_{nm} - \omega_r - \omega_s - \omega_q) - i\gamma_{nm}}\right\}.\end{aligned} \tag{1.13}$$

This leads to a lengthy expression for the third-order nonlinear susceptibility:

$$\begin{aligned}&\chi_{ijkl}^{(3)}(\omega_r + \omega_s + \omega_q; \omega_r, \omega_s, \omega_q) = \frac{N}{\epsilon_0\hbar^3}\text{PM}\sum_{nmpv} \\ &\left\{\frac{(\rho_{mm}^{(0)} - \rho_{vv}^{(0)})\mu_{mn}^i\mu_{np}^j\mu_{pv}^k\mu_{vm}^l}{[(\omega_{nm} - \omega_r - \omega_s - \omega_q) - i\gamma_{nm}][(\omega_{pm} - \omega_r - \omega_s) - i\gamma_{pm}][(\omega_{vm} - \omega_r) - i\gamma_{vm}]}\right. \\ &- \frac{(\rho_{vv}^{(0)} - \rho_{pp}^{(0)})\mu_{mn}^i\mu_{np}^j\mu_{vm}^k\mu_{pv}^l}{[(\omega_{nm} - \omega_r - \omega_s - \omega_q) - i\gamma_{nm}][(\omega_{pm} - \omega_r - \omega_s) - i\gamma_{pm}][(\omega_{pv} - \omega_r) - i\gamma_{pv}]} \\ &- \frac{(\rho_{pp}^{(0)} - \rho_{vv}^{(0)})\mu_{mn}^i\mu_{pm}^j\mu_{nv}^k\mu_{vp}^l}{[(\omega_{nm} - \omega_r - \omega_s - \omega_q) - i\gamma_{nm}][(\omega_{np} - \omega_r - \omega_s) - i\gamma_{np}][(\omega_{vp} - \omega_r) - i\gamma_{vp}]} \\ &\left. + \frac{(\rho_{pp}^{(0)} - \rho_{nn}^{(0)})\mu_{mn}^i\mu_{pm}^j\mu_{vp}^k\mu_{nv}^l}{[(\omega_{nm} - \omega_r - \omega_s - \omega_q) - i\gamma_{nm}][(\omega_{np} - \omega_r - \omega_s) - i\gamma_{np}][(\omega_{nv} - \omega_r) - i\gamma_{nv}]}\right\},\end{aligned} \tag{1.14}$$

in which the sign PM means a permutation over possible combinations of frequency indices r, s, and q, and in the meantime changing the Cartesian indices j, k, and l correspondingly. By splitting

the subtraction term containing $\rho^{(0)}$, this results in an expression with 48 different terms.

A simpler way to understand the CARS process is through the energy diagram plots: two photons with frequencies ω_{P} and ω_{pr} are absorbed, which are referred to as the pump and probe photon, respectively; and a photon with frequency ω_{S} is emitted, known as the Stokes photon. The emitted signal photon will have frequency $\omega_{\mathrm{as}} = \omega_{\mathrm{P}} - \omega_{\mathrm{S}} + \omega_{\mathrm{pr}}$. Such a process is characterized by the nonlinear susceptibility $\chi^{(3)}(\omega_{\mathrm{as}}; \omega_{\mathrm{P}}, -\omega_{\mathrm{S}}, \omega_{\mathrm{pr}})$, and Fig. 1.2 shows two diagrams indicating two different interaction paths. Figure 1.2a represents one possible path for the CARS process, in which the pump and the Stokes photon satisfy the resonance condition $\omega_{ig} - \omega_{\mathrm{P}} - \omega_{\mathrm{S}} = 0$ and the difference frequency addresses the vibrational level in the target. This will, in general, result in a resonance enhancement in the $\chi^{(3)}$ value, leading to a peak signal when tuning the difference frequency across the resonance. Note that there are other pathways that also lead to such resonance enhancement in CARS signals. On the other hand, Fig. 1.2b shows an example of a process that does not involve the lower vibrational levels, and will contribute as a background signal that does not show resonant peaks when tuning the difference frequency. The latter case is known as the nonresonant background. Similar graphic explanation using the double-sided Feymann diagram has also been demonstrated [44, 46].

For simplicity, we assume that all fields share the same polarization, and ignore the Cartesian indices. Also, we combine all the nonresonant path contributions and write it as one effective term in the susceptibility. Therefore the third-order susceptibility relating to the CARS process can be simplified as [44]:

$$\begin{aligned}\chi^{(3)}(\omega_{\mathrm{as}}; \omega_{\mathrm{P}}, -\omega_{\mathrm{S}}, \omega_{\mathrm{pr}}) &= \chi_{\mathrm{R}}(\omega_{\mathrm{as}}; \omega_{\mathrm{P}}, -\omega_{\mathrm{S}}, \omega_{\mathrm{pr}}) + \chi_{\mathrm{NR}}(\omega_{\mathrm{as}}; \omega_{\mathrm{P}}, -\omega_{\mathrm{S}}, \omega_{\mathrm{pr}}) \\ &= \sum_n \frac{A_n(\omega_{\mathrm{as}}; \omega_{\mathrm{P}}, -\omega_{\mathrm{S}}, \omega_{\mathrm{pr}})}{(\omega_{\mathrm{P}} - \omega_{\mathrm{S}}) - \Omega_n + i\gamma_n} + \chi_{\mathrm{NR}}(\omega_{\mathrm{as}}; \omega_{\mathrm{P}}, -\omega_{\mathrm{S}}, \omega_{\mathrm{pr}}).\end{aligned} \tag{1.15}$$

Here the first term χ_{R} represents the resonant contribution from the CARS process, and χ_{NR} is the nonresonant background. The sum in the χ_{R} term runs over all possible Raman modes, and Ω_n and γ_n are their corresponding frequencies and decay rates. As expected, we will see significant

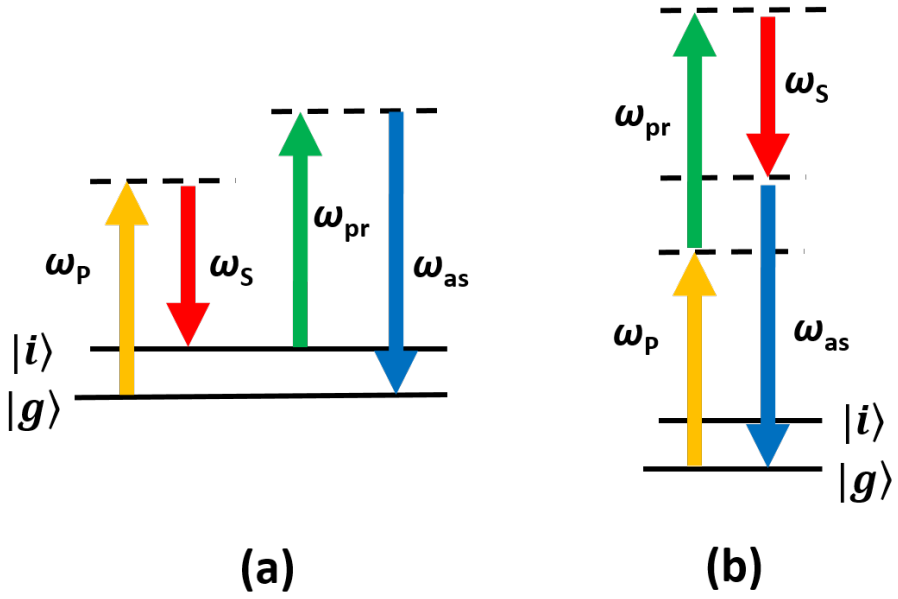

Figure 1.2: Energy diagrams corresponding to (a) coherent anti-Stokes Raman scattering (CARS) and (b) nonresonant background signal generation.

enhancement when the resonant condition $\omega_{\mathrm{P}} - \omega_{\mathrm{S}} = \Omega_n$ is met. The CARS signal is then given by [48]:

$$I_{\mathrm{CARS}}(\omega_{\mathrm{as}}) \propto \left| \iiint \chi^{(3)}(\omega_{\mathrm{as}}; \omega_{\mathrm{P}}, -\omega_{\mathrm{S}}, \omega_{\mathrm{pr}}) E_{\mathrm{P}}(\omega_{\mathrm{P}}) E_{\mathrm{S}}^{*}(\omega_{\mathrm{S}}) E_{\mathrm{pr}}(\omega_{\mathrm{pr}}) \times \delta(\omega_{\mathrm{as}} - \omega_{\mathrm{P}} + \omega_{\mathrm{S}} - \omega_{\mathrm{pr}}) d\omega_{\mathrm{P}} d\omega_{\mathrm{S}} d\omega_{\mathrm{pr}} \right|^2, \tag{1.16}$$

with $E_{\mathrm{P}}(\omega_{\mathrm{P}})$, $E_{\mathrm{S}}(\omega_{\mathrm{S}})$ and $E_{\mathrm{pr}}(\omega_{\mathrm{pr}})$ representing the pump, Stokes, and probe field, respectively. Therefore with given excitation field, we can calculate the CARS signal level. It is worth pointing out that typical CARS spectrum is different from the spontaneous Raman spectrum I_{Raman}, which satisfies $I_{\mathrm{Raman}} \propto \mathrm{Im}(\chi_{\mathrm{R}})$ to a first degree approximation [26]. Also note that we have neglected the coefficient arising from the phase-matching condition in Eq. 1.16, which can be obtained by solving the beam propagation equations [46]. A detailed treatment of the theory under tight-focusing condition can be found elsewhere [44].

1.2.3 Commonly used schemes

In the following we list some of the commonly adopted CARS microspectroscopy schemes according to earlier classification [45], and briefly explain their implementations.

Narrowband CARS

The narrowband CARS scheme employs a pair of laser oscillators with their output synchronized in time, producing two trains of narrowband picosecond pulses with negligible time jitter [49]. One is used as the degenerate pump and probe beam, and the other as the Stokes beam. The wavelength difference between the two beams is tunable, allowing the system to address different Raman bands. The two beams are combined to propagate collinearly and sent to the microscope, where they are focused onto the sample by a high N.A. objective lens. For transparent sample, forward scattered light is collected by another objective on the other side, while for opaque samples back scattered light is gathered by the same focusing objective. The collimated beam is sent to the detection element, typically a PMT, after passing a short-pass filter to get rid of the excitation light. Microscopy is achieved by collecting the scanning signal— either by moving the sample stage or by raster scanning the laser focus across the sample using galvonometric mirrors. Also, shifting the focus in the axial (z) direction allows depth-resolved three-dimensional imaging.

The major advantage of the narrowband CARS setup is its fast acquisition speed, allowing signal collection on the microsecond time scale, therefore enabling high-speed CARS imaging [35]. Another merit is the intrinsic high spectral resolution ($\sim$10 cm^{-1}) offered by the picosecond laser. Also, by using laser wavelength in the near infrared (NIR), deeper penetration into biological sample is possible, and less photo damage is imposed as compared to visible excitation. Dedicated objective can be chosen to offer high spatial resolution and sectioning capability thanks to the multiphoton nature of the CARS process. Such a setup has also been applied in stimulated Raman scattering microscopy [44], with additional components used to modulate the input pulses.

Still, there are several limitations coming with the scheme. First is that only one Raman band can be addressed at a time, and selective imaging of multiple bands requires tuning of the system,

during which instability and jitter arises. Secondly, separating the nonresonant background from the signal is difficult, therefore imaging are mostly done using the strong C-H stretching signals that suffer less distortion due to the background. Also, the complicated laser system and electronics are intimidating, in terms of both cost and maintenance, for users in other disciplines. There have been other modified schemes based on the narrowband excitation principle, such as polarization CARS [38], frequency modulation CARS [38], and heterodyne CARS [36]. These modifications provide solutions to the background issue, but impose further complications to the system.

Broadband CARS

Another widely adopted scheme, known as the broadband/multiplex CARS scheme, uses a broadband femtosecond laser instead of a narrowband picosecond laser to provide the Stokes beam. Detection is performed using a spectrometer with a multichannel detector like CCD camera. In this way a broad range of Raman bands can be stimulated and detected simultaneously, and scanning the laser focus results in a hyperspectral image in which each pixel contains the whole spectral information of the sample. The broadband pulse can be obtained directly from the laser, as in many single-beam CARS setups [50], which will be the subject of later chapters. It can also be obtained through wavelength extension methods, such as supercontinuum (SC) generation in photonic crystal fibers (PCF) [51]. Both methods eliminate the need for laser synchronization as in narrowband CARS system. Through broadband intrapulse excitation, both the fingerprint region and the C-H stretching region can be excited efficiently, resulting in a total detection bandwidth over 3000 cm^{-1} [37]. Another advantage of the broadband CARS scheme is the capability of extracting CARS signal from the background through post-processing methods employing maximum entropy [52] or Kramers-Kronig relation [53].

However, the unbalanced temporal durations of the picosecond pump/probe beam and the femtosecond Stokes beam in the multiplex CARS setup lead to less efficient generation of CARS signal as compared to the narrowband CARS scheme, resulting in a longer integration time, typically on the order of milliseconds [54]. Also, limitations in the CCD technology has also prevented the acquisition rate to go beyond kHz level— a problem that could be mitigated by the fast-growing

complementary metal-oxide-semiconductor (CMOS) imaging technology [55]. Moreover, the use of broadband light has imposed more restrictions on the optics, especially when using femtosecond pulses which requires careful dispersion control.

It is worth noting that narrowband excitation can also be achieved using femtosecond laser sources, through spectral focusing [56] or coherent control [50]. There have also been demonstrations of broadband CARS using all-fiber-based [54] or microchip laser sources, which are promising solutions for portable and robust CARS devices in the future.

Time and frequency domain CARS

The time-domain CARS technique relies on the temporal characteristic of the CARS signal generation— while nonresonant background signal is instantly generated during the overlapping period between the excitation pulses, the CARS process allows certain coherence lifetime depending on the decay term γ_{nm} in Eq. 1.1, and therefore CARS signal shows different decay curve as compared to the nonresonant background when changing the relative delay between the pulses. A time-resolved CARS scheme utilizing this characteristic was first demonstrated using an amplified Ti:Sapphire laser and an optical parametric amplifier (OPA), in which the wavelength of the two output pulses are tuned to match a specific Raman resonance of the sample, and the delay between the pulses was scanned to record time-dependent CARS signal [57]. The scheme addressed a relatively narrow spectral region (< 200 cm^{-1}), and was able to measure the Raman free induction decay. Later, detection covering broad-range of Raman bands was achieved using the SC from fibers [58]. Moreover, temporal shape of the probe pulse can be optimized using the femtosecond adaptive spectroscopic technique (FAST) [40] or dedicated spectral filter [59] to achieve optimal signal-to-background ratio.

An equivalent scheme is to use Fourier transform to retrieve the CARS signal [60]. Here a single broadband femtosecond pulse is used for intrapulse excitation of multiple Raman bands. By passing the pulse through a Michelson interferometer, it is split into two replica, serving as the pump and probe, respectively. By monitoring the variation of the generated anti-Stokes signal as the pulse delay changes, a fringe pattern can be recorded, which, after Fourier transform, can

be used to extract the CARS spectrum. Improvement using heterodyne detection has also been demonstrated, in which an additional reference beam is introduced as the local oscillator (LO) [61]. However, such delay scanning is typically slow, and limits the possible frame rate in imaging. More recently, fast scanning methods has been proposed which can run up to 20000 spectra per second [62] and scanning a wide field-of-view [63], showing potential for high-speed microscopic applications in the future.

1.3 Section overview

The rest of the dissertation is organized as follows. In Chapter 2, we introduce the single-beam CARS scheme in more details, and demonstrate our setup of pulse shaping without spatial light modulator. Moreover, we compare the collection of back-scattered CARS signal using our setup with that used in previous work, and show an enhanced epi-detection efficiency. Also, we demonstrate our capability in low-wavenumber Raman band detection, which is enabled by the spatial filtering through our pulse shaper. This can serve as an inexpensive alternative to the commonly used interference filters.

In Chapter 3, we further simplify our single-beam setup, and incorporate the FAST CARS technique to achieve a versatile single-beam FAST CARS system, which is easy to work with and allows various beam geometries for excitation and collection. Furthermore, by exploiting the phase relation between the CARS signal and the FWM background, heterodyne detection can be achieved through fast modulation of the probe delay, allowing an increased signal acquisition speed in our pulse shaper. We also demonstrate the incorporation of spectral detection into the pulse shaper, providing a compact module for beam modulation and CARS signal acquisition.

Chapter 4 is devoted to SC generation in large-mode area (LMA) PCF, and we apply this SC source in our CARS microspectroscopy setup. Effects of different fiber parameters on the SC generation are analyzed, and we show that a broadband SC pulse extending beyond 1600 nm, corresponding to an effective Raman detection range over 3000 cm^{-1}, can be achieved. We demonstrate its applicability in multiplex CARS scheme, and show the capability of the CARS microscope based on this novel source.

We further explore another CARS imaging scheme, known as the wide-field CARS, in Chapter 5, in order to enhance the acquisition speed of CARS microscopy. Here CARS imaging is achieved in a similar fashion as that in the bright-field microscopy— by directly illuminating and imaging a wide area on the sample. Selective imaging with regard to different Raman band is achieved by applying different filters in the signal beam path. We demonstrate a multiplex wide-field CARS setup using the high-energy SC source from LMA PCF, and show chemical selectivity in imaging polymer bead samples. Video-rate imaging is also demonstrated, followed by discussions on its limitations and possible advancement.

2. LOW WAVENUMBER EFFICIENT SINGLE-BEAM COHERENT ANTI-STOKES RAMAN SPECTROSCOPY *

This chapter focuses on the single-beam CARS spectroscopy scheme. First, 4f pulse shaping technique is introduced, which forms the foundation of most single-beam CARS setups. Next, the development of different single-beam CARS schemes is reviewed, with an emphasis placed upon those implementing spectral holes to achieve CARS detection. Following this track, we demonstrate our single-beam CARS setup using a spectral hole. Its capabilities in both forward and backward detection in the low-wavenumber regime are examined, and we show an improved efficiency in the back-scattered signal collection as compared to earlier works. Finally we discuss possible improvements such as further extending the detection limit into the low wavenumber region.

2.1 Single-beam coherent anti-Stokes Raman scattering spectroscopy

2.1.1 4f pulse shaping

This technique is generally referred to as Fourier transform pulse-shaping [64], where the laser light is spatially dispersed into different frequency components on the so-called 'Fourier plane', and each component is modulated separately to produce the desired pulse shape. Such a shaping mechanism can be described in the frequency domain as a transformation of the laser field:

$$E_{\text{out}}(\omega) = E_{\text{in}}(\omega)H(\omega), \tag{2.1}$$

where $E_{\text{out}}(\omega)$, $E_{\text{in}}(\omega)$, and $H(\omega)$ are the output electric field, input electric field, and the transformation function, respectively. Note that $H(\omega)$ is the Fourier transform of the better-known response function $h(t)$ of the system. A simple example is that when there is no modulation, we have $h(t) = \delta(t)$ and therefore $H(\omega) = 1$, so that no change is imposed on the input pulse.

*Reprinted with permission from "Low wavenumber efficient single-beam coherent anti-Stokes Raman scattering using a spectral hole" by Y. Shen, D. V. Voronine, A. V. Sokolov, and M. O. Scully, 2015. *Optics Letters*, 40, 1223-1226, Copyright [2015] by Optical Society of America.

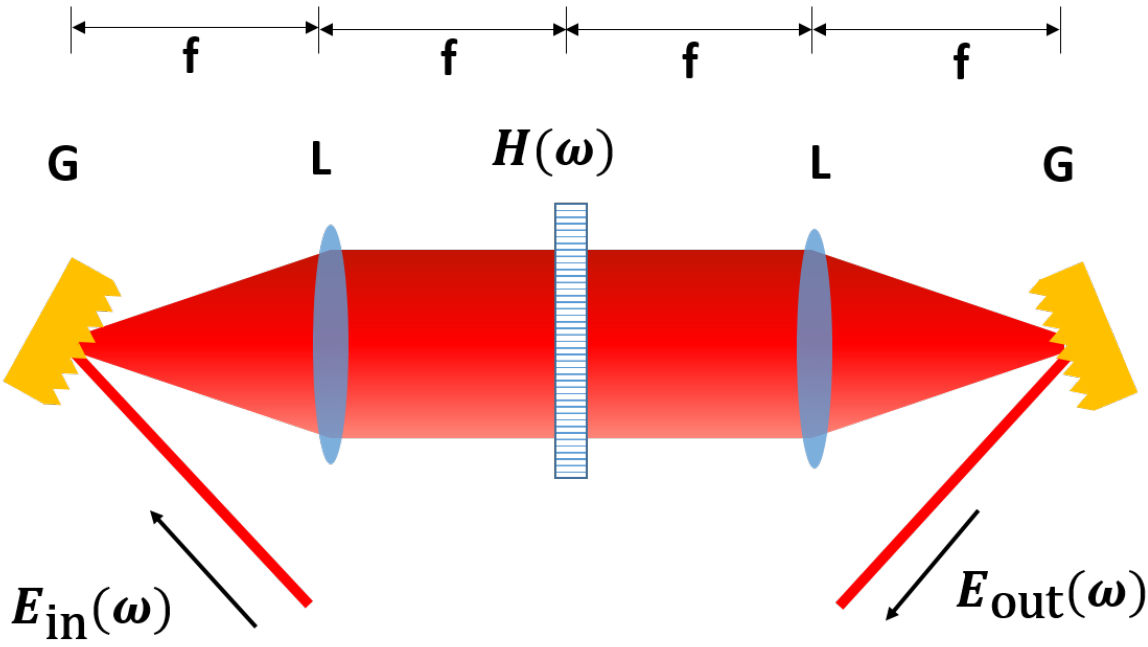

Figure 2.1: A typical layout of the 4f pulse shaping system. G: grating; L: lens, with focal length denoted as f; H(ω): the phase function implemented by the modulator.

A general layout of the 4f pulse shaper is shown in Fig. 2.1. The input pulse is separated into different frequency components by a dispersion element— which is given as a grating in Fig. 2.1, but it can also be replaced with a prism for broadband application [65], or a virtually imaged phased-array for comb-resolved fine shaping [66]. The angularly dispersed frequency components are then focused to diffraction-limited spots at the back focal plane of the first focal element— which is performed by a lens in Fig. 2.1. This plane is referred to as the Fourier plane, because the dispersion and focusing element (grating) effectively performs a Fourier transform on the input pulse that converts the angular dispersion to a spatial separation of different frequency components. Pulse shaping is then achieved by applying spatially patterned mask or programmable spatial light modulator (SLM) to change the amplitude and phase of each frequency components. The light then passes through the second focusing element (lens) to combine different frequency components on the second dispersion element (grating), providing a collimated output pulse with desired pulse shape. Because all major elements are separated by one focal length of the focusing element, making the total length of the setup four times the focal length as shown in Fig. 2.1, thus the name

4f pulse shaper. The key idea here is that waveform synthesis is achieved by parallel modulation of all frequency components in the Fourier plane, therefore femtosecond-time-scale control on the ultrashort pulse can be achieved without the need of ultrafast modulators [64].

Commonly used SLM include liquid crystal modulator (LCM), acousto-optic modulator (AOM), and deformable mirror (DM). Liquid crystal consists of long, thin, rod-like molecules, which will rotate under the application of external electric field. This, in turn, will change its refractive index for light with certain polarization. LCM is made under such principle— by constructing arrays of small liquid crystal element with electrodes, precise rotation of the molecule can be achieved through voltage control on the electrode. This is then translated into a phase change on the light propagating through it. Modern LCM typically contains thousands of pixels, with modulation rate up to the kHz range.

On the other hand, AOM uses standing acoustic wave in a transparent crystal, typically TeO_2, driven at radio-frequency (RF) by piezoelectric transducer. Different patterns are produced by changing the RF drive waveform. Unlike the LCM which suffers from pixellation effect, the modulation in the Fourier plane in AOM is continuous, with possible refreshing rate up to MHz. But this also limits the application of AOM to oscillators with high pulse repetition rate. Also, AOM is intrinsically less efficient due to crystal nonlinearities.

Lastly, deformable mirror modulates the light through the deformation of a reflecting thin membrane or a semipassive bimorph structure. Deformation is achieved by the piezoelectric actuators beneath the membrane. Such mirrors have been widely used for wavefront corrections [67]. As compared to the other two SLMs, DM has less effective element for pulse shaping, but enjoys a high efficiency and wider applicable wavelength range into the IR [68]. More detailed discussions on the principles and comparison between different types of modulators can be found in earlier reviews [69, 70].

2.1.2 Single-beam coherent anti-Stokes Raman spectroscopy scheme

As we have seen in the previous chapter, the strength of the Raman signal can be increased by generating vibrational coherence using pump and Stokes laser fields [31, 33, 36, 44], and the non-

resonant background can be eliminated through a variety of modifications [57, 40, 37]. However, these schemes typically require recombining of multiple beams, which involve alignment of ultrashort pulses to overlap both temporally and spatially. A simplified version of CARS that uses only a single laser beam has also been demonstrated [50]. The scheme was based on coherent modulation of the input femtosecond pulse— by applying periodic phase pattern in the 4f pulse shaper, the original transform-limited input pulse will be broken into a train of pulses, with temporal separation directly related to the modulation period in the frequency domain [50]. In a time-domain picture, when this separation matches the period of a vibrational mode, this vibration is in resonance, creating strong anti-Stokes signal. Then by recording the signals at different modulation frequencies using the SLM, a CARS spectrum can be retrieved by performing Fourier transformation on the temporal signal. This method can suppress the nonresonant background, and has been extended to other schemes using heterodyne [71], time-resolved [72], or Fourier transform interferometric measurement [73].

Given that it is relatively time-consuming to scan over different modulation period, another type of single-beam CARS scheme has been devised, in which a narrowband probe is created through the pulse shaper— typically by applying a π phase shift over a narrowband region on the SLM. Therefore, the broadband portion that is not modified serves to create strong impulsive excitation on various vibrational modes, and the narrowband probe produces corresponding features on the anti-Stokes signal [39]. In this way, CARS spectra are detected directly by multichannel detectors. This was followed by several variations [74, 75], and has been applied to stand-off detection [76, 77]. It is worth noting that most of the single-beam methods utilize spatial-light modulators such as AOM or LCM for pulse shaping.

Recently, Silberberg and coworkers have demonstrated the technique of single-beam CARS with a spectral notch/hole. Similar to the single-beam scheme mentioned above, a broadband femtosecond pulse was used to provide the pump and Stokes field, but the probe was generated by blocking a narrowband region in the frequency domain, as shown in Fig. 2.2. This was achieved using either a 4f pulse shaper or a resonant photonic crystal slab [78, 79, 80]. From Eq. 1.16, the

following expressions can be used to give the single-beam CARS signal using a spectral hole [39]:

$$P_{\mathrm{r}}^{(3)}(\omega) = C_{\mathrm{r}} \int d\Omega \frac{E(\omega-\Omega)}{\Omega-\Omega_{\mathrm{R}}+i\gamma_{\mathrm{R}}} A(\Omega), \tag{2.2}$$

$$P_{\mathrm{nr}}^{(3)}(\omega) = C_{\mathrm{nr}} \int d\Omega E(\omega-\Omega) A(\Omega). \tag{2.3}$$

Here $E(\omega)$ is the electric field of the input pulse. $P_{\mathrm{r}}^{(3)}(\omega)$ and $P_{\mathrm{nr}}^{(3)}(\omega)$ are the resonant and non-resonant contributions to the third-order polarization, corresponding to χ_{R} and χ_{NR}, respectively. And C_{r} and C_{nr} are their amplitude coefficients. Also we have $A(\Omega) = \int d\omega E^*(\omega-\Omega)E(\omega)$, and Ω_{R} and γ_{R} are the characteristic Raman shift and decay rate, respectively. The polarizations are linked to the CARS signal in Eq. 1.16 via $I_{\mathrm{CARS}} \propto |P^{(3)}|^2 = |P_{\mathrm{r}}^{(3)} + P_{\mathrm{nr}}^{(3)}|^2$. In the single-beam CARS scheme, the spectral hole corresponds to a narrowband portion in $E(\omega)$, and therefore has a minor effect on $P_{\mathrm{nr}}^{(3)}$. On the other hand, due to the denominator in Eq. 2.2, sharp features in $E(\omega)$ originating from the spectral hole are manifested in $P_{\mathrm{r}}^{(3)}$ but shifted by Ω_{R}. This is shown in Fig. 2.2a in the frequency domain as a blue-shifted non-linear signal 'dip', with a frequency difference of Ω_{R} from the probing spectral hole [79]. In the time domain picture shown in Fig. 2.2b, the modulated pulse can be seen as a sum of the ultrafast pump/Stokes pulse and a long-duration probe with an opposite phase.

In the following, we demonstrate an approach to detect low wavenumber vibrational signals using the single-beam CARS with a spectral hole created within a 4f laser pulse shaper [81]. The setup can be used for both forward- and back-scattered CARS signal detection, and the back-scattered signal collection yields a higher efficiency as compared to previous single-beam CARS schemes using beam-splitter [82, 83]. We also show its capability in low wavenumber CARS spectra detection without using an interference filter. This setup is suitable for characterizing low wavenumber vibrations such as important conformational modes of complex biomolecules.

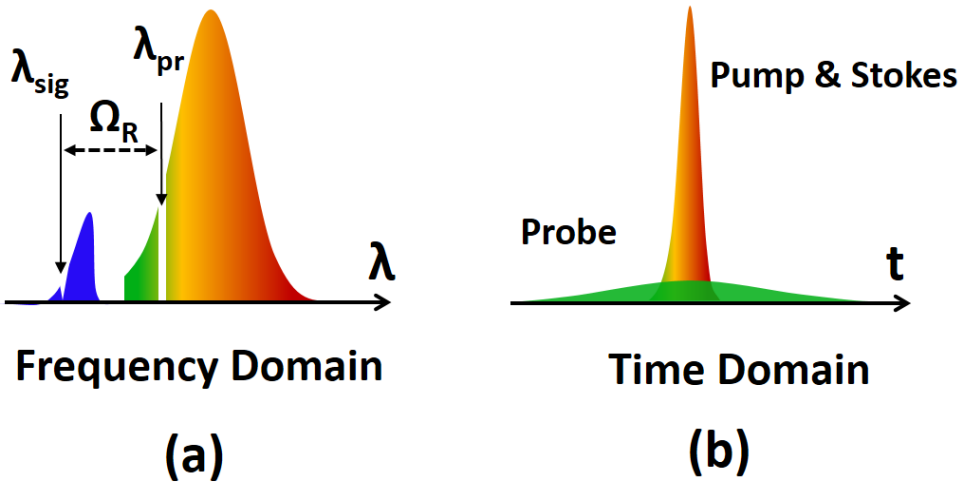

Figure 2.2: Principle of single-beam CARS with a spectral hole. (a) Frequency domain picture, with narrowband probe wavelength λ_{pr}, and signal wavelength λ_{sig} that is shifted by the characteristic vibrational frequency Ω_R. (b) The time domain picture of the pump/Stokes and probe pulse.

2.2 Low-wavenumber efficient setup using spectral hole

2.2.1 Experimental setup description

The setup is shown in Fig. 2.3. Femtosecond laser pulses with 785 nm center wavelength, $\sim$ 20 fs duration and 80 MHz repetition rate (Micra, Coherent) were shaped by a home built 4f pulse shaper after dispersion compensation using two prisms [84], and then were focused onto the sample. At the Fourier plane of the pulse shaper, a needle mounted on translation stages was used to block a part of the pulse, generating a spectral hole. A knife edge right-angle prism mirror (MRAK25-P01, Thorlabs) was placed at the high-frequency portion of the pulse, with the side facing the input light covered with black paper so as to block the frequency components that coincides with the CARS signal, while the other side was used to guide the reflected signal out for detection. The inset in Fig. 2.3 shows a typical spectrum of the excitation pulse with a spectral hole at 781.5 nm. The cut-off wavelength was fixed at 767.4 nm, and the spectral hole width was 0.9 nm at full-width-half-maximum (FWHM). The input beam size was $\sim$ 1 cm in diameter, with a power of 70 mW before focusing onto the sample. All liquid samples were kept in quartz cells

(1-G-1, Starna).

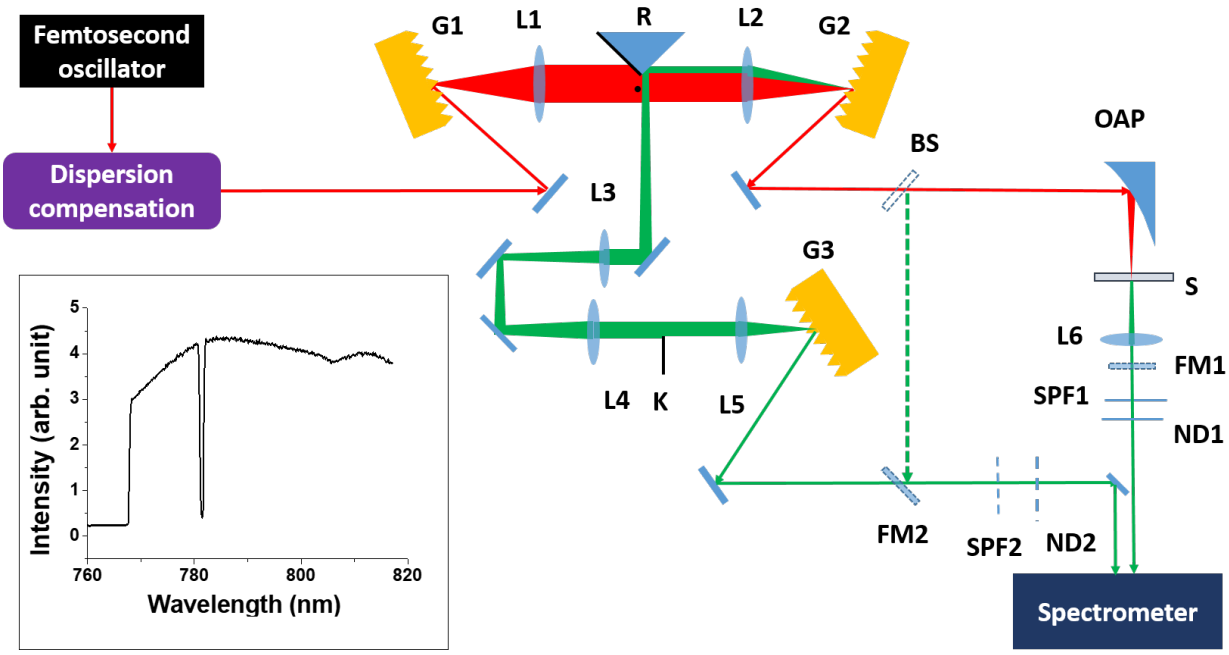

Figure 2.3: Experimental setup for single-beam CARS with a spectral hole. L1 to L5: achromatic lenses with f=100 mm; L6: achromatic lens with f=30 mm; G1 to G3: 830 grooves/mm gold-coated gratings blazed at 800 nm; R: right-angle prism mirror; K: knife edge; OAP: off-axis parabolic mirror with f=20 mm; S: sample; SPF1 and SPF2: short-pass filters; ND1 and ND2: neutral density filters; FM1 and FM2: flip mirrors; BS: 70/30 beamsplitter. Dashed line represents the signal path in the back-scattered detection using the beam-splitter scheme. Inset shows the excitation pulse spectrum with a spectral hole at 781.5 nm.

In the forward detection scheme, light transmitted through the sample was collected by an achromatic lens and passed through two filters — a 760 nm short-pass filter (FF01-775/SP-25, Semrock) to suppress the residual excitation pulse, and a neutral-density (ND) filter to prevent signal saturation. The transmitted signal was then measured with a spectrometer (Surespectrum, Bruker Optics) and a CCD detector (iDus420, Andor), placed $\sim$ 5m away from the setup to avoid stray light. For demonstration of back-scattering detection, we used a mirror to retro-reflect the forward signal generated in the liquid sample [82]. This reflected signal was sent back to the pulse shaper, and only the blue-shifted CARS signal was picked up by the prism mirror. The reflection

path including gratings G2, G3 and lenses L2 to L5 effectively forms an 8f pulse shaper [85], which guarantees a second Fourier plane of the anti-Stokes signal formed between L4 and L5. A second knife edge was used here to block the residue of the original pulse with frequency close to the cutoff edge that was partially transmitted/scattered at the knife edge mirror. This transmitted light was then collimated by the grating and sent to the spectrometer. We have also tested the scheme in which a beam-splitter was used to guide the back-reflected signal, in order to compare the detection efficiency— this is depicted by dashed lines in Fig. 2.3.

2.2.2 Result analysis

Simulation and experimental test using carbon tetrachloride

First we present polarization field simulation using Eqs. (2.2) and (2.3). We assumed a Gaussian input pulse with a bandwidth of 50 nm centered at 800 nm. The short-wave cut-off was at 765 nm, and there was a rectangular spectral hole around 775 nm with a width of 1 nm. Other parameters were set as follows: $\Omega_{\mathrm{R}} = 400$ cm^{-1}, $\gamma_{\mathrm{R}} = 10$ cm^{-1}, C_{r} and C_{nr} were chosen such that the effect of the resonant signal is visible in the total polarization. Calculated $|P^{(3)}|$, $|P^{(3)}_{\mathrm{nr}}|$ and the rescaled $|P^{(3)}_{\mathrm{r}}|$ are shown in Fig. 2.4a. The cut-off edge at 760nm was a simulation of the short-pass filter used to eliminate the excitation pulse. Unlike the smooth nonresonant signal, $|P^{(3)}_{\mathrm{r}}|$ showed a characteristic dip around 752 nm, shifted from the spectral hole by the Raman frequency Ω_{R}. The dip appeared as a 'shoulder' in the total polarization signal $|P^{(3)}|$. In order to obtain a peak-like spectrum, we simulated two signals with slightly shifted hole positions at 774.05 nm and 775.95 nm, and showed their difference in Fig. 2.4b, in which a peak corresponding to the desired Raman shift at ~ 400 cm^{-1} appeared [79].

Experimental signals with a spectral hole shift of 0.9 nm obtained from carbon tetrachloride (CCl_4) in the forward detection are shown in Figs. 2.4c and 2.4d. The CCD exposure time was set at 20 ms, which was limited by the hardware. The CARS signals were averaged over 100 spectra. The difference signal in Fig. 2.4d represents our target CARS spectrum, and shows separated peak structures corresponding to the CCl_4 Raman bands, as expected from earlier simulations. The

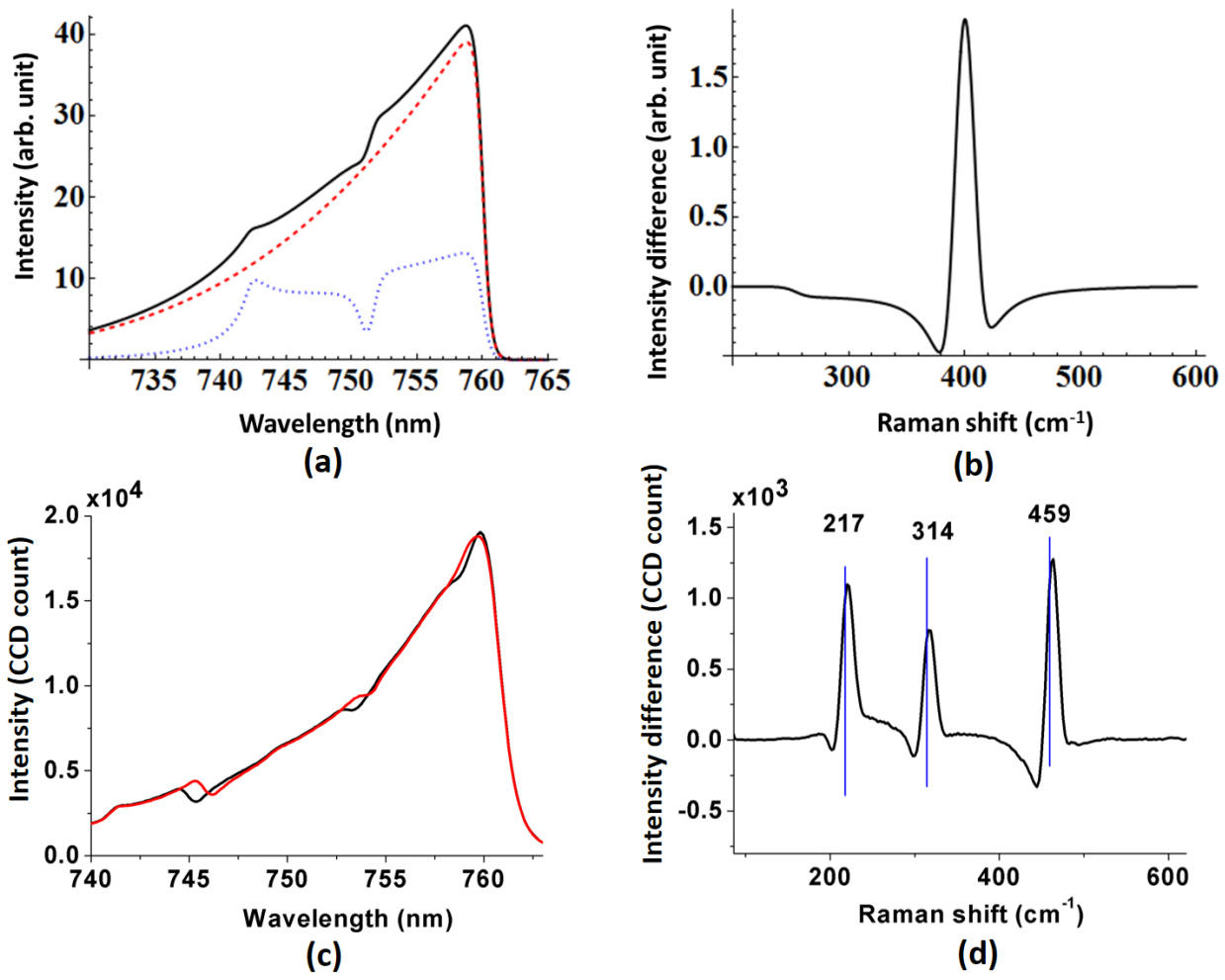

Figure 2.4: Simulated and experimental single-beam CARS results with a spectral hole. (a) Simulated polarization fields: $P^{(3)}$ (solid black), nonresonant $P_{\mathrm{nr}}^{(3)}$ (dashed red), and resonant $P_{\mathrm{r}}^{(3)}$ (dotted blue) rescaled by a factor of 40. (b) Intensity difference of two $P^{(3)}$ signals with different spectral hole positions. (c) CARS spectra of carbon tetrachloride (CCl_4) detected with shifted spectral hole positions. (d) Single-beam CARS signal from CCl_4 obtained as the difference between the two spectra in (c). The Raman shift is calculated from the center of the two holes. Blue vertical lines represent the spontaneous Raman signals.

deviations of the CARS peak values from the spontaneous Raman data [86] were approximately 3 cm^{-1}, which could be due to the reading error of the center positions of the two holes, or due to the lineshape distortion when taking difference spectra. Note that an additional ND filter with 0.7% transmissivity was placed at the entrance of the spectrometer to prevent CCD saturation. This high signal intensity results from the strong intrapulse excitation [45], and is beneficial for microscopic applications as it allows for higher signal detection speed.

Enhanced backward detection efficiency

Early schemes have used beam-splitter to collect back-scattered signals in stand-off single-beam CARS schemes [82, 83]. As a simple analysis of the efficiency of such schemes, we assign the four-wave mixing signal obtained without any loss as unity. Then by adding a beam-splitter in the path, the collected back-reflected signal intensity will be $I \propto T^3(1-T)$, where T is the transmissivity of the beam-splitter. Here the T^3 factor represents a decrease in the four-wave mixing signal due to the input pulse attenuation, and $1-T$ is the loss of the back-scattered signal reflected from the beam-splitter. The maximum detected signal occurs when T is $\sim 75\%$, and in this case I is $\sim 10\%$ of the original signal. For pulses with sufficient energy as in the previous works, this did not present as a problem. However, for systems in power-starving situations, the loss due to the beam-splitter is critical, such as in microscopic applications where throughput will be further attenuated due to other optical losses.

Here we show that by using the pulse shaper for epi-CARS signal collection, detection efficiency can be improved. For comparison, we also implemented the beam-splitter-based setup with a 70/30 beamsplitter placed before the sample. Extra dispersion introduced by the beam-splitter was compensated using the prism pair. Figure 2.5 shows the resulting total nonlinear and CARS signal obtained from CCl_4. Our pulse-shaper-based setup gave a $\sim$ three-fold enhancement compared to the beam-splitter-based scheme. Since the same ND filter and exposure time were used in the earlier-shown transmission detection of CCl_4, we can also compare this with the forward detection result in Fig. 2.4 and find that the beam-splitter scheme intensity is about 7% of that detected in the forward scheme. This is reasonable if we take into account the loss from the quartz

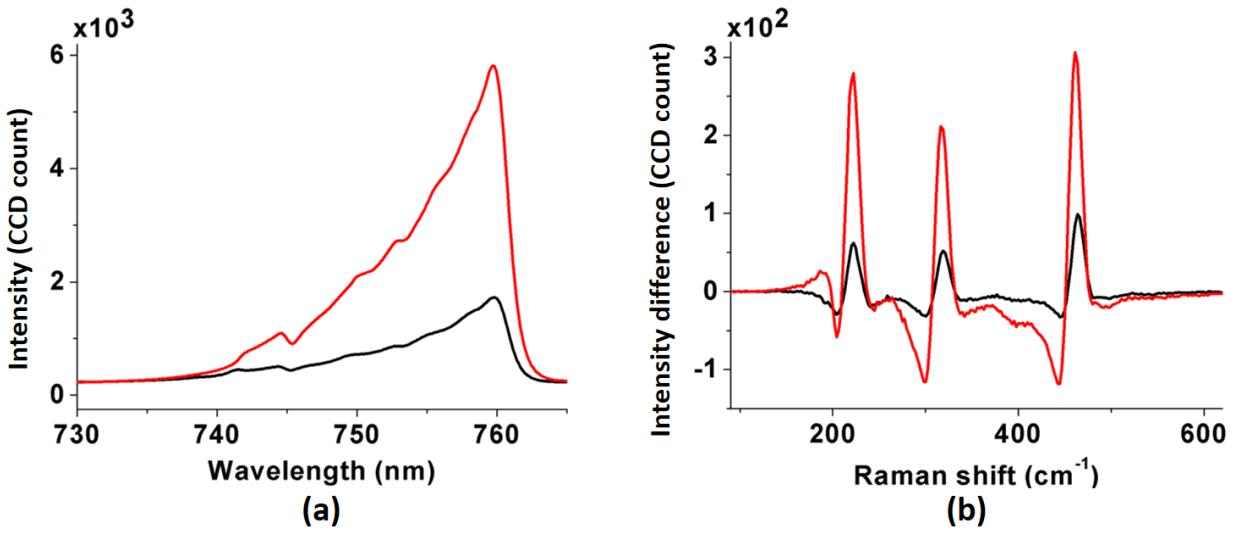

Figure 2.5: Comparison of two back-reflected detection schemes: pulse-shaper-based (red) and beamsplitter-based (black) CARS with a spectral hole. (a) Total nonlinear signals, and (b) difference CARS signal.

cell ($\sim 15\%$) and the internal loss from the beam-splitter ($\sim 17\%$). The efficiency can be further improved by increasing the diffraction efficiency of gratings in the pulse shaper, or by implementing more sensitive detectors such as PMT assisted by lock-in amplifier [71]. Other schemes with high collection efficiency using dichroic mirrors or interference filters can also be used [33, 44, 71], but suffer from the intrinsic filter-edge limit and pulse distortion in the low-wavenumber region, which will be shown in the next section. One thing to note is that even though we only compared the back-reflection of forward CARS signals from liquid, our scheme can also be used in epi-detection of solids or turbid samples in microscopy as well.

Filterless low-wavenumber CARS detection

We also demonstrate single-beam CARS without the use of an interference short-pass filter, which can be a limiting factor in the low-wavenumber region detection [87]. This is possible because the pulse shaper itself acts as a short-pass filter for backward-propagating CARS signals. This is similar to the idea used in multi-stage monochromators, where high resolution and low frequency detection are achieved through spatial filtering. A comparison of the 1,1,2,2-

tetrachloroethane (TeCA) spectra obtained in the forward detection scheme using the 760 nm short-pass filter, and that in the backward detection using our pulse shaper are shown in Fig. 2.6, with the same exposure time, signal attenuation, and averaging as in the previous data. Figure 2.6a shows that the spectral edge using our pulse shaper exceeded that using the interference filter. This enables our setup to measure lower wavenumber Raman shifts. As a result, the 173 cm^{-1} and 89 cm^{-1} Raman peaks [86] blocked by the interference filter are visible in our backward detection setup, as shown in Fig. 2.6b. The lowest wavenumber resolvable Raman shift depends on the cut-off edge of the non-linear signal, and in the present setup this is limited to ~ 80 cm^{-1}.

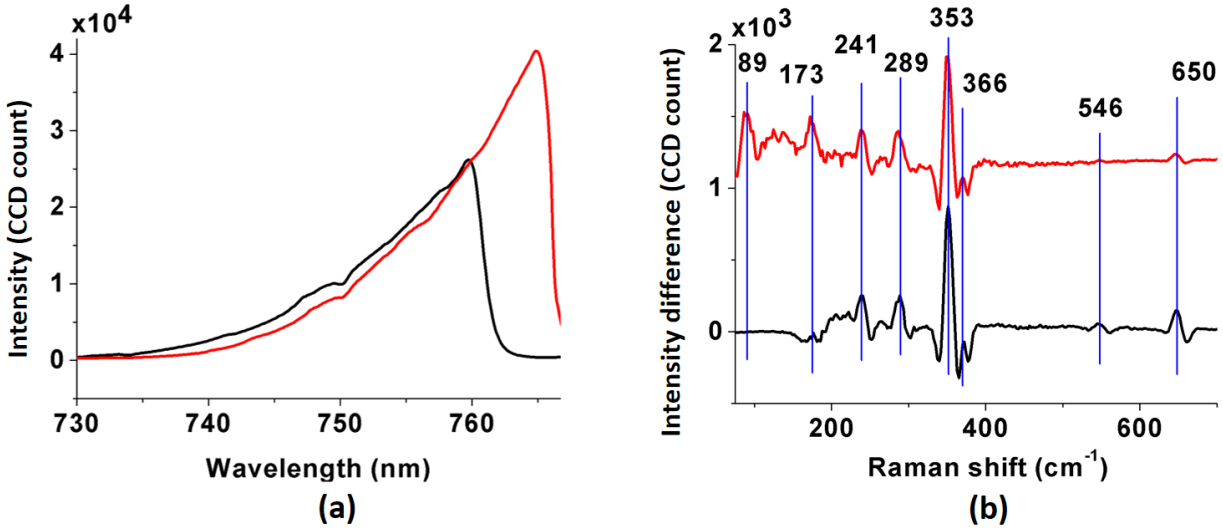

Figure 2.6: Comparison between forward (black) and back-scattered (red) signal of 1,1,2,2-tetrachloroethane (TeCA): (a) total nonlinear and (b) CARS signals. The back-scattered signal is rescaled by a factor of 3.3.

2.2.3 Discussions

The needle tip in our pulse shaper serves two functions: the main function is to block the input light and form the spectral hole; in the meantime, it also blocks the residual excitation light that scatters from the knife edge mirror— because spectral components are focused to a finite size in the Fourier plane, there is a portion close to the edge that will inevitably pass through and being

reflected back due to Rayleigh scattering. This shows up as a very strong and sharp peak in the signal spectrum, and will saturate the CCD if the needle tip is absent. Better design of the pulse shaper should enable an improved shielding from such unwanted light in the epi-detection scheme.

The spatial filtering capability of the pulse shaper mainly relies on how well we can resolve different spectral components in the Fourier plane. It is roughly proportional to the groove number density of the grating, and inversely proportional to the input beam size. Hence if replaced with a 2400 grooves/mm grating and with the beam size increased by 1.5 times, the lowest detectable Raman shift can be decreased to ~ 20 cm^{-1} theoretically. Other factors such as the angle of incidence onto the grating and the input pulse energy also affect the lowest detection limit. Another merit of using such spatial filtering is that the cut-off edge is easily tunable with no broadening or distortion to the femtosecond pulse. This setup can also be applied to low-wavenumber spontaneous Raman spectroscopy by moving the prism mirror to the long wavelength side to perform spectral filtering on the input laser and the signal. This would be a less expensive solution compared to commercial low-wavenumber Raman filters, but comes with the price of a decreased efficiency and bulky setup.

Another thing worth noting is that the difference measurement implemented here resembles that used in shifted excitation Raman difference spectroscopy [88], and the detection is intrinsically heterodyne— the nonresonant portion P_{nr} is used as the local oscillator to enhance the Raman signal. This is beneficial for recognizing weak vibrational modes, but the fluctuation in the background will also deteriorate the signal curve. Last but not least, the limitation on the detection bandwidth can be resolved by adopting oscillators with broader bandwidth to include modes up to 2000 cm^{-1} [89].

In summary, we have demonstrated an approach to detect low-wavenumber vibrational signals based on single-beam CARS with a spectral hole, using 4f pulse shaper and only basic optical components. We examined its capability in both forward and backward detection schemes in the low-wavenumber region. We also showed an improved efficiency in collecting backward propagating signal, and discussed possible solutions for extending the detection region into even lower wavenumber region.

3. SINGLE-BEAM COHERENT ANTI-STOKES RAMAN SPECTROSCOPY USING FEMTOSECOND ADAPTIVE SPECTROSCOPIC TECHNIQUE*

In this chapter, we further improve our single-beam CARS setup by simplifying the pulse shaper design, and incorporating the FAST technique [40] on the excitation pulse. In this chapter, a brief review is first given on the FAST CARS spectroscopy. Then we outline the design of a versatile single-beam FAST CARS setup that allows easy alignment and switching between different excitation and detection layouts. To increase the detection speed, we also implement piezo modulation on the probe delay so as to allow fast CARS signal retrieval through heterodyne. In addition, spectral detection of the back-scattered signal is incorporated into the pulse shaper, allowing compact and efficient system design. We demonstrate the capabilities of CARS microspectroscopy by imaging silicon and molybdenum disulfide (MoS_2) microstructure.

3.1 Introduction to femtosecond adaptive spectroscopic technique

As mentioned in the previous chapters, the nonresonant background has often prohibited the faithful retrieval of CARS spectrum, and various techniques have been devised to overcome this problem, such as epi-detection [90], polarization CARS [38] or frequency modulation [91] scheme. FAST CARS was proposed in the early years of CARS microscopy, also aiming at effective suppression of the nonresonant background [92]. In the conventional CARS scheme, the nonresonant background is strong due to the temporal overlap between the probe and pump/Stokes fields, as shown in Fig. 3.1c. In the FAST CARS scheme, one takes advantage of the difference between the long-lived vibrational coherence and the instantaneous nonresonant background, and applies a delay on the probe relative to the pump/Stokes pulse to significantly suppress the nonresonant background, while maintaining an appreciable portion of the CARS signal. Notice that unlike the

*Reprinted with permission from "A versatile setup using femtosecond adaptive spectroscopic technique for coherent anti-Stokes Raman scattering" by Y. Shen, D. V. Voronine, A. V. Sokolov, and M. O. Scully, 2015. *Review of Scientific Instruments*, 86, 083107, Copyright [2015] by AIP Publishing, and with permission from "Single-beam heterodyne FAST CARS" by Y. Shen, D. V. Voronine, A. V. Sokolov, and M. O. Scully, 2016. *Optics Express*, 24, 21652-21662, Copyright[2016] by Optical Society of America.

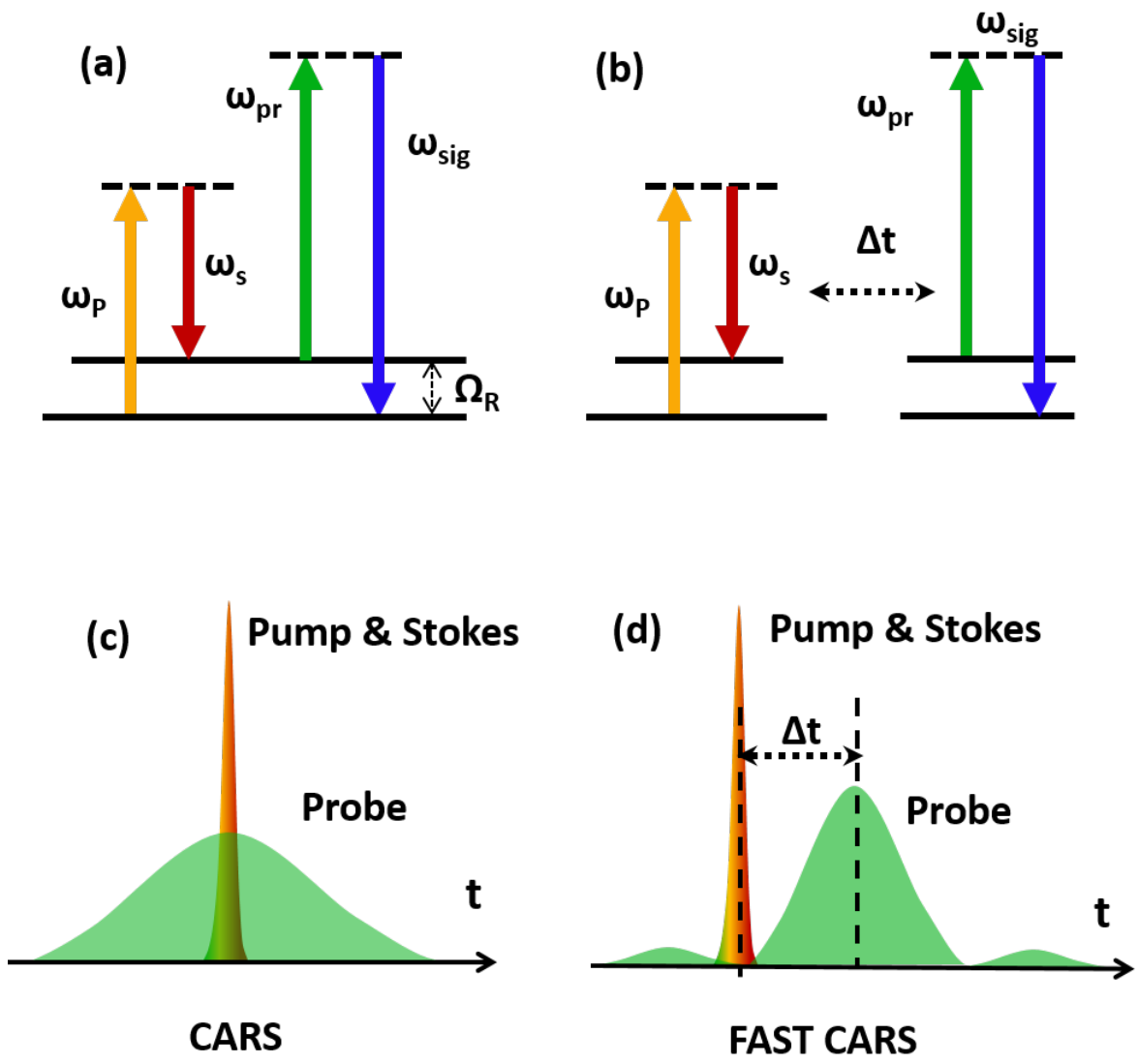

Figure 3.1: Energy diagrams of the (a) CARS and (b) femtosecond adaptive spectroscopic technique (FAST) CARS processes, and temporal pictures of the (c) CARS and (d) FAST CARS processes. ω_p: pump; ω_s: Stokes; ω_{Pr}: signal; ω_{sig}: signal; Ω_R: characteristic Raman shift.

case in time-resolved CARS measurement [58] in which only a delay between pulses is applied, in FAST CARS the probe laser pulse is also shaped to improve the signal-to-background ratio [40]. Figures 3.1b and 3.1d illustrate the FAST CARS scheme, in which the probe pulse with a sinc temporal shape has its node overlapped with the pump/Stokes pulse, so as to minimize their temporal overlap and suppress the nonresonant background; while the main portion of the probe pulse still interacts with the vibrational coherence and produces CARS signals [40].

Still, the original implementation of the FAST CARS scheme requires up to three separate beams from the amplified laser system, and beam geometry has to be carefully adjusted so as to meet the phase-matching condition due to the loose focusing element [40]. Benefiting from the tight-focusing in a microscopic setup [31], here we demonstrate FAST CARS microspectroscopy using the single-beam setup [93]. The setup uses a femtosecond Ti: Sapphire laser oscillator and a 4f pulse shaper with folded geometry, and the pulse shaping is carried out through common optical elements so no complicated SLM equipment is needed. Our setup is simple in alignment, and can be easily switched between the collinear single-beam geometry and the noncollinear two-beam geometry. We also demonstrate the capability of detecting both the transmitted and back-scattered signals. Moreover, we further update the system to implement single-beam heterodyne FAST CARS microscopy by exploiting the phase relation between the CARS and the LO signal generated inside the sample [94]. An improved epi-detection efficiency is obtained by combining the spectral detection and the pulse shaping unit, which reduces redundant optical components as compared to our earlier setups [81, 93] and eliminate the requirement of an external spectrometer.

3.2 Versatile single-beam coherent anti-Stokes Raman spectroscopy using femtosecond adaptive spectroscopic technique

3.2.1 Setup description

The pulse shaper in our current setup uses a folded geometry [69] as opposed to the transmission geometry previously adapted [81]. Such a design facilitates the alignment procedure and provides an easy configuration to employ a probe delay in the pulse shaper. The block diagrams

of the experimental setup using different beam and detection configurations are shown in Fig. 3.2 [93]. The laser source included a broadband oscillator (TS laser kit, KMLabs), a double-prism compressor, a telescope, and a long-pass filter. The output pulse from the oscillator was centered at 800 nm, with a spectral FWHM of 45 nm. The separation between the prisms in the compressor was $\sim$1 m, optimized by monitoring the autocorrelation trace of the output pulse. The telescope was consisted of two convex lenses with focal lengths of 700 mm and 300 mm, respectively, to shrink the beam size to $\sim$2 mm at the pulse shaper input. A long-pass filter (FF01-776/LP-25, Semrock) was used after the telescope to block the high-frequency component of the pulse that coincided with the CARS signal. We denote this beam from the laser source as the primary beam. It was then guided into the pulse shaper to generate the desired pump/Stokes and probe beam. Our versatile setup allows the probe beam and the pump/Stokes beam to be set up in either collinear or noncollinear configuration. In the collinear configuration, the two beams propagate collinearly; whereas in the noncollinear configuration, they are parallel to each other but exhibit a tunable spatial offset (set to $\sim$7 mm in later experiments), allowing spatial separation of the two beams.

After the pulse shaper, the two beams were focused onto the sample by an off-axis parabolic mirror (50328AU, Newport), with an effective focal length close to 20 mm. Figures 3.2e and 3.2f show different detection methods and beam geometries at the sample for the collinear and the noncollinear configuration, respectively. In the former case, the two beams were spatially overlapped before focusing onto the sample. After that, beams were collimated by an achromatic lens with a focal length of 30 mm. Again for transparent sample, we used a flip mirror placed behind the collimation lens to retro-reflect the forward signal, so as to simulate backward detection [81], as shown in Fig. 3.2e. In the noncollinear configuration, the two beams were spatially separated before focusing onto the sample. After the collimation lens, the two beams propagated in parallel again. Then the pump/Stokes beam, together with the FWM signal it generated, were terminated by a beam block, leaving only the probe and CARS signal beam propagating forward or being reflected by the flip mirror, as shown in Fig. 3.2f. After the sample, the forward-propagating signal passed a short-pass filter (SP01-785RU-25, Semrock), and was then sent to the spectrometer

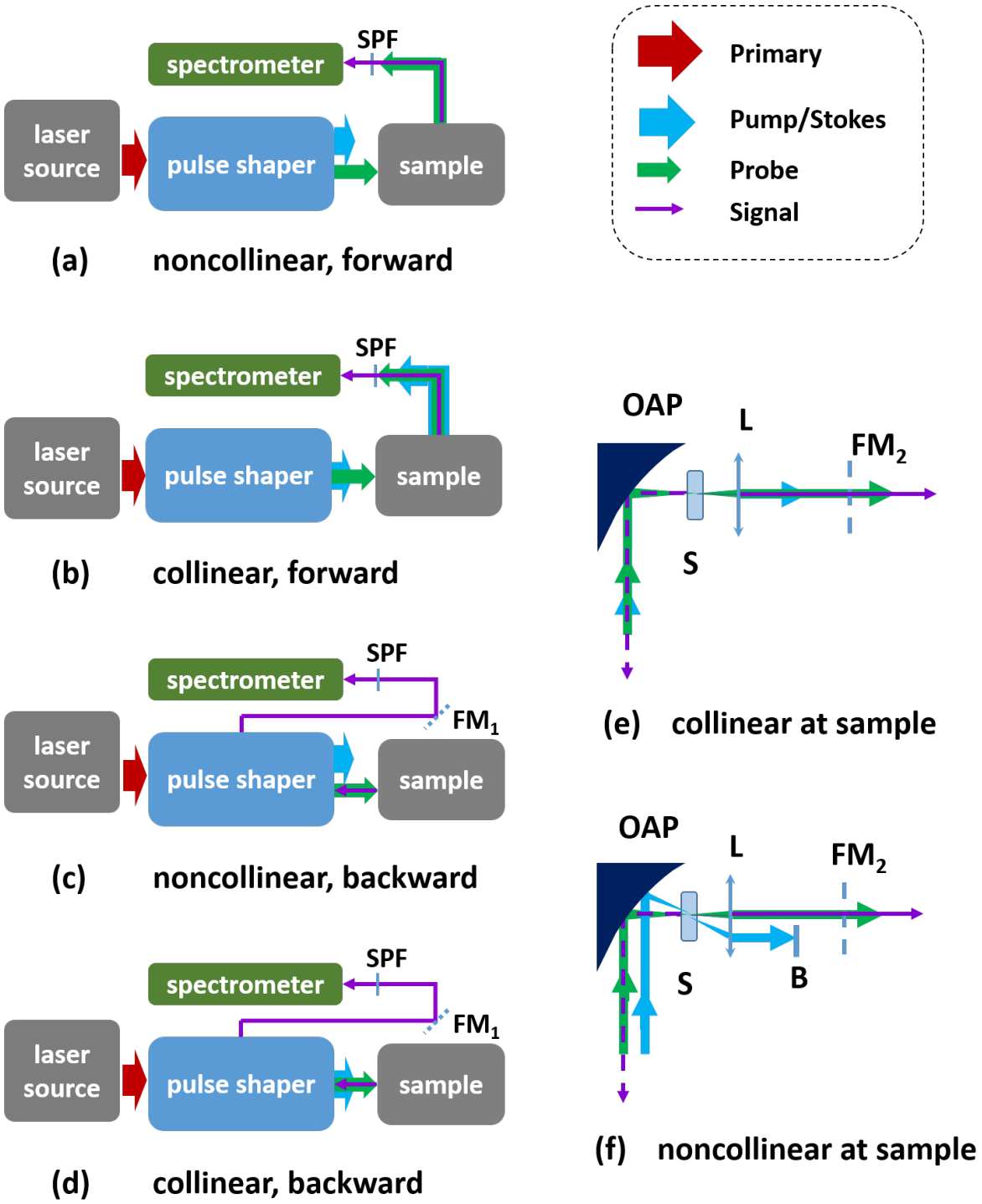

Figure 3.2: Versatile experimental setup for FAST CARS. (a)-(d) Block diagram schematics of different beam configurations and detection schemes. Beams are represented by their colors, and the inset shows the corresponding labels: red - primary beam from the source; blue - pump/Stokes; green - probe; purple - signal. Beam geometries at the sample for the collinear (e) and noncollinear (f) configurations are also shown. The dashed lines for the flip mirrors and signal beam mean that they are present only in the backward detection scheme. SPF: short-pass filter, OAP: off-axis parabolic mirror, FM: flip mirror, S: sample, B: beam block, L: lens.

(Surespectrum, Bruker Optics) and CCD detector (iDus420, Andor). On the other hand, in the backward detection scheme, the signal propagated back into the pulse shaper, and the blue-shifted nonlinear signal was picked out and guided to the short-pass filter and spectrometer via another flip mirror. These different beam configurations and detection schemes are shown in Figs. 3.2a-3.2d.

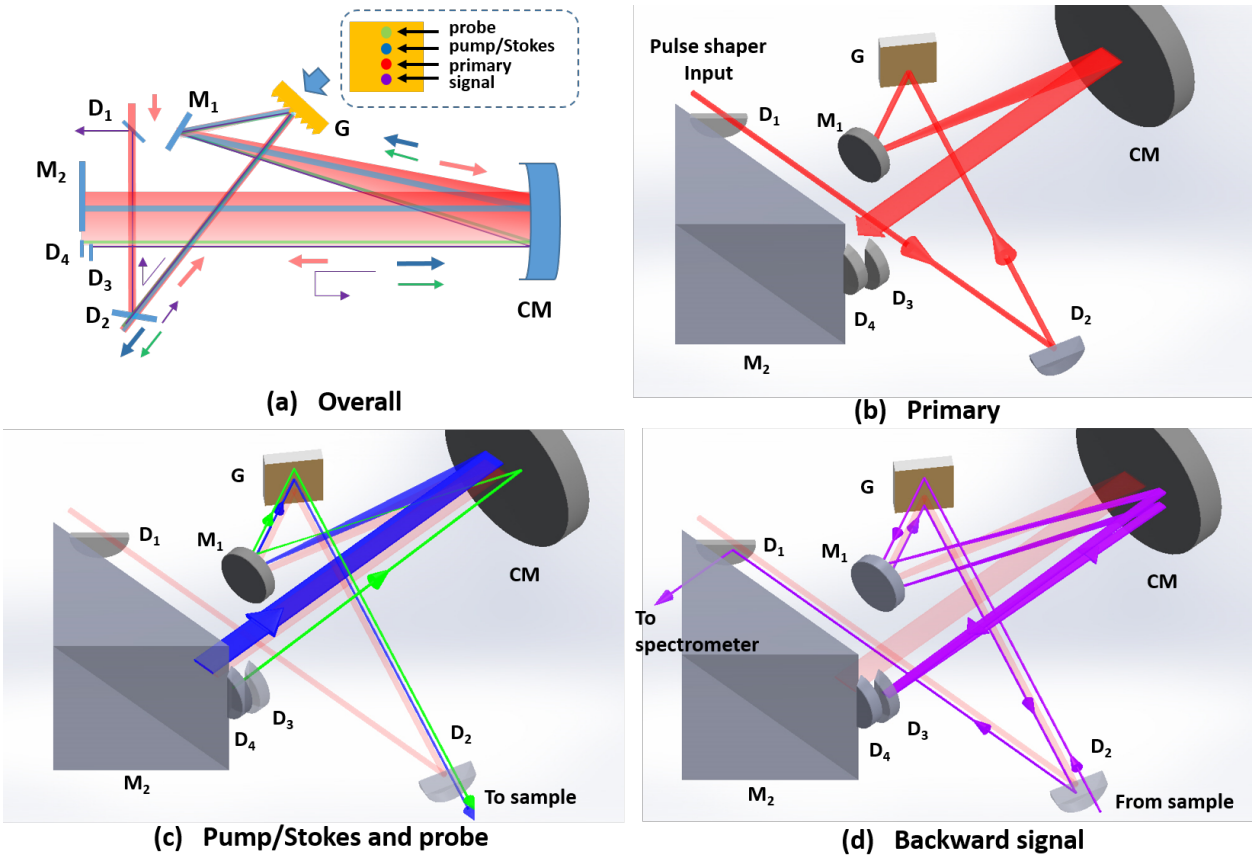

Figure 3.3: Beam propagation schemes inside the pulse shaper of the FAST CARS setup, for the noncollinear backward detection case. The beam colors and labels are the same as in Fig. 3.2. (a) Sketch of the overall setup, and inset shows beam spots on the grating surface. (b) Propagation of the primary beam from laser source. (c) Generation and propagation of the pump/Stokes and probe beams. (d) Light path of the backward propagating signal beam. In (c) and (d) the primary beam is also shown (light red). CM: concave mirror; G: grating; M: mirror; D: D-shaped mirror.

The detailed beam propagation scheme inside the pulse shaper is shown in Fig. 3.3a, illustrating the noncollinear backward detection case. The corresponding paths of different beams are shown

in Figs. 3.3b-3.3d. The primary beam was sent above the first D-shaped mirror D_1 (PFD10-03-P01, Thorlabs) and was reflected by the second D-shaped mirror D_2 into the pulse shaper. The pulse shaper used a folded geometry, consisting of a 830 grooves/mm grating (43-850, EdmundOptics), a folding mirror, a 3-inch-diameter concave mirror (CM) with a focal length of 500 mm (Thorlabs), and three reflectors in the vicinity of the Fourier plane — i.e. a prism mirror (47-308, EdmundOptics) M_2 and two D-shaped mirrors D_3 and D_4. The primary beam was dispersed by the grating, guided by the folding mirror to the CM, and the focus of different frequency components were spatially separated, as shown in Fig. 3.3b. A major part of the beam at the low-frequency side was reflected by M_2, serving as the pump/Stokes beam. D_3 was shifted slightly right to D_4, so that a narrow-band portion of light passing the edge of D_3 and hitting D_4 was reflected and used as the probe beam. D_4 was mounted on a translation stage so that it could be moved back and forth to change the relative delay between the probe beam and the pump/Stokes beam. Figure 3.3c shows the pump/Stokes and probe beam layout. It can be seen that M_2 guided the pump/Stokes beam back with a slightly tilted angle so that this beam hit a spot directly above the primary beam on the grating, and then passed over D_2 and was guided to the sample. The same for the probe beam directed by D_4, but with a larger tilting angle. The inset in Fig. 3.3a shows marked spots on the grating surface, indicating the vertical positions of different beams— with the pump/Stokes spot $\sim$3 mm higher than the primary beam spot, and probe spot $\sim$7 mm above that of the pump/Stokes. Since both beams were reflected close to the Fourier plane, after collimation by the CM and the grating, they propagated in parallel to the sample, therefore achieving the noncollinear configuration. The collinear configuration was achieved simply by tilting M_2 so that the pump/Stokes spot coincided with that of the probe. With a total incident power of 110 mW on the primary beam, the power of the pump/Stokes and probe at the output of the pulse shaper was 31 mW and 450 μW, respectively.

The pulse shaper was also used to guide the backward-propagating signal as demonstrated in the previous chapter. The back-scattered light path is shown in Fig. 3.3d. The signal followed the path of the probe but in the opposite direction, dispersed by the grating, guided by the folding

mirror to the CM, and then separated into different frequency components in the Fourier plane. Since the nonlinear signal was blue-shifted from the probe, it would encounter D_3, which was aligned such that the back-scattered signal would hit a spot $\sim$3 mm below the primary beam spot on the grating, therefore propagating in parallel with but opposite to the primary beam, and with a finite spatial separation. The signal was then reflected by D_2 and guided out by D_1 to the short-pass filter and the spectrometer for detection.

3.2.2 Result analysis

Raw data obtained from TeCA using the forward detection scheme are shown in Fig. 3.4. Figure 3.4a corresponds to the noncollinear configuration, and Figs. 3.4b and 3.4c are the collinear configuration results. In the bottom panel of Fig. 3.4a, a spectrogram showing the anti-Stokes signal spectrum versus the probe delay in the noncollinear configuration is plotted. Each spectrum was taken with a 10 s integration time, and averaged over 10 times. The tail-like features at 767 and 749 nm in the plot are the signature of FAST CARS signals, indicating long-lived vibrational coherence as compared to the nonresonant background. The top panel of the graph shows the variation of signal at 779 nm versus the probe delay. Since there is no strong Raman line at this wavelength, this variation can be seen as an indication of the nonresonant background strength. The curve in the top panel reveals the sinc-shape behavior of the background intensity: first attaining its maximum at zero delay, then decreasing, reaching the first node; and then increasing again to the second, smaller maximum. The optimal delay is at the first node position at $\sim$1 ps where the background is largely suppressed, therefore yielding the maximum signal-to-background ratio.

In Figs. 3.4b and 3.4c we show the data using the collinear configuration with 0 ps and 1 ps probe delay, respectively. Similar to previous works [81, 95], here the detection was intrinsically heterodyne, with the FWM generated by the pump/Stokes beam serving as the LO. This guaranteed higher signal level, and enabled faster detection speed. Each spectrum was acquired with 20 ms integration and averaged over 100 times. In order to retrieve the CARS signal, a baseline spectrum of the LO was needed, and was acquired at relatively long delay (3.5 ps) where the vibrational signal contribution was negligible and the FWM by the pump/Stokes pulse was dominant. The

final spectrum in the collinear configuration could be obtained by subtracting this background from the raw data.

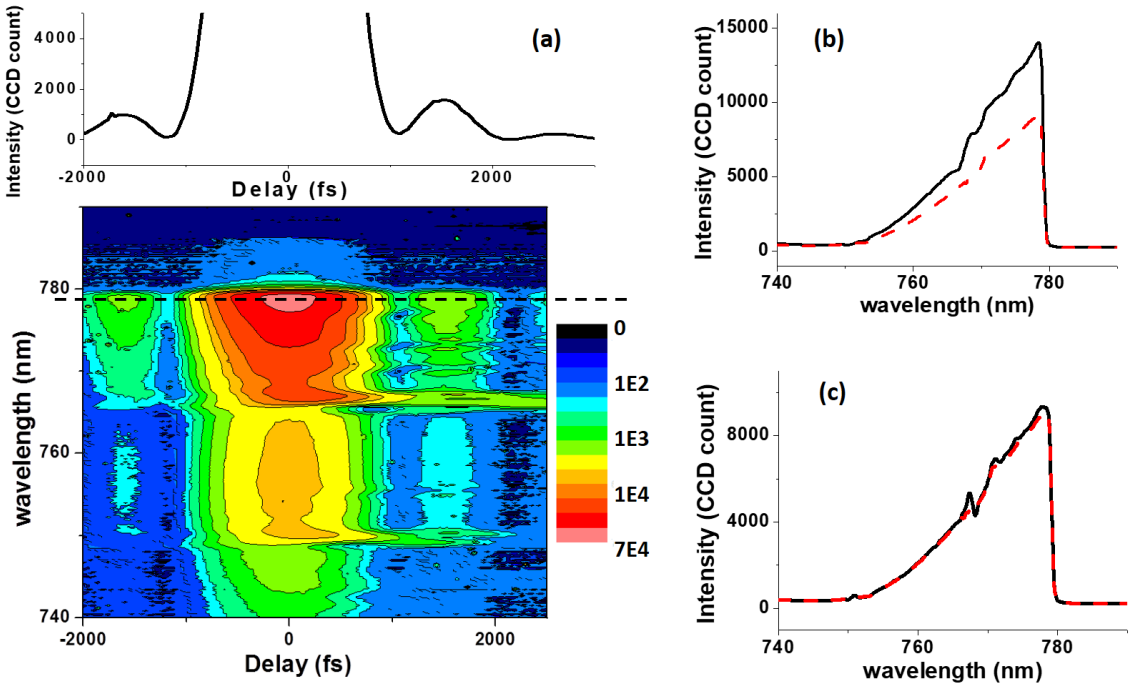

Figure 3.4: Forward detection results from TeCA. Bottom panel in (a) shows a 2D spectrogram of the FAST CARS signal versus the probe delay in the noncollinear configuration. Colors represent signal strength in log-scale. Top panel in (a) shows the signal intensity at 779 nm at different delays, corresponding to the horizontal cross-section in the 2D spectrogram (marked by the black dashed line). Raw data of TeCA signal (solid black) at zero (b) and 1 ps delay (c) in the collinear configuration are also plotted, with the long-delay (3.5 ps) baseline signals in dashed red.

The processed spectra of TeCA at zero and at the optimal 1 ps delay using different beam configurations and detection schemes are shown in Fig. 3.5. The left and right column correspond to spectra with zero and 1 ps probe delay, respectively. Figures 3.5a and 3.5b, representing the noncollinear configuration and forward detection, were directly obtained from the 2D plot in Fig. 3.4a by taking the spectra (vertical cross-section) at zero and 1 ps delay, respectively. Clearly the nonresonant background in Fig. 3.5a is dominating at zero delay, and only the strongest peaks at

353 cm^{-1} and 650 cm^{-1} are visible. However with the 1 ps delay, we obtained peak structures that matched well with the spontaneous Raman spectrum of TeCA [86], marked by blue vertical lines. The minor deviations are due to the finite spectral resolution and lineshape distortions. Figures 3.5c and 3.5d, representing the collinear configuration, were obtained by taking the difference between the raw data and the baselines in Figs. 3.4b and 3.4c, respectively. For zero delay, Fig. 3.5c displays a sharp edge corresponding to the major peak of TeCA at 353 cm^{-1}, while the rest of the Raman structures are not visible due to the large background; on the other hand, the 1-ps-delay result reveals these other peaks in Fig. 3.5d. However, due to the interference of the signal and background, some peaks have a dispersive line shape, and will need further processing to retrieve the Raman lineshape [52].

Results for the detection of backward-propagating signals are shown in Figs. 3.5e-3.5h, with the same integration time and averaging setting as previous. Due to the finite size of mirror D_3, the detection range in the high frequency region had a cut-off around 766 nm, corresponding to the 400 cm^{-1} edge from the zero-delay data in Figs. 3.5e and 3.5g. The backward signals from TeCA shown in Figs. 3.5f and 3.5h shared a similar shape as that in the forward detection, but was attenuated by a factor of 3. During the acquisition of the collinear configuration spectra in Figs. 3.5g and 3.5h, the probe was red-shifted to 792 nm, as opposed to the 789 nm used in the previous figures, therefore leading to the change of the low-wavenumber-cutting-edge towards larger Raman shift, and the disappearance of the 173 cm^{-1} peak. Still, we can see from the above TeCA results that the FAST CARS provided significant nonresonant background suppression, leading to enhanced signal-to-background ratio.

We also performed backward detection of crystalline sulfur using the collinear configuration. The results are shown in Fig. 3.6, in which we compare signals obtained with and without probe delays. The sulfur crystal produced a genuine epi-CARS signal with two major Raman peaks resolved through the appropriate probe delay, as seen in Fig. 3.6(b), which agreed well with its spontaneous Raman data [96]. Again we can see that probe delay helped to suppress the nonresonant background. The sulfur spectra were acquired with 100 ms integration time and averaged

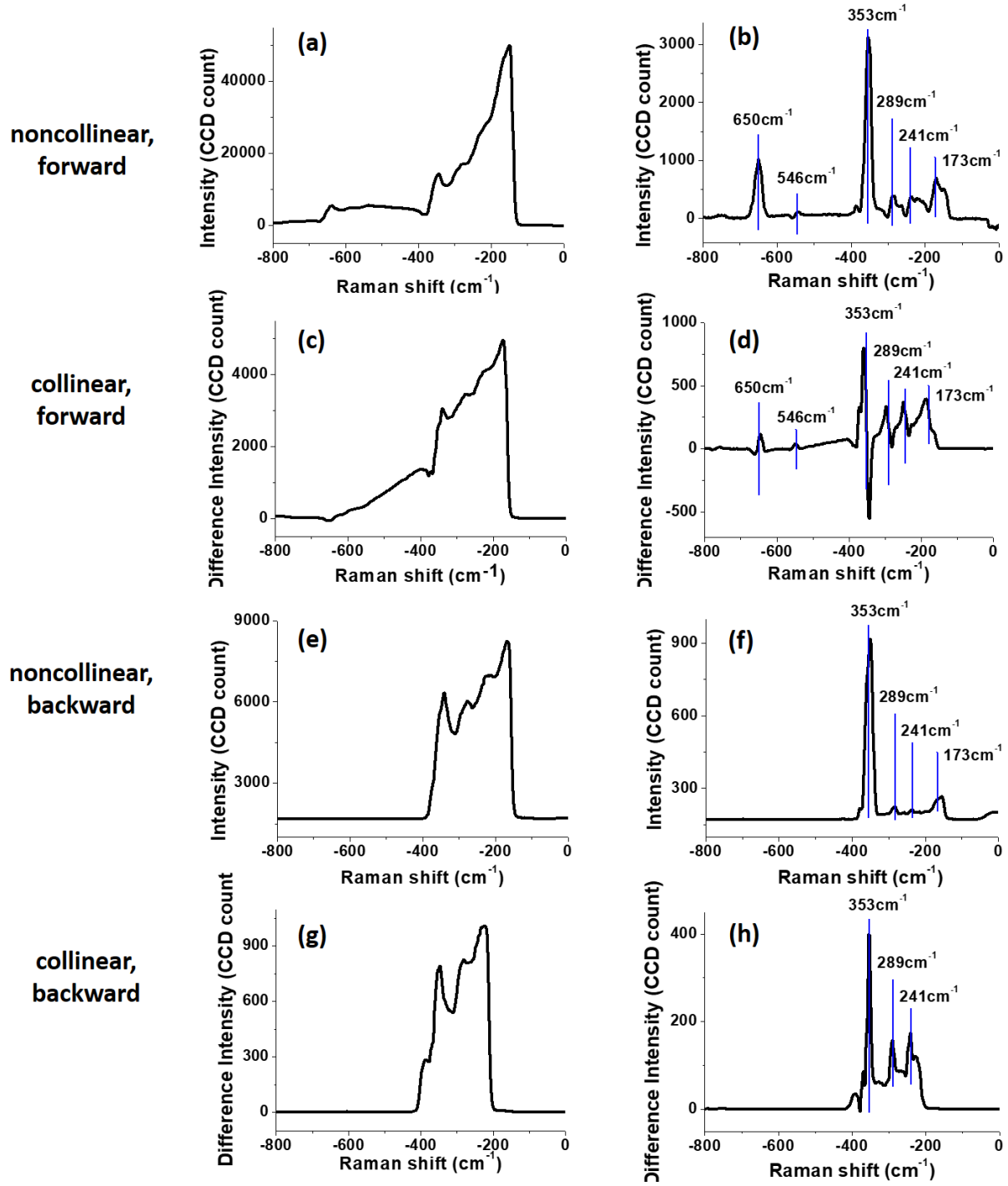

Figure 3.5: FAST CARS spectra of TeCA at zero (left column) and 1 ps (right column) delay using different beam configurations and detection schemes labeled below the spectra. These results correspond to configurations in Fig. 3.2. Spontaneous Raman transitions of TeCA are marked by thin blue vertical lines.

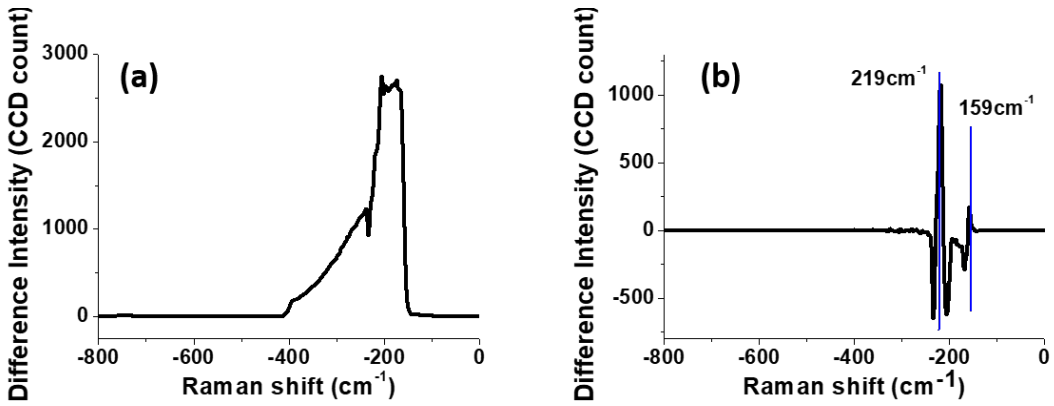

Figure 3.6: Signal spectra comparison of zero delay (a) and 1 ps delay (b) of sulfur crystal, using the collinear configuration and backward detection. Spontaneous Raman peaks of sulfur are marked by blue vertical lines.

over 10 times.

3.2.3 Discussions

The single-beam FAST CARS setup shown above surpasses our previous setups [40, 81] in its simplicity in construction, and its versatility in switching between different configurations. The simplicity is two-fold: first, the pulse shaper is consisted of only basic optical components, which makes the setup more accessible as opposed to those incorporating SLMs; second, the spatial and temporal overlap alignment is straightforward. For spatial overlap, by coarse alignment of the pump/Stokes and the probe spots onto the same vertical line on the grating, we can achieve a signal level more than one third of that after fine tuning. The temporal overlap alignment is also facilitated by the proximity of the two reflectors. Therefore the initial coarse positioning is only a few millimeter away from the preferred temporal overlap for FAST CARS. Moreover, tilting only the vertical knob of the mirror M_2 allows switching from the noncollinear to the collinear configuration, and no additional spatial alignment is required.

The collinear configuration outperformed the noncollinear configuration in its detection speed, with close to three orders of magnitude decrease in CCD integration time thanks to the strong FWM signal from the pump/Stokes beam. Also, because of the increasing FWM intensity close to the probe, low-wavenumber signals see more amplification than higher-wavenumber signals, as

seen for the TeCA peaks below 200 cm^{-1}. The downside is that when moving away from the probe, signals are less visible, therefore limiting the detection range. One solution to this nonuniform LO problem would be to use the short-wave side of the input pulse as the LO [71], with appropriate attenuation to create a 'flat top' spectrum. This, on the other hand, may result in a stronger LO compared to the FWM from the pump/Stokes beam, and would require detectors with a larger dynamic range.

Another problem in using the heterodyne technique is the instability due to interference. While this is usually not a problem for uniform samples like liquids and crystals, it makes the detection of highly scattering powder samples rather challenging, as multiple scattering inside a sample makes the spectra unstable, and therefore the difference spectra will contain lots of ripple-like noise that veils the signal. A good solution is to use a probe with frequency sufficiently away from the pump/Stokes so that the signal is generated at new frequencies that can be separated from the background [97]. With a supercontinuum source and modified dispersion schemes (e.g. using a prism or an echelle grating), such a solution can be incorporated into our setup.

Next we note the necessity of the long-pass filter. The high frequency part of the primary beam that coincides with the signal region is reflected by D_3 at a different angle, and therefore will not enter the spectrometer directly. But a small portion of this light will scatter from the surface of D_3, which may be stronger than the CARS signal generated in the noncollinear configuration and is generally comparable to or even stronger than the FWM from the pump/Stokes beam. This will then produce a significant background. While it is still possible to perform the collinear configuration measurements in such a case, it is generally desirable to have the long-pass filter to get rid of the unwanted light and obtain a cleaner background in the signal range.

The current setup maintains the advantage of the enhanced backward detection efficiency as in the previous setup as compared to a beam-splitter-based backward collection scheme [81]. And similar to the previous work, the short-pass filter can, in principle, be removed in the backward detection scheme, since the pulse shaper itself acts as a short-pass filter. Still we are limited by the long-pass filter edge to achieve the extremely low-wavenumber detection mentioned in the previous

work. Also the beam size in the present setup is reduced to fit the noncollinear configuration, which leads to poorer frequency resolution in the Fourier plane. The setup can be modified to use an unfolded pulse shaper, which would then be able to achieve filterless and efficient low-wavenumber detection, at the cost of increased complexity and additional alignment in the pulse shaper.

The collinear setup configuration may be coupled into a microscope for fast imaging. With larger input beam size and a large N.A. objective lens for focusing, the nonlinear signal can be generated efficiently. Moreover, larger input beam size would provide higher resolution in the Fourier plane and therefore a sharper spectral edge, which is beneficial for both pulse shaping and enhancing the detection range. On the other hand, although we have only used oscillator pulses at high repetition rate, the present setup can also work with amplified pulses to achieve single shot detection or imaging. Also the signal strength may be enhanced by incorporating plasmonic enhancement, as was previously shown in a related time-resolved surface-enhanced collinear CARS scheme [98].

As a summary, we have demonstrated a versatile setup for FAST CARS in this section, which is simple to build and is less demanding in terms of alignment. We performed spectral measurements on both liquid TeCA and crystalline sulfur samples, using the forward and backward detection schemes. The spectra obtained with the optimized probe delay provided background suppression and increased visibility of CARS signals. We have also shown the higher acquisition speed of the collinear configuration compared to the noncollinear configuration. Yet the former requires a dedicated background collection stage in order to retrieve the CARS spectra, which can be further simplified as we will show in the following section.

3.3 Heterodyne single-beam FAST CARS

We have previously demonstrated two single-beam CARS systems capable of heterodyne detection, which include using the FWM background generated by the pump/Stokes as the LO and therefore ensure stability [99]. However, the retrieval method requires either shifting the position of a needle tip [81] or delaying the probe to a large extent so as to obtain the baseline [93],

which leads to low acquisition speed and lineshape distortion as seen in Figs. 2.4d and 3.5d. To resolve these issues, we can exploit the phase relation between the FAST CARS signal and the LO and implement heterodyne detection with fast modulation of the probe delay. The idea of single-beam heterodyne CARS has been experimented earlier using chopper-based single-channel detection [71], and heterodyne-based multiplex CARS has also been demonstrated by dividing the femtosecond pulse into a broadband low-frequency pump/Stokes, a narrowband probe, and a high-frequency LO, and the CARS signal was retrieved via double quadrature spectral interferometry (DQSI) method [75].

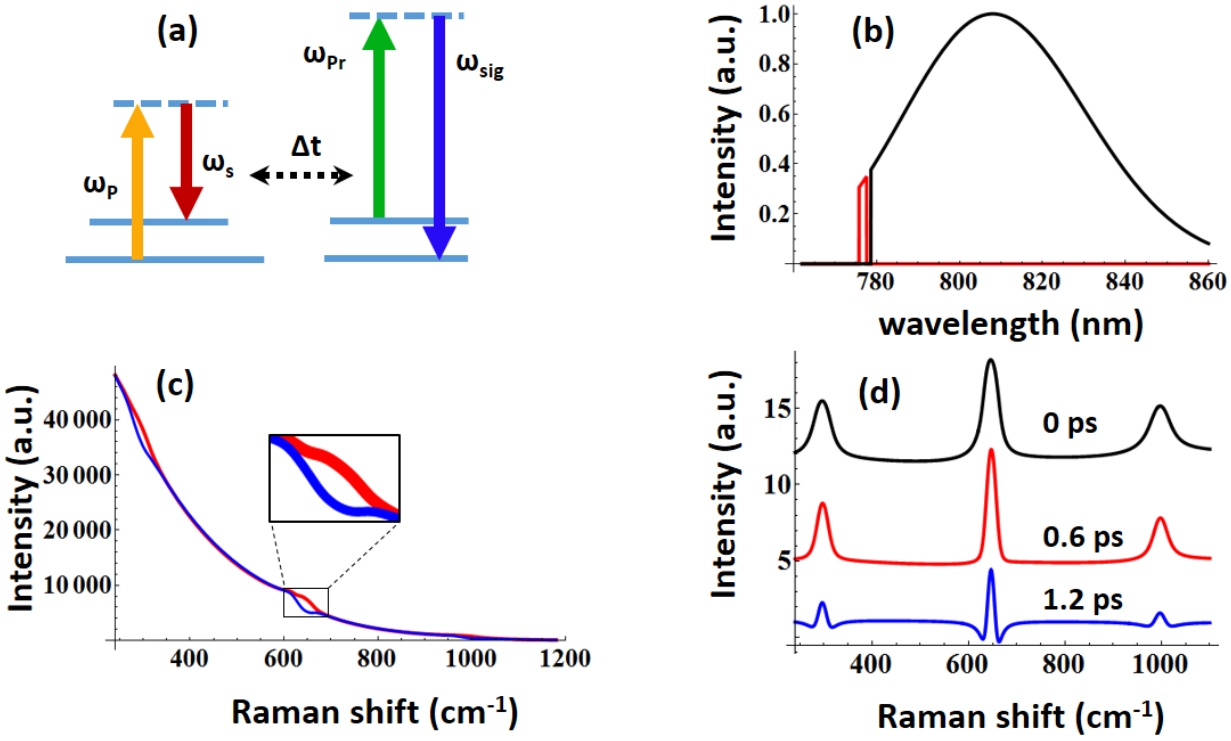

Figure 3.7: Schematic of the single-beam heterodyne FAST CARS. (a) Energy diagram of the FAST CARS scheme. (b) Spectral intensity of the excitation pulse with the probe and pump/Stokes parts marked with red and black lines, respectively. (c) Anti-Stokes signals $I_+(\omega)$ (red) and $I_-(\omega)$ (blue) simulated corresponding to delays $\tau_0 + \delta\tau$ and $\tau_0 - \delta\tau$, respectively, with $\tau_0 \approx 0$. Inset shows the constructive (red) and destructive (blue) interferences between the FAST CARS signal and the four-wave mixing local oscillator. (d) FAST CARS signal retrieved from the spectra in (c) using Eq. (3.1).

Based on these earlier designs and our previous setup, we demonstrate single-beam heterodyne FAST CARS microscopy through precise control of the probe delay, which in turn affects the phase relation between the signal and the LO. The energy level diagram of the heterodyne FAST CARS scheme is shown in Fig. 3.7a, and the spectral intensities of the probe and the pump/Stokes field are plotted in Fig. 3.7b. In addition to the large-scale delay controlled by the motorized actuator described in the previous section, we added a piezo actuator for fine tuning the delay. By modulating the probe mirror position locally within a fraction of the wavelength, we switched the probe delay between two close values $\tau_0 + \delta\tau$ and $\tau_0 - \delta\tau$, and obtained two spectra $I_+(\omega)$ and $I_-(\omega)$, respectively. Here τ_0 denotes the central delay value and $\delta\tau$ is the modulation amplitude. By careful selection of τ_0 and $\delta\tau$, $I_+(\omega)$ and $I_-(\omega)$ will correspond to the constructive and destructive interference between the FAST CARS signal and the LO, as shown by the simulation data in Fig. 3.7c. Then by using a modified DQSI method [74, 75]:

$$I_{CARS} = \frac{I_+(\omega) - I_-(\omega)}{\sqrt{I_+(\omega) + I_-(\omega)}}, \tag{3.1}$$

fast reconstruction of the vibrational signal and subtraction of the nonresonant background can be achieved, resulting in CARS peaks with good visibility as shown in Fig. 3.7d. A more detailed theoretical treatment will be provided at the end of this section. In addition, an improved epi-detection efficiency is obtained by incorporating the spectral detection into the pulse shaper, which reduces redundant optical components, such as an external spectrometer and collimation optics[81, 93]. This compact design can be used to construct an improved CARS microspectroscopy system.

3.3.1 Setup description

The sketch of our experimental setup is shown in Fig. 5.1, with a similar pulse shaper design as that in Fig. 3.3. Again, the Ti:Sapphire oscillator (TS laser kit, KMLabs) was pumped by a green laser (Millenia eV, Spectra Physics) to produce 25 fs pulses centered around 810 nm, with a repetition rate of 85 MHz. A variable ND filter was used for attenuation, and followed by a chirp mirror pair (DCMP175, Thorlabs) for dispersion compensation. Then high-frequency parts

of the pulses that coincided with the CARS signal was blocked by a long-pass filter (LP02-785RU-25, Semrock), and the pulses were sent to the pulse shaper where its spectrum was dispersed across the Fourier plane. Similar to the previous setup shown in Fig. 3.3, a mirror M_1 reflected a majority of the light on the low-frequency side, which was used as the pump/Stokes field, and a narrowband portion was reflected by the mirror M_2, serving as the probe. A right angle mirror M_3 was placed closely in front of M_2 such that the edges of M_2 and M_3 determine the bandwidth of the probe, which was chosen to be 30 cm^{-1}. M_2 was mounted on a linear stage with a motorized actuator for coarse tuning, and a piezo actuator for fine tuning the delay τ_0 and the modulation $\delta\tau$. The following procedure was carried out to determine the relative position between M_1 and M_2: we used distilled water as the sample, and a large range of probe delays was scanned using the motorized actuator, with spectra taken at each increment of the stepper motor. Then by plotting the signal intensity versus the probe delay at different wavelength, we retrieved a fringe pattern resulting from the interference between the LO and the nonresonant signal generated by the probe. The envelope of this pattern indicated the temporal shape of the probe pulse, which was similar to that shown in Fig. 3.5a. We determined the zero delay position from the peak point of this envelope. Then the probe delay value τ_0 could be calculated according to the motorized actuator shift from the zero delay position. Also, the optimal modulation amplitude for the piezo actuator was found to be $\sim$190 nm, corresponding to $\delta\tau \approx 1.3$ fs, which maximized the retrieved Raman peaks.

The reflected beams from M_1 and M_2 were tilted so that they could be guided out collinearly and sent to the microscope. Both beams were focused on the sample by an objective lens (N40X-NIR, Nikon). For transparent samples, the transmitted light was collected by another objective (LPlan50X, Nikon) and sent through a short-pass filter (TSP01-790-25x36, Semrock) before entering the spectrometer (SureSpectrum, Bruker Optics) for detection; for opaque samples, back-scattered light was collected by the same focusing objective and guided back into the pulse shaper. After reaching the Fourier plane, the blue-shifted signal was directed to the telescope consisting of the concave mirror CM_2 and the lens L, and imaged using a CCD camera (Spec10, Princeton

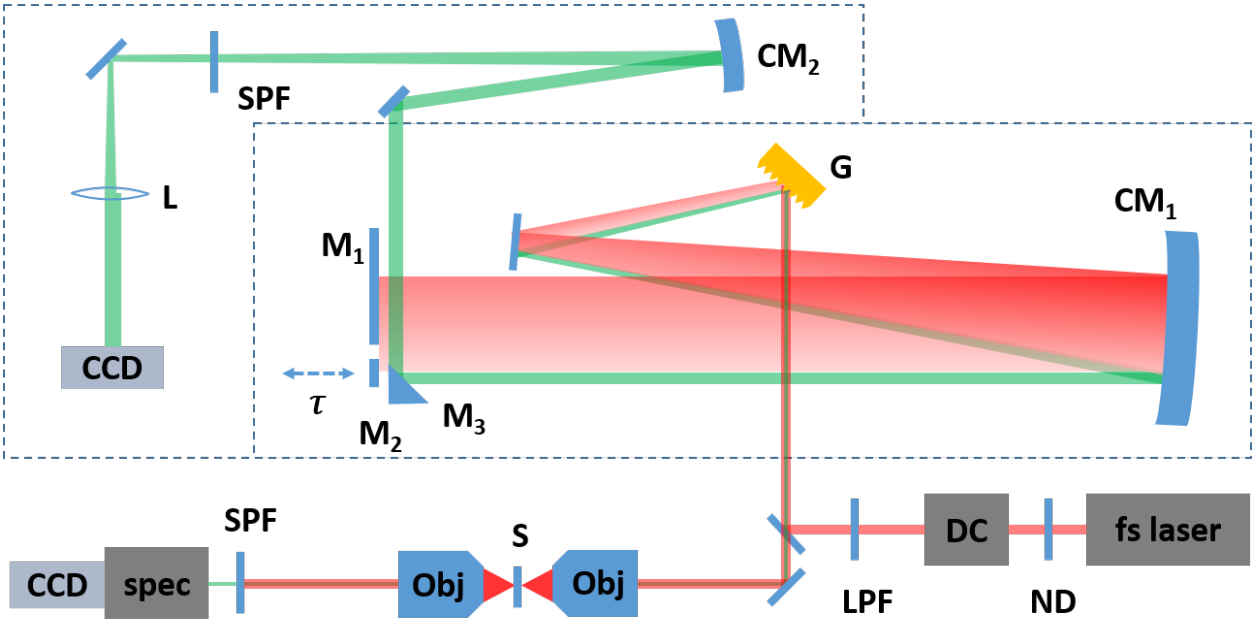

Figure 3.8: Experimental setup: DC, dispersion compensation using chirp mirror pair; LPF, long-pass filter; G, grating; CM, concave mirror; M, mirror; SPF, short-pass filter; L, lens; Obj, microscope objective; S, sample on X-Y translation stage; spec, spectrometer. The excitation and FAST CARS beams are shown by red and green colors, respectively.

Instruments). The focal lengths of CM_2 and L were 500 mm and 200 mm, respectively. The same short-pass filter was placed inside the telescope for filtering the residual excitation light. The Raman shifts were calculated using the frequency shift from the probe central wavelength, which was measured by the forward arm spectrometer.

Samples used for detection include TeCA and CCl_4 (Sigma Aldrich), and fused silica sample was from UV-grade window (Newport). Also, structured silicon (Si) sample was prepared using e-beam lithography on Si wafer with the poly(methyl methacrylate) (PMMA) patterned mask followed by 50 nm thick gold coating, and MoS_2 flakes were prepared by exfoliation of bulk MoS_2 using tape onto a Si substrate. TeCA, fused silica, and CCl_4 were transparent samples and were measured in the forward direction; Si and MoS_2 samples were imaged using epi-detection. The laser power on the sample without attenuation by the ND filter was 50 mW, and typical laser powers used on each sample were 9.8, 8.3, 19.2, 42, and 16.7 mW for CCl_4, TeCA, fused silica, Si, and MoS_2, respectively, except for the power dependent measurement that will be detailed later.

The CCD exposure time for all samples was fixed at 40 ms. CCl_4, TeCA, and silicon spectra were averaged over 10 times, while fused silica and MoS_2 spectra were averaged over 100 times due to their relatively weak CARS signals. During the acquisition the CCD received a trigger frequency of 14 Hz while the piezo was driven at 7 Hz such that the two spectra were collected at constructive and destructive interference positions, from which the FAST CARS signals were retrieved using Eq. (3.1). For comparison, spontaneous Raman spectra were acquired using a commercial Raman system (LabRAM HR Evolution, Horiba).

3.3.2 Results

Result analysis

Results obtained from TeCA are shown in Fig. 3.9, illustrating the effect of the probe delay on retrieved Raman peaks. Figure 3.9a shows the spectrogram of TeCA acquired at different probe delays, from which we can see the tails due to the long-lived coherences of various Raman modes. Nonresonant background was suppressed at all delay values τ_0 thanks to the DQSI method, and we plot three spectra at delays of 0 ps, 0.6 ps, and 1.2 ps in Fig. 3.9b. For comparison, we also plot the zero probe delay spectrum, which is adapted from Fig. 3.5c, in Fig. 3.9c. Here the resonant signal is buried in the large nonresonant background. As the delay τ_0 was increased from 0 ps to $\tau_0 \approx 0.6$ ps, the height of the main peak around 353 cm^{-1} had increased by $\sim$30%, and its FWHM decreased from 32 cm^{-1} to 21 cm^{-1}. Other peaks showed similar behavior, and the effect is similar to the π-step-phased probe case depicted in the previous literature [100]. Also noticeable are the lineshape distortions to the retrieved peaks, with dispersive shapes forming on both sides of the 353 cm^{-1} peak at 0.6 ps delay. When the delay was further increased to $\tau_0 \approx 1.2$ ps, the distortion became so large that the peak height information was lost, but the central peak became more distinct. One interesting point to note is that, besides the main peak at 353 cm^{-1}, there is also a spectral structure appearing at 370 cm^{-1}. The origin of this minor peak could be the 366 cm^{-1} vibrational mode of TeCA, whose spontaneous Raman spectrum is shown in Fig. 3.9d. We suggest that at large τ_0 values, the delay induces a spectral phase across the probe spectrum and

modifies its interaction with the nonlinear susceptibility, which can lead to the appearance of the doublet structure that would otherwise be hidden as in the zero probe delay case.

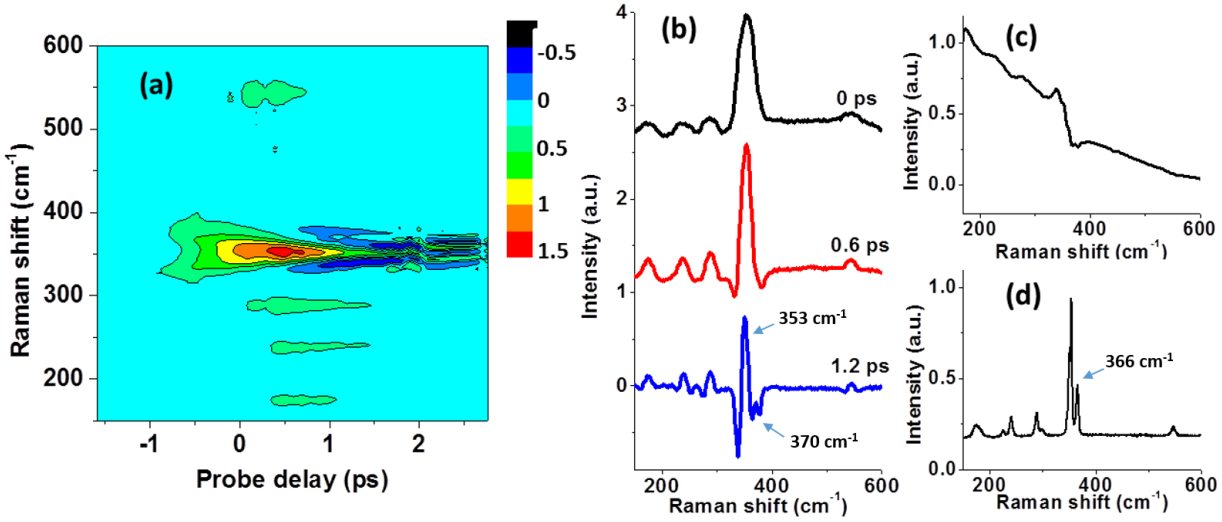

Figure 3.9: Single-beam heterodyne FAST CARS of TeCA using the forward detection: (a) 2D plot of the heterodyne FAST CARS spectra at different probe delays. (b) Heterodyne FAST CARS signal at 0 (black), 0.6 (red), and 1.2 ps (blue) delay. (c) FAST CARS signal of TeCA at zero probe delay from Fig. 3.4b. (d) Spontaneous Raman spectrum of TeCA. Spectra in (b) are normalized by the same factor.

Next we carried out measurements probing coherence lifetimes of the Raman modes in fused silica. It was previously shown that fused silica contained a broadband vibration mode with a short decoherence time, denoted as ω_1 [101]. The retrieved FAST CARS signals of fused silica at different probe delay times are shown in Fig. 3.10. We identify the ω_1 band as the broad feature in the range between 200 cm^{-1} and 440 cm^{-1}. As the probe delay increased, this band intensity gradually decreased, and only the narrow peak due to the four-fold ring structure at 495 cm^{-1} [101] was preserved. The coherence lifetime of the ω_1 band was estimated to be shorter than 1 ps due to the convolution of the FAST CARS signal with the probe temporal shape, which limited the temporal resolution to $\sim$1 ps. Still, better resolution can be achieved through more careful shaping

of the probe pulse.

We used CCl_4 as the test sample to verify the power and concentration dependence. Because the raw signal intensities $I_{\pm}(\omega)$, generated by third-order nonlinear process, are proportional to the third power of the total input laser intensity $I_{\pm}(\omega) \propto (\text{Input power})^3$, then from Eq. (3.1) the retrieved signal has a 1.5th-power dependence on the input power:

$$I_{CARS} \propto (\text{Input power})^{1.5}. \tag{3.2}$$

On the other hand, we expect a linear dependence on the concentration for heterodyne detection [91]. Figure 3.11a shows the retrieved spectrum from CCl_4 at zero probe delay. Figures 3.11b and 3.11c show the signal dependence on the input power and concentration, respectively, on a log-log scale. The units for the input power and concentration were mW and percentage, respectively. The input laser power was measured before entering the pulse shaper, and Fig. 3.11c was obtained using different concentrations of CCl_4 in acetone at fixed laser power. The intensities shown in Figs. 3.11b and 3.11c correspond to the 459 cm^{-1} transition of CCl_4. The slopes of the fitting curves in Figs. 3.11b and 3.11c are measured to be 1.49 ± 0.02 and 1.04 ± 0.05, respectively, which agrees with the theory. Other transitions showed similar behavior.

Finally we demonstrate the epi-detection capability of the setup by imaging microscopic structures of the gold-coated Si and MoS_2 flakes. The samples were scanned using piezo-driven stages, and characteristic peak intensities at 1 ps probe delay value at each spatial location were collected to obtain the FAST CARS images. Figures 3.12a and 3.12d are the microscopic optical images of the Si and MoS_2 samples, respectively, with scan areas marked by red rectangles. Figures 3.12b and 3.12e compare two FAST CARS spectra acquired at different pixels from the two samples, with one pixel containing the target substance and the other not. The characteristic Raman peak values used for imaging are 520 cm^{-1} for Si and 385 cm^{-1} for MoS_2, the latter corresponded to the E_{2g} transition of MoS_2. The retrieved FAST CARS images are shown in Figs. 3.12c and 3.12f, which are in good agreement with the optical images for both samples.

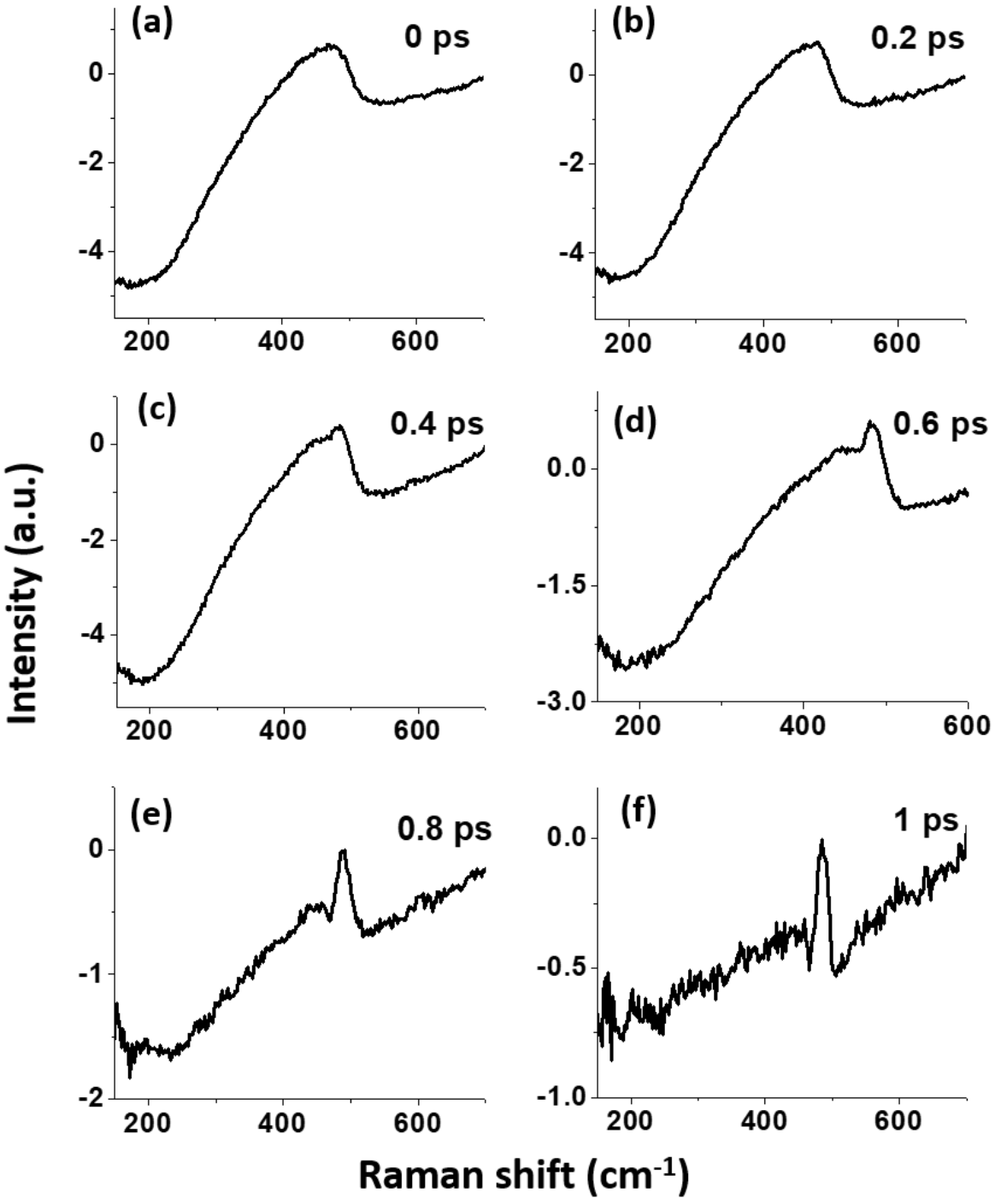

Figure 3.10: Heterodyne FAST CARS spectra of fused silica using the forward detection at different probe delays: (a) 0 ps, (b) 0.2 ps, (c) 0.4 ps, (d) 0.6 ps, (e) 0.8 ps, and (f) 1 ps.

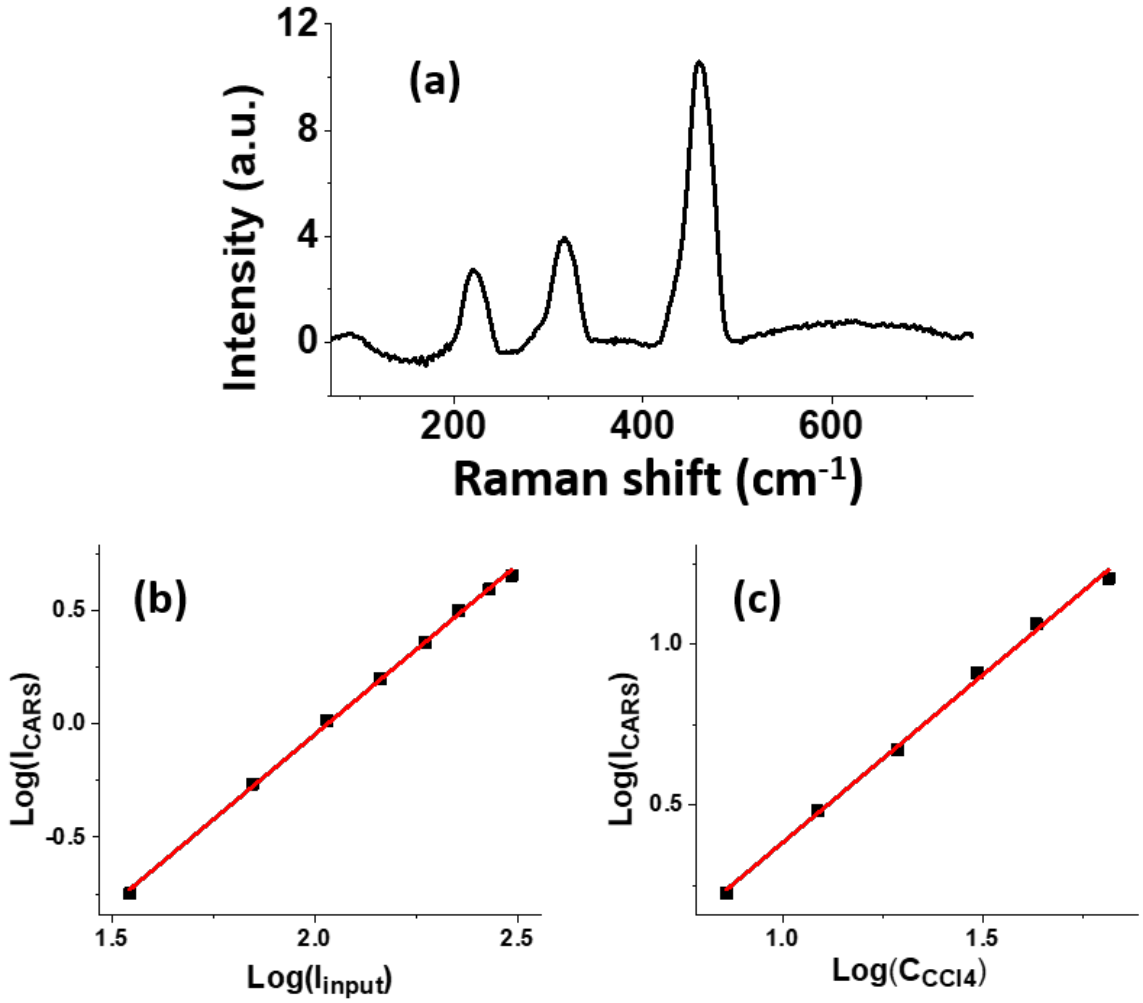

Figure 3.11: Input power and concentration dependence of the CCl_4 FAST CARS signal measured in the forward detection. (a) Retrieved FAST CARS spectrum from CCl_4 at zero probe delay. (b) Log-log plot of the intensity of the 459 cm^{-1} peak as a function of the laser power. (c) Intensity of the 459 cm^{-1} peak measured at different concentrations of CCl_4 in acetone.

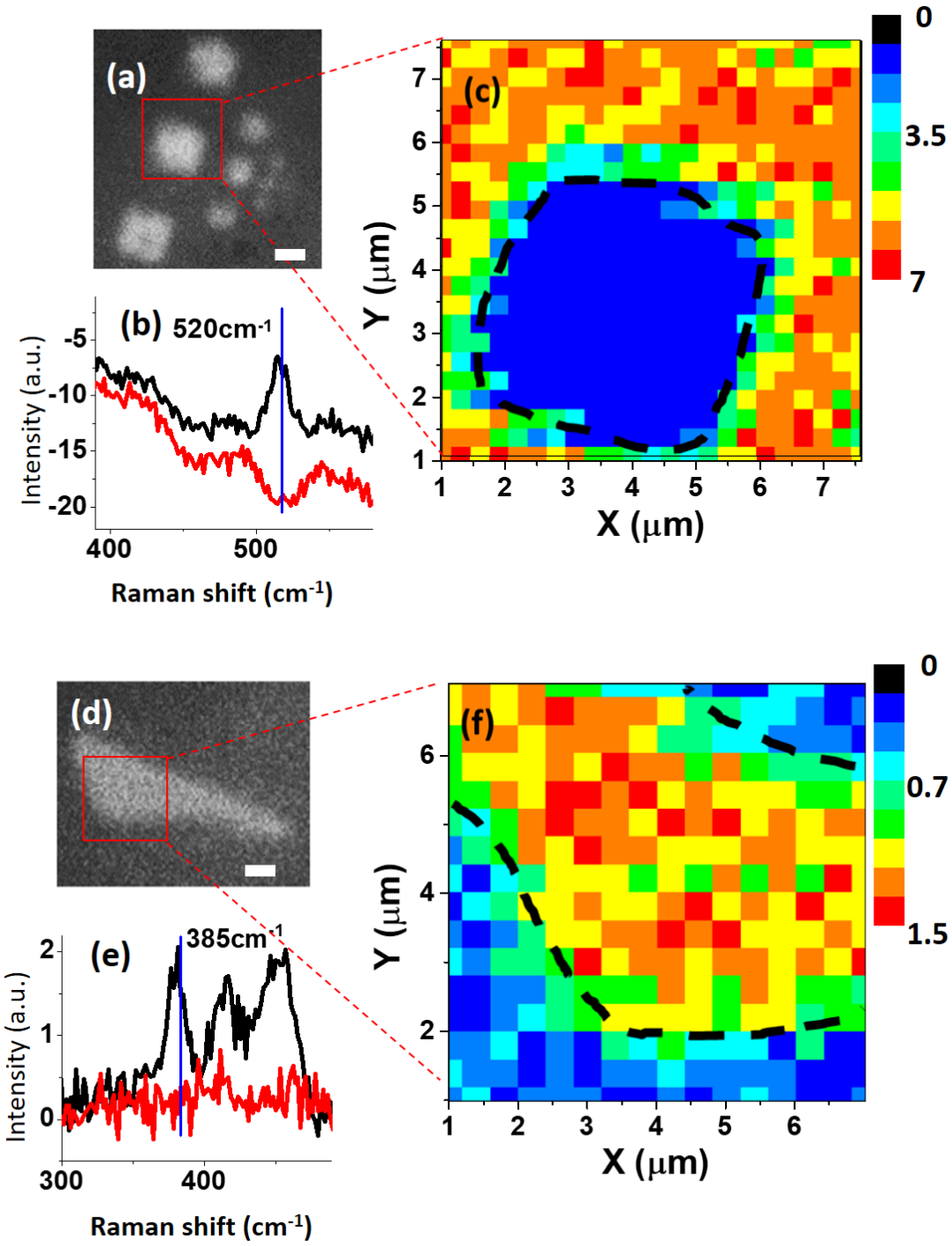

Figure 3.12: Epi-detection FAST CARS microscopy of silicon (Si) and molybdenum disulfide (MoS_2) microstructures. Optical images of the structured (a) Si and (d) MoS_2 flake samples are shown, with scale bars of 2μm. FAST CARS spectra of (b) Si and (e) MoS_2 are plotted in black lines compared to the background (red lines), with corresponding FAST CARS images in (c) and (f), respectively, using the Si peak at 520 cm^{-1} and the MoS_2 peak at 385 cm^{-1}. The two spectra in (b) were acquired at coordinates of (6.4 μm, 6.4 μm) (black) and (4.0 μm, 4.0 μm) (red) in (c), and the two spectra in (e) were acquired at (4.6 μm, 3.8 μm) (black) and (1.0 μm, 2.2 μm) (red) in (f).

Discussions

The appropriate power assignment to the probe and pump/Stokes field could contribute to an enhanced signal level. For the experiment on TeCA described earlier, the total power on the sample was 8.3 mW, with a probe to pump/Stokes power ratio $\sim$ 1:75. By adjusting the ND filter controlling the total power, and by placing another ND filter in front of the M_1 mirror for attenuation of only the pump/Stokes light, we modified the probe to pump/Stokes power ratio to $\sim$ 1:9.3, and the total power on the sample changed to 7.8 mW. We found that, for TeCA, the signal-to-noise ratio of the primary peak at 355 cm^{-1} was doubled as compared to the previous case using 8.3 mW total power but with smaller probe power ratio. Because the LO is also dependent on the pump/Stokes field, careful adjustment is required to reach the optimal ratio between the probe and the pump/Stokes field for the FAST CARS signal retrieval.

The sensitivity and acquisition speed of the current setup can be further improved from various perspectives. Higher pulse energy lasers such as cavity-dumping oscillator [100] or high-repetition-rate regenerative amplifier system [102] could lead to orders of magnitude signal enhancement and therefore less acquisition time with better sensitivity. Also, the piezo actuator controlling the probe mirror can be operated faster than 10 kHz, so higher detection speed can be achieved by adopting high speed detectors like a frame-transfer CCD, scientific CMOS camera, or the recently devised TAMP array [103]. Another limitation concerns the bandwidth —given a broader spectral coverage, the full fingerprint region can be addressed, therefore leading to broader applications in chemistry and biology. Currently we are limited to multiplex detection in the deep fingerprint region, but the setup can be easily modified to adopt broadband sources such as sub-10 fs oscillators [75], or oscillator-pumped supercontinuum [37].

3.3.3 Theoretical treatment

We end this chapter with a detailed theoretical analysis on the heterodyne FAST CARS. We denote $E(\omega)$ as the excitation laser field, which is separated into the probe field $E_{pr}(\omega)$ with a bandwidth of $\delta\omega$, and the pump/Stokes field $E_{ps}(\omega)$, as shown in Fig. 3.7(b). For the transform

limited pulses, the electric fields are taken to have real values. From Eqns 2.2 and 2.3, the nonlinear polarization is given by:

$$P(\omega) \propto \int [E_{pr}(\omega-\Omega)\chi(\Omega) + E_{ps}(\omega-\Omega)\chi(\Omega)]A(\Omega)d\Omega, \tag{3.3}$$

where

$$A(\Omega) = \int E^*(\omega')E(\Omega+\omega')d\omega', \tag{3.4}$$

$$\chi(\Omega) = \chi_{NR}(\Omega) + \chi_R(\Omega) = \chi_{NR}(\Omega) + \sum_m \frac{A_m}{\Omega_{Rm} - \Omega + i\Gamma_{Rm}}. \tag{3.5}$$

Again $A(\Omega)$ corresponds to the vibrational coherence due to impulsive excitation, and $\chi(\Omega)$ is the nonlinear susceptibility, which has a real nonresonant part χ_{NR} and a complex resonant part χ_R containing different Raman modes with frequencies Ω_{Rm}, transition amplitudes A_m, and linewidths Γ_{Rm}. Typical Raman lines come from the imaginary part of this susceptibility Im$[\chi(\Omega)]$. We also denote $P^{ps}_{FWM}(\omega) = \int E_{ps}(\omega-\Omega)\chi(\Omega)A(\Omega)d\Omega$ as the strong FWM polarization generated by the pump/Stokes field in the CARS signal region, which is used as the LO.

When a time delay τ relative to the pump/Stokes field is applied to the probe, it is equivalent to adding a linear spectral phase to $E_{pr}(\omega)$ in the frequency domain, and Eq. (3.3) is modified as:

$$P(\omega) \propto \int E_{pr}(\omega-\Omega)e^{-i(\omega-\Omega)\tau}\chi(\Omega)A(\Omega)d\Omega + P^{ps}_{FWM}(\omega). \tag{3.6}$$

Now we consider two spectra taken at two different delays $\tau_0 + \delta\tau$ and $\tau_0 - \delta\tau$, where τ_0 and $\delta\tau$ are the central probe-delay and the small modulation, respectively. Because the bandwidth of the probe $\delta\omega$ is typically tens of wavenumbers, the phase term $e^{-i(\omega-\Omega)\delta\tau}$ varies little when integrating over the probe region, and therefore can be approximated as $e^{-i\omega_{pr}\delta\tau}$. We assign the following function:

$$f(\omega) \propto \int E_{pr}(\omega-\Omega)e^{-i(\omega-\Omega)\tau_0}\chi(\Omega)A(\Omega)d\Omega, \tag{3.7}$$

so that the two polarizations $P_+(\omega)$ and $P_-(\omega)$, corresponding to the delay $\tau_0 + \delta\tau$ and $\tau_0 - \delta\tau$, can be written as:

$$\begin{aligned} P_+(\omega) = \quad & \{\text{Re}[f(\omega)]\cos(\omega_{pr}\delta\tau) + \text{Im}[f(\omega)]\sin(\omega_{pr}\delta\tau)\} + \\ & i\{\text{Im}[f(\omega)]\cos(\omega_{pr}\delta\tau) - \text{Re}[f(\omega)]\sin(\omega_{pr}\delta\tau)\} + P^{ps}_{FWM}(\omega), \qquad (3.8) \\ P_-(\omega) = \quad & \{\text{Re}[f(\omega)]\cos(\omega_{pr}\delta\tau) - \text{Im}[f(\omega)]\sin(\omega_{pr}\delta\tau)\} + \\ & i\{\text{Im}[f(\omega)]\cos(\omega_{pr}\delta\tau) + \text{Re}[f(\omega)]\sin(\omega_{pr}\delta\tau)\} + P^{ps}_{FWM}(\omega). \qquad (3.9) \end{aligned}$$

For simplicity, we first assume $P^{ps}_{FWM}(\omega)$ to be real. The detected signal intensities $I_+(\omega) \propto |P_+(\omega)|^2$ and $I_-(\omega) \propto |P_-(\omega)|^2$ correspond to the constructive and destructive interference between the signal and the LO, respectively, and the difference is given by:

$$I_+(\omega) - I_-(\omega) \propto |P_+(\omega)|^2 - |P_-(\omega)|^2 \approx 4P^{ps}_{FWM}(\omega)\text{Im}[f(\omega)]\sin(\omega_{pr}\delta\tau), \qquad (3.10)$$

in which we keep only the heterodyne term because $|P^{ps}_{FWM}(\omega)| \gg |f(\omega)|$. Further approximating $P^{ps}_{FWM}(\omega) \propto \sqrt{I_+(\omega) + I_-(\omega)}$, and fixing $\delta\tau = \pi/(2\omega_{pr})$, we obtain from Eq. (3.1):

$$I_{CARS} = \frac{I_+(\omega) - I_-(\omega)}{\sqrt{I_+(\omega) + I_-(\omega)}} \propto \text{Im}[f(\omega)]. \qquad (3.11)$$

The above equation relates the detected CARS signal to the function $f(\omega)$. A closer look at this function in Eq. (3.7) reveals that it is essentially the susceptibility $\chi(\Omega)$ gated by the probe with phase $E_{pr}(\omega-\Omega)e^{-i(\omega-\Omega)\tau_0}$ and a large smooth envelope function $A(\Omega)$. For the ideal probe shape, $E_{pr}(\omega)$ assumes the form of a delta function with infinitely small bandwidth so that $f(\omega)$ reproduces the shape of $\chi(\Omega)$. In reality $E_{pr}(\omega)$ always has a finite bandwidth, leading to a compromised resolution. In the FAST CARS case, it is further complicated by the phase factor $e^{-i(\omega-\Omega)\tau_0}$. Using Eqs. (3.7) and (3.11) we can express I_{CARS} as:

$$I_{CARS} \propto \int E_{pr}(\omega - \Omega)A(\Omega)\{\text{Im}[\chi(\Omega)]\cos[(\omega - \Omega)\tau_0] - \text{Re}[\chi(\Omega)]\sin[(\omega - \Omega)\tau_0]\}d\Omega. \quad (3.12)$$

A simple situation is when τ_0 is small such that $(\omega - \Omega)\tau_0$ does not vary much across the probe spectral region and can therefore be approximated by $\omega_{pr}\tau_0$. Then by choosing $\cos(\omega_{pr}\tau_0) = 1$ the term containing $\mathrm{Re}[\chi(\Omega)]$ in Eq. (3.1) is canceled, and we see that I_{CARS} is directly related to $\mathrm{Im}[\chi(\Omega)]$. In the case of larger delay τ_0, the same condition $\cos(\omega_{pr}\tau_0) = 1$ should be satisfied, so that the nonresonant background term $\mathrm{Re}[\chi_{NR}(\Omega)]\sin[(\omega - \Omega)\tau_0]$ would see an equal contribution from the positive and the negative part of the sine factor when integrating over the spectral region of the probe, therefore yielding negligible contribution.

Next we consider the neglected imaginary part of the LO field $P^{ps}_{FWM}(\omega)$, which is due to the contribution from $\chi_R(\Omega)$ in the expression for $P^{ps}_{FWM}(\omega)$. Consider $P^{ps}_{FWM}(\omega) = |P^{ps}_{FWM}(\omega)|e^{i\theta(\omega)}$, where $\theta(\omega)$ denotes the spectral phase of the LO field. Then the polarizations $P_+(\omega)$ and $P_-(\omega)$ change correspondingly, leading to a modification on the difference term in Eq. (3.10):

$$I_+(\omega) - I_-(\omega) \propto 4\sin(\omega_{pr}\delta\tau)\{\mathrm{Re}[P^{ps}_{FWM}(\omega)]\mathrm{Im}[f(\omega)] - \mathrm{Im}[P^{ps}_{FWM}(\omega)]\mathrm{Re}[f(\omega)]\}. \tag{3.13}$$

This results in a correction term involving $\mathrm{Im}[P^{ps}_{FWM}(\omega)]$. Expanding the above equation using Eq. (3.7), and setting $\omega_{pr}\delta\tau = \pi/2$, we can obtain a modified I_{CARS} expression compared to Eq. (3.12):

$$\begin{aligned} I_{CARS} \propto \int E_{pr}(\omega - \Omega)A(\Omega) \qquad & \{\mathrm{Im}[\chi(\Omega)]\cos[(\omega - \Omega)\tau_0 + \theta(\omega)] \\ & -\mathrm{Re}[\chi(\Omega)]\sin[(\omega - \Omega)\tau_0 + \theta(\omega)]\}d\Omega. \end{aligned} \tag{3.14}$$

In the situation where $|\chi_{NR}| \gg |\chi_R|$, the spectral phase $\theta(\omega)$ is small and simulations show that the first term containing $\mathrm{Im}[\chi(\Omega)]$ again provides the Raman lines, and the second term containing $\mathrm{Re}[\chi(\Omega)]$ contributes to a minor background which can be offset by adjusting the actual τ_0 compared to the theoretical value by less than 0.1 fs. When the ratio χ_R/χ_{NR} increases to a considerable amount, the oscillation due to the phase enters the signal, and causes severe lineshape distortion to the retrieved CARS spectrum— turning it into almost a dispersive shape. A possible solution could be using the high-frequency part of the excitation pulse as LO [75], so that the LO

field becomes real. This may be achieved in the current setup by replacing M_3 with a variable density ND filter. Such an LO field is also advantageous in that its intensity can be controlled to obtain an optimal LO power level for maximizing the signal-to-noise ratio of the retrieved FAST CARS signal [36].

The simulated curves in Figs. 3.7(c) and 3.7(d) were obtained with the following parameters: $\Omega_1 = 300$ cm^{-1}, $\Omega_2 = 650$ cm^{-1}, $\Omega_3 = 1000$ cm^{-1}, with $\Gamma_1 = 15$ cm^{-1}, $\Gamma_2 = 10$ cm^{-1}, and $\Gamma_3 = 20$ cm^{-1}. The probe pulse width was $\delta\omega = 30.5$ cm^{-1}, and the delay parameters $\tau_0 = 0.06$ fs and $\delta\tau = 0.65$ fs.

4. SUPERCONTINUUM GENERATION IN LARGE MODE AREA PHOTONIC CRYSTAL FIBERS AND APPLICATIONS IN COHERENT ANTI-STOKES RAMAN SPECTROSCOPY*

In the previous chapters we have demonstrated single-beam CARS based on a femtosecond oscillator. Despite its simplicity in setup, the detection range is limited below 1000 cm^{-1} due to the finite bandwidth of the oscillator used. To extend the spectral coverage, one needs to adopt excitation sources with broader bandwidth. As a robust and easy-to-achieve method, SC generation in PCFs has been widely adopted in various nonlinear microscopic applications to extend the wavelength coverage. In this chapter we will review the basics in SC generation, and focus on those implementing LMA PCF. Detailed theoretical and experimental investigation of the SC generation process in LMA PCF pumped by a high-energy, high-repetition rate picosecond Nd:YVO_4 laser will be carried out [104]. We analyze the influence of the fiber structure and length on the supercontinuum power, spectral shape, and group delay dispersion, and identify the experimental conditions for stable supercontinuum generation. As a result, we demonstrate SC generation with microjoule-level pulse energy, and with spectrum extending beyond 1600 nm— which allows excitation of Raman modes up to 3000 cm^{-1} and beyond. Finally, we show reliable and efficient operation of a coherent anti-Stokes Raman microspectroscopy setup using this supercontinuum source, followed by the construction of a CARS microscope based on it.

4.1 Supercontinuum generation introduction

Shortly after the invention of the laser technology, various nonlinear effects were studied, which formed the basis of wavelength extension in bulk media. This included optical Kerr effect [105], self-focusing [106], four-wave mixing [107], and stimulated Raman scattering [108]. In 1970, Alfano and Shapiro demonstrated the first significant spectral broadening in borosilicate

*Part of this chapter is reprinted with permission from "Picosecond supercontinuum generation in large mode area photonic crystal fibers for coherent anti-Stokes Raman scattering microspectroscopy" by Y. Shen, A. A. Voronin, A. M. Zheltikov, S. P. O'Connor, V. V. Yakovlev, A. V. Sokolov, and M. O. Scully, 2018. *Scientific Reports*, 8, 9526, Copyright[2018] by Creative Commons Attribution 4.0 International License.

glass pumped by high power picosecond pulses [109]. This was followed by numerous experiments, mostly pumping solid glass or liquid-filled jet with amplified dye laser systems [110]. The advent of high quality single-mode fiber around the 1970s provided yet another platform for SC generation, with much lower power threshold due to the improvement in interaction length. Theoretical and experimental investigation into the fiber-based supercontinuum generation had been conducted, and had covered important topics such as optical solitons and modulation instability [111, 112]. Relative applications such as wavelength division multiplexing and optical coherence tomography had also pushed the technology forward.

By the end of the century, another revolution hit the field, with the introduction of the PCF. Conventional ultrafast pump sources such as Ti:Sapphire, Nd- or Yb- based lasers all emit below the zero dispersion wavelength (ZDW) of silica glass, therefore hard to reach the anomalous dispersion region in glass fibers. With PCF, however, such dispersion can be engineered by controlling the surrounding structure, allowing the ZDW be tuned below the pump wavelength. This, in turn, led to efficient SC generation via solitonic effects [113, 114]. Various SC generation schemes have been demonstrated in the past decades [115], with ever increasing power [116] and blue-shifting of the cut-off edge [117]. Studies have also been carried out using other type of glass for SC generation [118], or using liquid- [119] or gas-filled hollow core PCF [120]. And these SC generation schemes have found wide applications in diverse fields such as optical communication, metrology, and biophotonics [121, 122, 123, 124].

CARS has also benefited from the development of the SC generation [125]. Early experiments focused on multiplex CARS scheme based on the SC source [33, 34, 126, 127]. Later on, SC generation was also incorporated in other CARS schemes, such as single-beam [72] and spectral focusing [128] CARS. To increase the system robustness, all-fiber-source CARS systems were also developed, in which the SC generation served as a key ingredient [129, 130]. SC generation has also been applied in stimulated Raman scattering microscopy [131], and all these improvements have advanced the commercialization and practical application of coherent Raman scattering microspectroscopy [44].

A typical SC-based CARS scheme uses a femtosecond Ti:Sapphire laser to pump a short (several centimeters) small-core PCFs with high nonlinearity [128]. Other excitation sources such as sub-nanosecond microchip laser [34] or Er-doped fiber laser [132] have also been implemented. On the other hand, LMA PCFs, which possess low nonlinearity and are commonly used for light delivery [133, 134], have also been found applicable in SC generation. It should be noted that power scaling of SC generation is not straightforward: for a given pulse duration, pump power is narrowly constrained by the fiber used, and in order to, for example, scale up the generated SC power, the whole experiment, including the fiber, needs to be redesigned. Early research had analyzed SC spectra obtained from different LMA PCFs pumped by a nanosecond laser [135], but with relatively low pump power ($\sim$100 mW) and long fiber length (100 m). Others had used amplified femtosecond laser to excite short-length LMA PCF [136, 137]. While achieving μJ level pulse energy with octave spanning spectrum, the resulting average power only reached mW level. A pump source with picosecond pulse output was also implemented, in an experiment focused on LMA PCF with large air-filling ratio [138]. For more common, commercially available LMA PCF, one expects to achieve μJ level pulse energy, and simultaneously reaching Watt-level output power, by using an appropriate repetition rate of the pump source [139]. Yet more careful characterization of such SC is required, and systematic study of its dependence on various fiber parameters is needed.

In terms of CARS application, there have been a few demonstrations using SC generation in LMA fibers [139, 140], and our present work builds upon these proof-of-principle experiments. The LMA-PCF-based SC source offers several advantages: the large core-size can sustain significantly more power as compared to the small-core, highly nonlinear PCF, offering bright SC output with both high pulse energy and high average power; the intrinsic low N.A. of the fiber allows easy free-space coupling, and the LMA fibers are easier to process in terms of splicing and connectorization, allowing implementation towards all-fiber setups; when pumped with a picosecond laser slightly above 1000 nm, as we will show in this chapter, the generated SC spectrum is predominantly red-shifted, and shows good flatness and smoothness in the infrared region— which forms

an ideal combination for multiplex CARS, providing good spectral resolution, broad coverage of Raman bands, and minimal damage to cells and tissue [141]. Such a source is very promising for potential CARS applications in microscopy [142], cell cytometry [139], as well as in combustion diagnostics [42].

In the next section we investigate the SC generation in several commercially available LMA PCFs. We show that high power SC can be efficiently generated with spectrum extending beyond 3000 cm^{-1} from the excitation wavelength. Spectral and temporal behavior of the SC from different fibers are characterized in details, and we evaluate how different fiber parameters affect the SC generation process. Computer simulations are carried out to provide insights into the processes underlying the SC generation. As a final result, we demonstrate CARS spectroscopy and microscopy utilizing this novel SC source, and show improved spectral coverage compared to previous works [139, 140].

4.2 Supercontinuum generation in large-mode area photonic crystal fibers

4.2.1 Theoretical investigation

To understand the mechanisms of the SC generation process in LMA PCF, we first performed theoretical simulations in a 10-m-long LMA-20 fiber, and visualize the SC development with increasing excitation powers. Our numerical analysis was based on the generalized nonlinear Schrödinger equation [121, 51, 143] for the field envelope:

$$\frac{\partial}{\partial z}A(\omega,z)=i\widetilde{D}(\omega)A(\omega,z)-\frac{\alpha(\omega)}{2}A(\omega,z)+\widetilde{F}\left\{i\frac{\omega_0 n_2\widetilde{T}}{c}\left[\int_{-\infty}^{\infty}R(\eta-\eta')I(\eta',z)d\eta'\right]A(\eta,z)\right\}. \qquad (4.1)$$

Here, $A(t,z)$ is the field envelope, $A(\omega,z)$ is its Fourier transform, z is the coordinate along the propagation axis, t is the retarded time, $\omega=2\pi c/\lambda$ is the radiation frequency, λ is the wavelength, $\widetilde{F}$ is the Fourier transform operator, $\widetilde{D}=\beta(\omega)-\beta(\omega_0)-\partial\beta/\partial\omega|_{\omega_0}(\omega-\omega_0)$, ω_0 is the central frequency, $\beta(\omega)$ is the propagation constant, $\alpha(\omega)$ is the attenuation coefficient, $\widetilde{T}=1+i\omega_0^{-1}\partial/\partial t$, n_2 is the nonlinear refractive index, $R(t)=(1-f_R)\delta(t)+f_R h(t)$ is the optical response function,

which includes the instantaneous (Kerr-type) and retarded (Raman-type) parts, $\delta(t)$ is the delta function, f_R is the fraction of Raman nonlinearity in the nonlinear response, and $h(t)$ is the Raman response function. The Raman response function was approximated in our model with a standard damped-oscillator model [121], $h(t)=(\tau_1^2+\tau_2^2)\tau_1^{-1}\tau_2^{-2}\exp(-t/\tau_2)\sin(t/\tau_1)$. Simulations were performed for typical parameters of fused silica [121, 51]: $n_2=3.2\times10^{-16}$ cm^2/W, $f_R=0.18$, $\tau_1=12.5$ fs, and $\tau_2=34$ fs. The fiber dispersion profile was defined in such a way as to mimic the dispersion of the LMA-20 fiber with the group-velocity dispersion (GVD) passing through the zero at the wavelength $\lambda_z\approx1.23$ μm [144].

The nature of the physical problem, which deals with broadband SC field waveforms generated by narrowband, picosecond input laser pulses, propagating over large fiber lengths, dictates a high computation complexity of simulations [145]. For an adequate description of the SC generation process in our experiments, simulations have been performed on a computational grid consisting of 2^{17} nodes with a 0.5-fs step in the time variable and 2×10^5 nodes with a 50-μm step along the z-coordinate. When performed on such a computation grid, simulations provided an accurate description of the SC output of the PCF we measured.

Figure 4.1 displays the simulation results for the 10-m-long LMA fibers, revealing important tendencies in SC generation and providing important insights into the physics behind spectral and temporal transformations of picosecond laser pulses in LMA PCFs. As is clearly seen in Figs. 4.1a and 4.1b, the initial stage of the SC generation is dominated by stimulated Raman scattering, in good agreement with prior experimental data [146]. Intense Raman sidebands are readily visible in the PCF output for input laser energies in the range of 70 nJ (Fig. 4.1a). As the input laser energy is increased to about 100 nJ, higher-order Raman sidebands start to show up in the fiber output. At even higher input laser energies, these Raman sidebands seed a parametric FWM decay of the pump into Stokes and anti-Stokes FWM sidebands. This parametric conversion is especially efficient near the ZDW where FWM processes of this type are automatically phase-matched [147]. The long-wavelength part of the SC field that falls in the range of the anomalous GVD gives rise to multiple optical solitons, which undergo a continuous self-frequency shift, due to the Raman

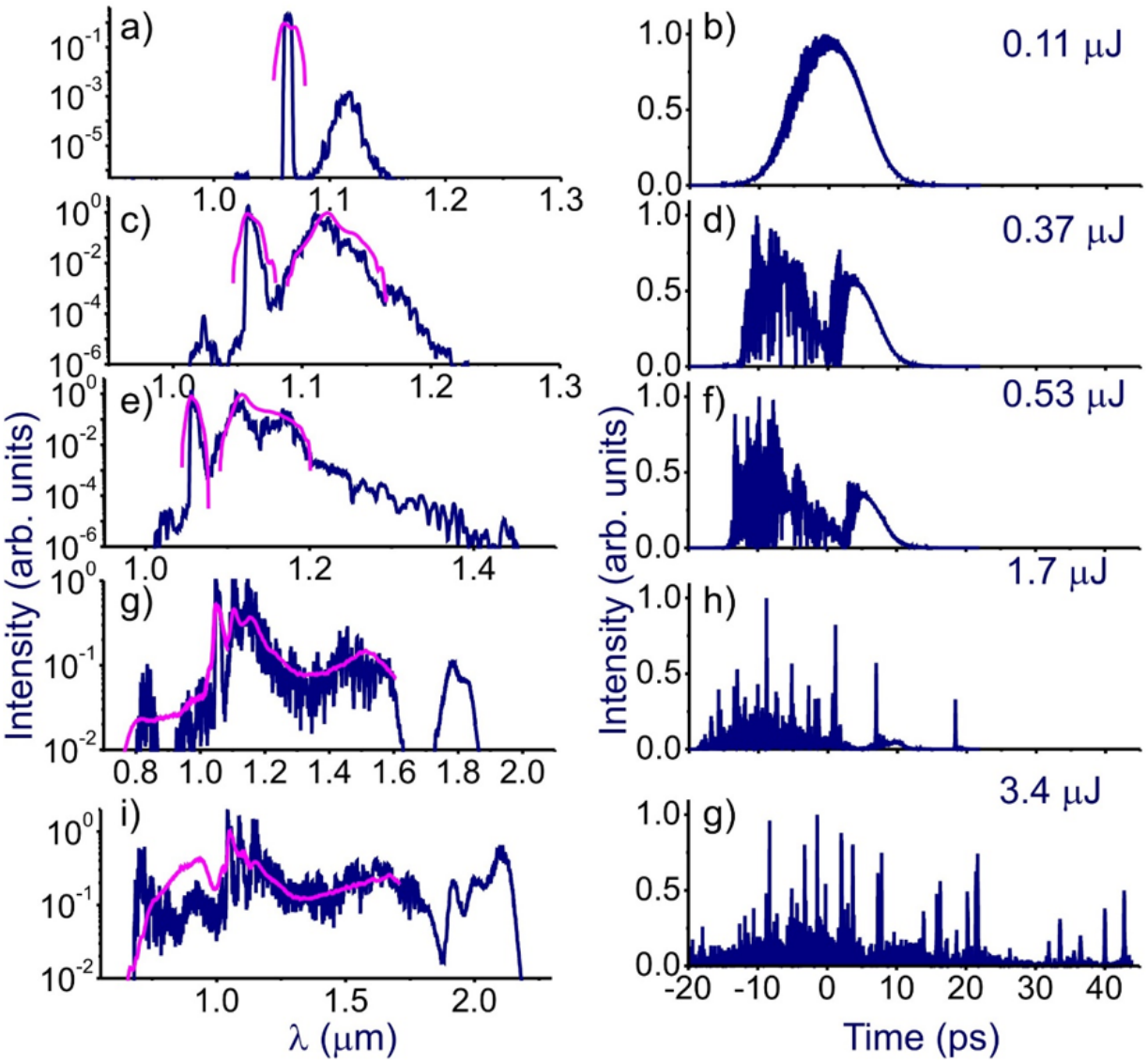

Figure 4.1: The supercontinuum (SC) output of the 10-meter large-mode area (LMA) photonic crystal fiber (PCF): (pink line) experiments and (blue line) simulations. The energy of the SC output is 0.067 μJ (a, b), 0.17 μJ (c, d), 0.31 μJ (e, f), 0.63 μJ (g, h), and 1.27 μJ (i, j). The fiber dispersion profile is shown by the dash-dotted line in (i).

effect, as the pulse propagates along the fiber. These Raman-shifted solitons are clearly visible as intense peaks in the temporal envelope of the SC output in Fig. 4.1.

A clearer picture of the soliton development process is demonstrated through spectrograms shown in Fig. 4.2. Well-isolated features corresponding to the solitons are visible at the output when the SC energy reaches 0.41 μJ in Fig. 4.2d, and increases in number as the pulse energy gets stronger. Meanwhile, dispersive waves originate from these solitons also appear as isolated packets on the anti-Stokes side of the excitation wavelength, and their correlation can be directly drawn from the spectrograms. In addition, the effect of chromatic dispersion due to fibers are better visualized in Fig. 4.2 as a parabolic variation of spectral components over wavelength.

4.2.2 Experimental results

LMA PCFs tested here included LMA-15, LMA-20, LMA-25, and LMA-PM-15 (NKT Photonics), all of which showing similar dispersion curves with ZDW close to 1230 nm [144]. The first three fibers are normal LMA PCF, with core sizes 15 μm, 20 μm and 25 μm, respectively; the last one is a polarization-maintaining LMA PCF with a core size of 15 μm. Their cross-sections after cleaving are shown in Fig. 13, and their parameters are listed in Table 4.1 [144]. The power of the SC output was measured by a thermopile power meter (PM10, Coherent), and the spectra were acquired by a combination of a visible (BlueWave, Stellarnet) and a near infrared (EPP2000, Stellarnet) spectrometer modules, both corrected for the spectral response. When testing the LMA-PM-15, we also added a half-wave plate in front of the in-coupling lens before the PCF to control the polarization of the incident light.

Fiber	Core size (μm)	λ_z (nm)	Bend edge (nm)	N.A.
LMA-15	15.1	1222	500	0.07
LMA-20	19.9	1226	700	0.06
LMA-25	25.0	1235	900	0.05
LMA-PM-15	14.8	1221	500	0.07

Table 4.1: LMA PCF parameters. λ_z represents the zero dispersion wavelength (ZDW) of the fiber.

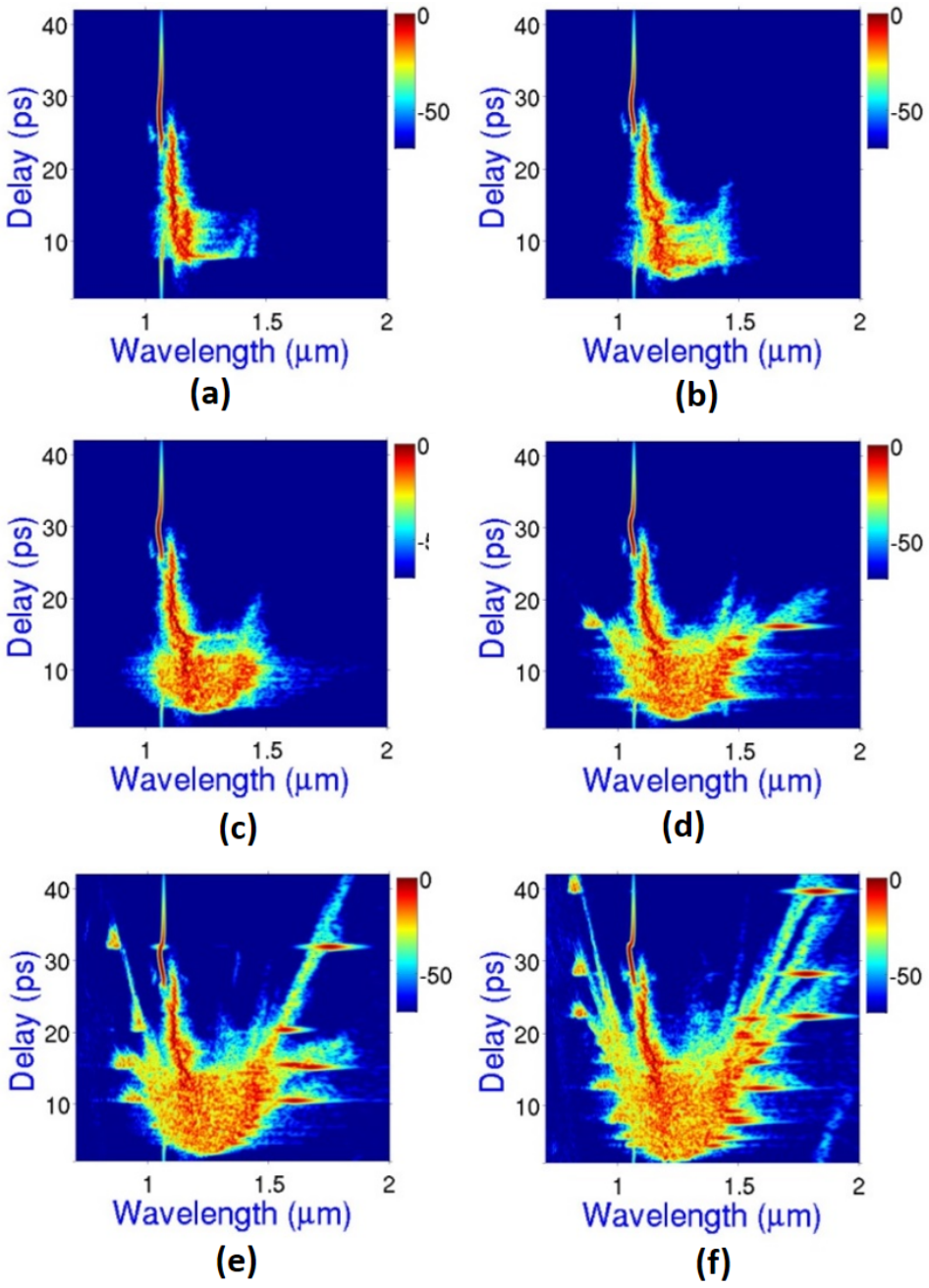

Figure 4.2: Spectrograms of the SC output of the 10-m-long LMA PCF. The energies of the SC output are 0.24 μJ (a), 0.35 μJ (b), 0.41 μJ (c), 0.45 μJ (d), 0.56 μJ (e), and 0.63 μJ (f).

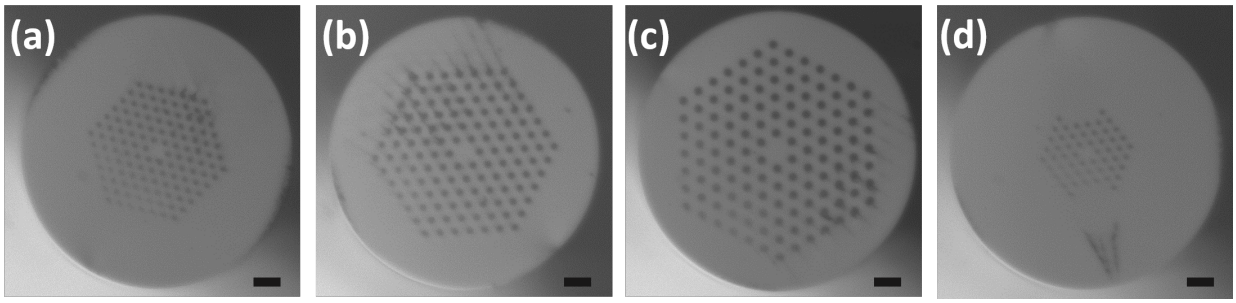

Figure 4.3: Cross-sections of the LMA PCF: (a) LMA-15, (b) LMA-20, (c) LMA-25, and (d) LMA-PM-15. The scale bars in all figures indicate 20 μm.

First, as a verification to our theoretical model, we have collected SC spectra from a 10-m-long LMA-20 PCF with the corresponding pulse energy, and the results are plotted together with the theoretical simulation curves in Fig. 4.1. In general, the experimental spectra fall in good agreement with the simulation predictions in spectral shape and major sideband positions. Minor deviations in the peak structures could be the result of calibration errors, finite resolution, and limited dynamic range of the spectrometer module. Bending and tension in the fiber also contributes to the disagreement between the theoretical and the experimental data, as their effects are hard to quantify numerically for the simulation.

Given the fact that the LMA fibers studied here share similar dispersion profile and same core material, it is expected that the LMA-15 and LMA-25 PCF follow similar SC generation process as demonstrated above. However, the difference in core size and bent edge can lead to significant differences in the SC pulse energies and spectra, especially on the short-wavelength side of the pump wavelength. We examined such differences by comparing the SC spectra generated from 5-m-long LMA-15, LMA-20, and LMA-25 fibers, as shown in Fig. 4.4. Figure 4.4a indicates that, under a relatively low pump power (1.36 W), SC spectrum in fibers with smaller core gained broader extension in wavelength compared to that with a larger core under the same excitation power. This is reasonable due to their smaller effective areas, which led to higher nonlinear coefficient and therefore enhanced wavelength extension. Under a higher pump power of 3.8 W, the SC spectra from the three fibers are shown in Fig. 4.4b. Despite the similar broadening on

the long-wavelength side, the SC spectra exhibited vast difference in the visible range, with the LMA-15 spectrum extended into the blue light region, the LMA-20 spectrum ended close to 600 nm, and the LMA-25 spectrum edge further red-shifted to 700 nm. We note that, while 3.8 W of pump power was close to the damage threshold of the LMA-15 fiber, for LMA-20 and LMA-25 the pump power could be safely increased up to 5 W and 8 W, respectively. But the corresponding SC pulse energy only rose to 1.6 W and 1.9 W, respectively; and the spectra obtained from these fibers under higher pump power showed insignificant changes in their visible-range performance. The major reason leading to such differences between fibers can be the excessive loss of light close to the bend edge of the fiber. Other factors such as changes in nonlinearity and ZDW can also affect the short-wavelength-side performance of the SC [135].

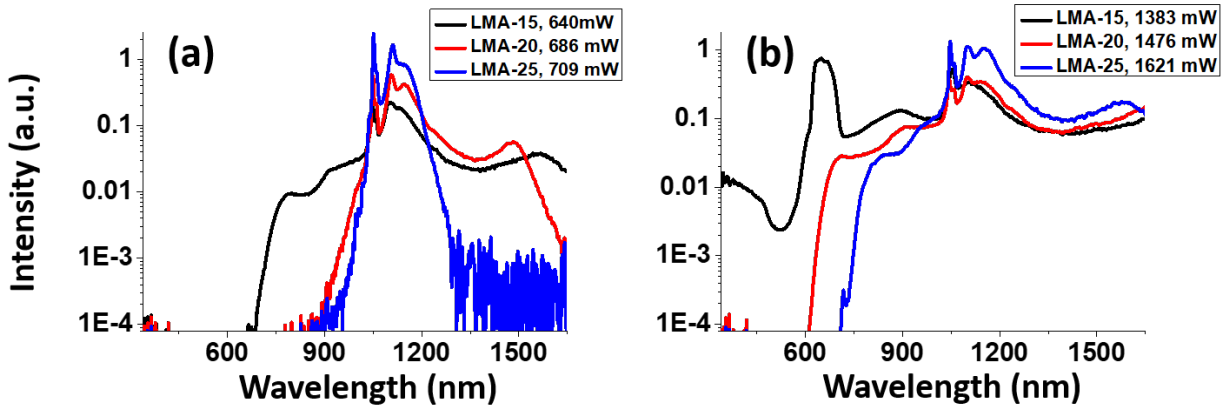

Figure 4.4: SC spectra generated from 5-m-long LMA-15, LMA-20, and LMA-25 fibers, under a pump power of (a) 1.36 W and (b) 3.8 W. Legends show the corresponding length and the SC power for each curve.

Another factor influencing the output SC pulse is the fiber length. We expect longer fibers to have a lower onset power level for the spectral broadening to occur beyond their ZDW, because the soliton fission length is inversely proportional to the square root of the peak intensity [51]. This is indeed the case, as we can see in Fig. 4.5a where three SC spectra obtained from the LMA-20 PCF with 2-meter, 5-meter, and 10-meter fiber length are plotted, all pumped at 1.36 W. While for

the 2-m-long LMA-20, the SC spectrum extended only up to 1200 nm, those from 5-m-long and 10-m-long PCFs had exceeded 1600 nm, and the SC generated in the 10-m-long fiber also showed significant extension on the short-wavelength side of the pump, corresponding to the simulation shown in Fig. 4.1g and Fig. 4.2f. The SC spectra under higher pump power (5.8 W) are plotted in Fig. 4.5b. Overall, we see that longer fibers offered better flatness and smoothness in their SC spectra from the visible to the short-wave IR region. For the 2-m-long LMA-20 fiber, the variation in spectral intensity exceeded 15 dB in the range from 1000 nm to 1600 nm, while that for 5-m-long and 10-m-long fibers were 7.7 dB and 6.5 dB, respectively. On the other hand, SC pulse energy saw significant decrease as the fiber length increase, which again could be attributed to the loss due to bending and tunneling modes.

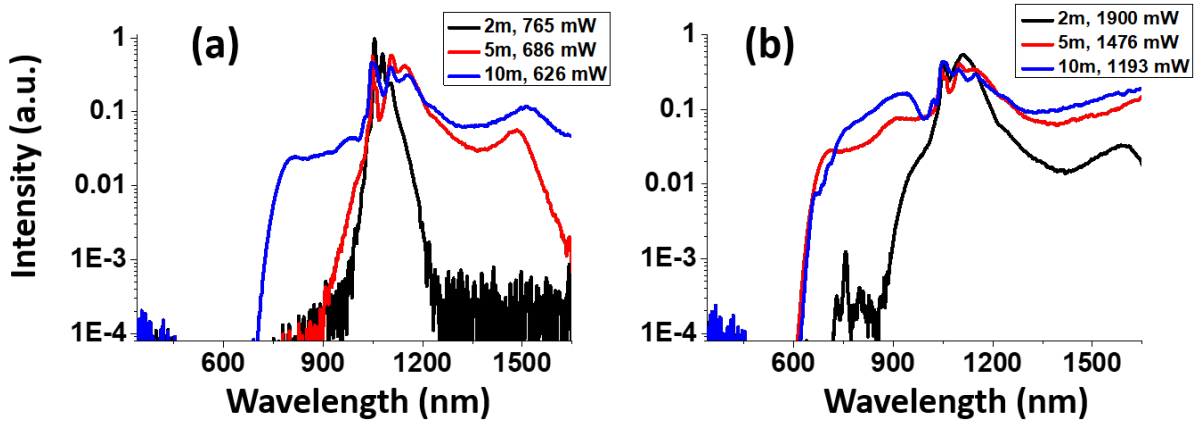

Figure 4.5: SC spectra generated from LMA-20 fiber with 2-meter, 5-meter, and 10-meter length, under a pump power of (a) 1.36 W and (b) 5.8 W. Legends show the length and output SC power of the corresponding curves.

When varying fiber length, chromatic dispersion also plays an important role in SC characteristics, as we have already seen in the simulation result. To visualize and quantify the effect of fiber dispersion, we have constructed a CARS setup, and used the anti-Stokes nonresonant signal from a microscope slide (Micro Slides, VWR) to infer the temporal behavior of the generated SC. Details of the setup will be provided in the next section. We measured a sequence of spectra at

varying pump and Stokes delay times, and Fig. 4.6 shows three such spectrograms recorded for the SC generated in 2-m-, 5-m-, and 10-m-long LMA20 fibers. We notice the group delay dispersion and pulse-broadening effects become significant in the case of a longer fiber. For the 10-m-long LMA-20 fiber, the leading edge of the anti-Stokes signal pulse was around 935 nm, corresponding to $\sim$ 1230 nm in the SC pulse, which is the ZDW of the fiber; and on either side of ZDW the pulse was stretched in time up to 25 $\sim$ 30 ps. The spectrogram for the 2-m-long LMA-20 fiber, on the other hand, shows little broadening due to dispersion. The measured spectrogram in Fig. 4.6c exhibits similar chromatic dispersion property as that in Fig. 4.2f, yet the fine details of the temporal behavior, such as those related to soliton mechanism, are not visible. This is because the pump pulse extended up to 7 ps in time, therefore the spectrogram lacked temporal resolution, and the peak information from various solitons were smoothed out due to the convolution with the pump pulse. Either probing with a synchronized femtosecond laser or examining the SC pulse through optical time-stretch [148] can be a solution to visualize the soliton behavior shown in Fig. 4.2f.

To evaluate the effect of bending loss associated with these fibers, we first take another look at how the SC develops with increasing pump power. Figure 4.7a shows a set of SC spectra collected for a 2-m-long LMA-20 fiber under increasing excitation power, and the results followed a similar trend as that shown in the simulation in Fig. 4.1. We also plot the relationship between the pump power and the output SC power in Fig. 4.7b. When the pump power was low, an increase in the pump power led to a linear growth in the SC power, and the throughput remained above 50%; when the excitation power exceeded 4W, the growth rate of the SC power decreased sharply, and the SC power saw a saturation around 2W. The turning point coincided with that when the SC started to develop its visible portion. It is reasonable to believe that the saturation was mainly due to the visible SC light escaping the fiber via higher-order modes or tunneling modes. Therefore, the excessive power used to generate this visible portion is lost during transmission, and the SC sees saturation in power.

For a direct comparison, we recorded the SC spectra from the 2-m-long LMA-25 fiber in bent and straight status. When bent in spool, the bending radius of the fiber was around 12.5 cm. The SC

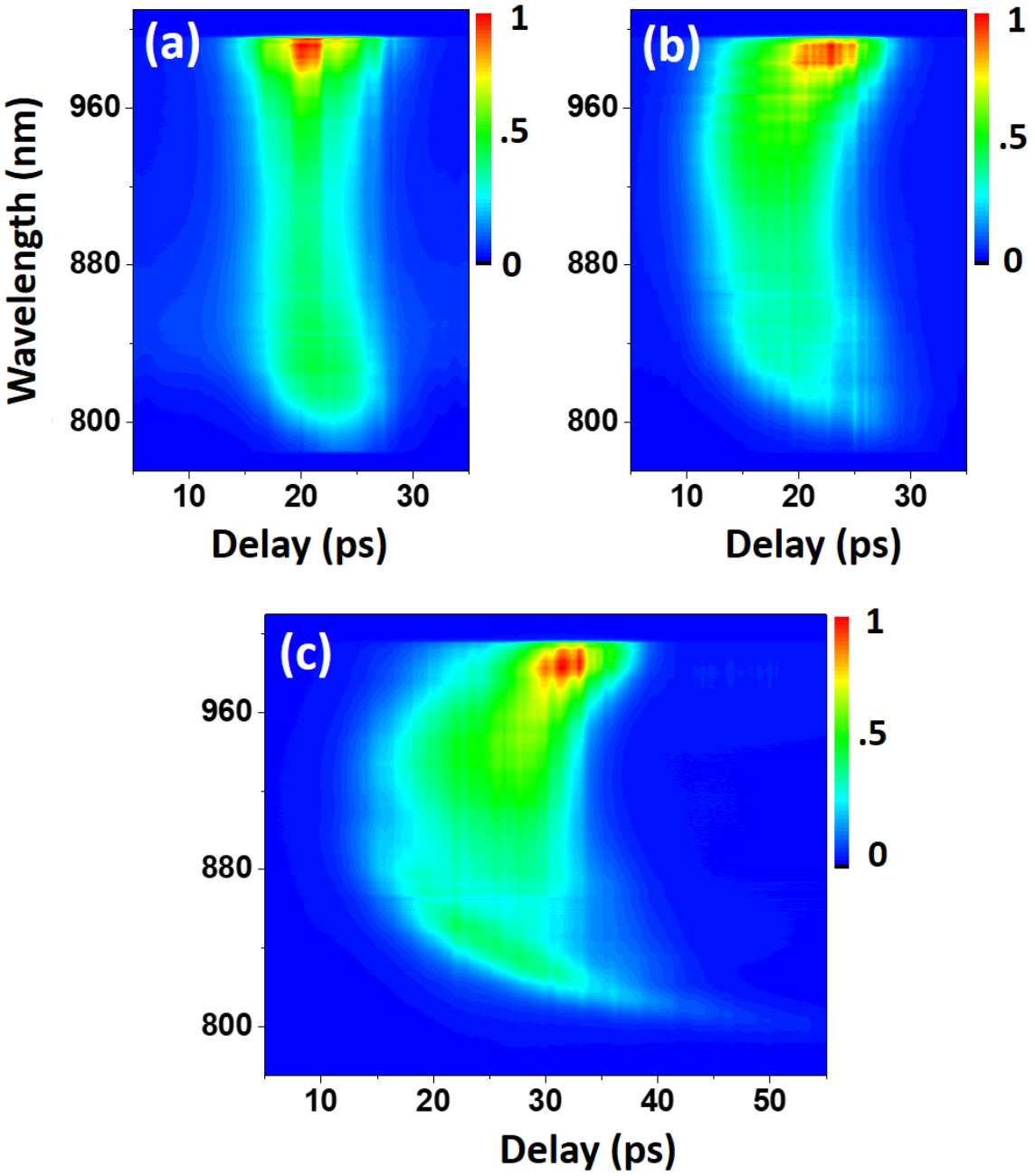

Figure 4.6: Spectrograms of the nonresonant anti-Stokes signal from a microscope slide. SC Stokes pulse are generated from LMA-20 fibers with a length of (a) 2m, (b) 5m, and (c) 10m.

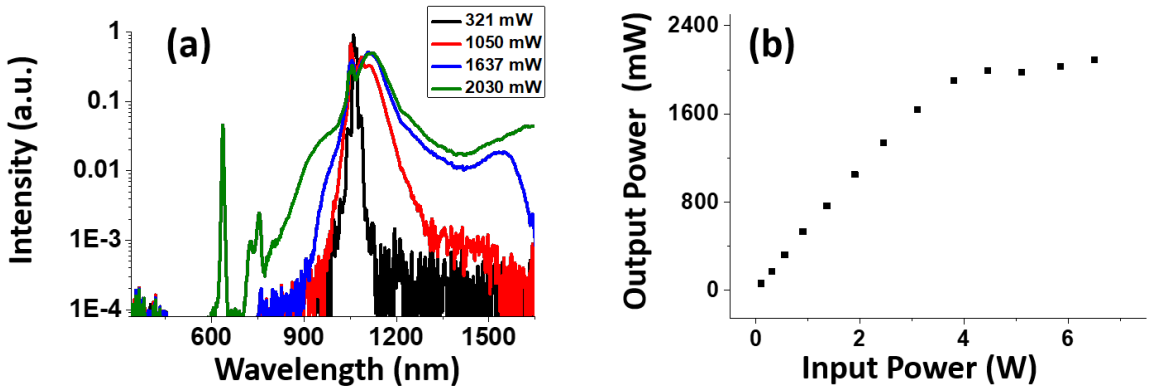

Figure 4.7: (a) SC spectra generated from a 2-m-long LMA-20 fiber. Legends show the output SC power of each curve. (b) The dependence of the SC output power as a function of the input power.

spectra from bent and straight fibers are plotted in Figs. 4.8a and 4.8b, respectively. As expected, the SC produced by the straight fiber displayed a major difference as compared to the bent one in its visible range performance, with the visible cut-off edge shifted from 700 nm to 600 nm; and the SC power increased from 2.2 W to 3.2 W under the same pump power of 8.3 W. This can be attributed to the reduced bending loss in the straight fiber, which preserved more power in the SC generation and transmission. Also, we noticed that for the straight fiber spectrum, a peak signal around 800 nm appeared when the SC power increased to 1.8 W. This could be due to the coupling between the pump and the SC Stokes, producing anti-Stokes SC signal, as we can observe a minor dip structure occurring around 1590 nm in Fig. 4.8b.

Finally, we note that all the SC generated in previous fibers are un-polarized. In order to obtain efficient SC source for polarization-sensitive application, we tested the SC generation in a polarization-maintaining LMA PCF. The SC spectra from LMA-PM-15 fiber are shown in Fig. 4.9, with the excitation polarization along the fast- and slow-axis of the fiber plotted in Figs. 4.9a and 4.9b, respectively. For the SC excited along the slow-axis, two spectral peaks emerged when SC power reached 710 mW, one around 890 nm and the other around 1320 nm. By placing a polarizer at the SC output, we found that these spectral components had a polarization along the fast axis. This can be attributed to the FWM process, in which the pump beam seeded spectral

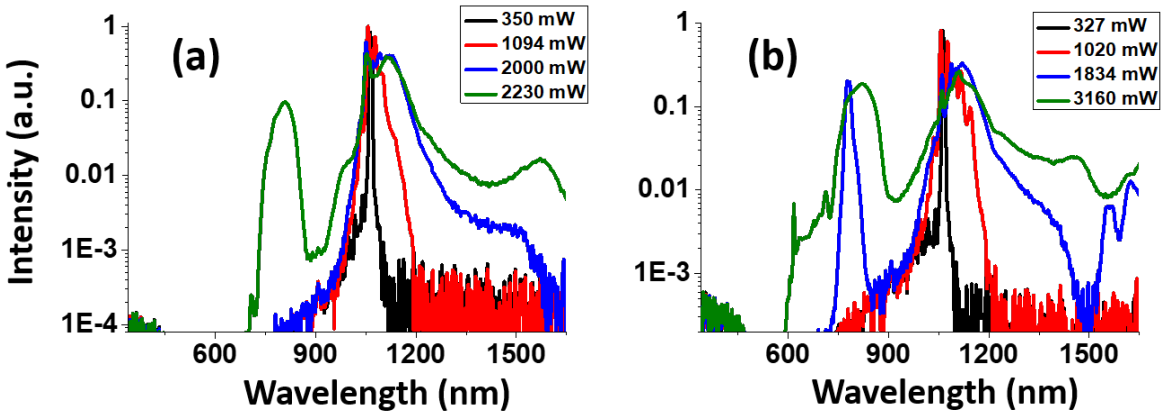

Figure 4.8: SC spectra generated from 2-m-long LMA-25 fiber in (a) bent and (b) straight status. Legends show the output SC power of each curve. The curves in the two plots with the same color shares the same excitation power.

components in the fast axis mode that appeared symmetrically on both sides of the excitation wavelength, and satisfying the phase-matching condition [51]. We note that the SC generation shown in Fig. 4.9a has a similar spectrum to that generated in the 2-m-long LMA-15 fiber, with a slightly lower output power of 1.3 W compared to the 1.6 W from the latter. However, given the fact that the output light was linearly polarized, the SC generation in the polarization-maintaining LMA fiber actually contained more useful power as compared to a typical LMA fiber, especially for polarization CARS application. Therefore it is reasonable to expect that a polarization-maintaining version of the LMA-20 and LMA-25 PCF can produce higher power with linearly polarized SC light.

We have shown some typical SC spectra from LMA PCF above. Benefiting from the high brightness SC source, we can implement a high efficiency CARS system, and construct a microscope based on this novel source, as we will describe in the following section.

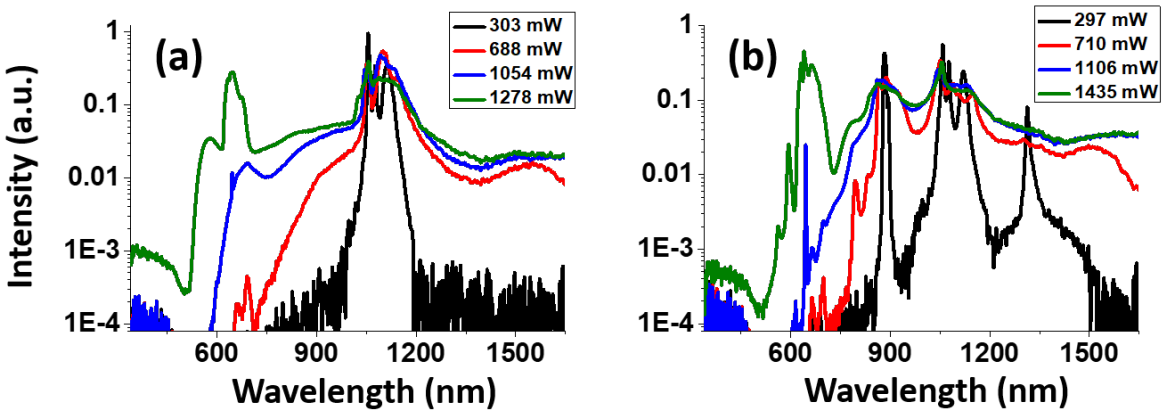

Figure 4.9: SC generation from the 2-m-long LMA-PM-15 fiber, with (a) and (b) showing excitation along the fast- and slow-axis, respectively. Legends show the output SC power of each curve.

4.3 Application to multiplex coherent anti-Stokes Raman scattering microspectroscopy

4.3.1 Setup description

The experimental setup for CARS microspectroscopy is shown in Fig. 5.1. An industrial Nd:YVO_4 laser centered at 1064 nm (APLX-10, Attodyne) was used as the pump source, which output 7 ps pulses at the 1-MHz repetition rate. The output beam was divided into two arms, and the power in each arm was controlled by the combination of a half-wave plate and a polarizer. The output of one arm was launched into the LMA PCF for the SC generation using a plano-convex lens (AC254-100-C-ML, Thorlabs), and was subsequently collimated by an off-axis parabolic mirror (MPD229-M01, Thorlabs); the other arm was sent to a delay stage to ensure a proper temporal overlap of the pulses from the two arms at the sample. Note that the same setup has been applied in the SC characterization mentioned in the previous section.

The SC beam was filtered by a long-pass filter (FELH1150, Thorlabs) before recombining collinearly with the 1064-nm beam through a dichroic beam-splitter (LPD02-1064RU-25, Semrock). The SC was used as the Stokes beam, and the 1064 nm radiation was used as the degenerate pump and probe beam in the CARS experiment. Both beams were aligned to the same polarization

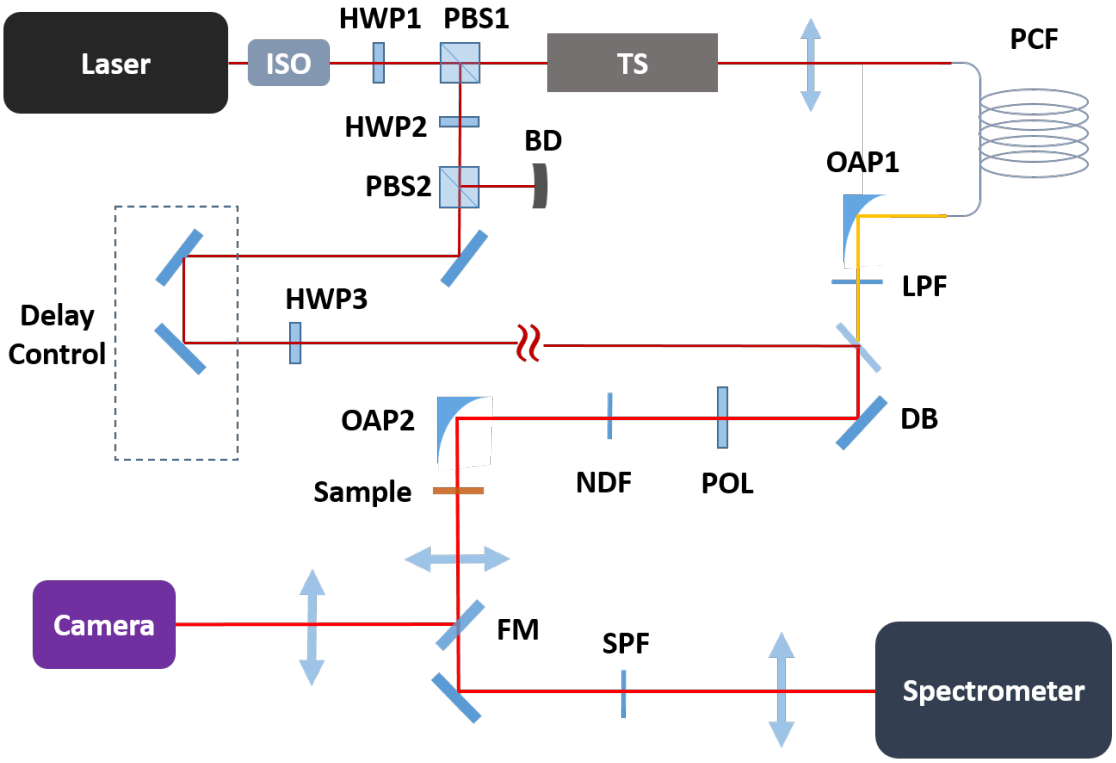

Figure 4.10: Schematic of the picosecond SC CARS system. ISO: isolator; HWP: half-wave plate; PBS: polarizing beam-splitter; BD: beam dump; OAP: off-axis parabolic mirror; LPF: long-pass filter; DB: dichroic beam-splitter; NDF: neutral density filter; FM: flip mirror; SPF: short-pass filter.

by a polarizer (LPNIR100-MP2, Thorlabs) and attenuated to appropriate power before focusing onto the sample. The transmitted light was either directed to a CCD camera by a flip mirror for bright-field imaging, or guided through a short-pass filter and then sent to the spectrometer (Holospec, Andor) with the attached TE-cooled CCD (iDus416, Andor) for detection.

4.3.2 Result analysis

For demonstration of CARS microspectroscopy, we have chosen to use the 2-m-long LMA-20 fiber as the SC source. The short fiber length eliminated the need for large chirp compensation; and the LMA-20 PCF produced more useful Stokes power compared to the LMA-15 fiber, while requiring only moderate excitation power, leaving us plenty of room for power control in the pump beam. As an example, we first show CARS spectroscopy of the ambient air. The power of the pump and Stokes beams were measured to be 89 mW and 139 mW, respectively. We loosely focused the beam into the air using a lens with a focal length of 100mm (we estimated the beam waist to be $\sim$30 μm), and set the integration time to be 50 ms. Figure 4.11 shows a typical CARS spectrum obtained from the ambient air, with the vibrational peaks corresponding to nitrogen and oxygen molecules marked in the graph. The ratio of the nitrogen peak count over the oxygen peak count was around 15, which is reasonably close to the previous result [149], taking into account the quadratic dependence of the CARS signal on the concentration and the variation in spectrometer efficiency.

Next we performed CARS microspectroscopy using a mixed sample of polystyrene (PS) and PMMA beads as the sample. The beads were surrounded by immersion oil (Type B, Cargille Lab), and the whole mixture was sandwiched between two coverslips (Micro Cover Glasses, VWR). Typical CARS spectra of the three species are shown in Fig. 4.12a, and the bright-field image is shown in Fig. 4.12b. We selected three characteristic bands in the C-H stretching region corresponding to each material for imaging. The center Raman shifts were chosen to be 3050 cm^{-1}, 2950 cm^{-1}, 2850 cm^{-1} for PS, PMMA and immersion oil, respectively. The retrieved images from these bands are shown in Figs. 4.12c, 4.12d, and 4.12e, respectively. From these figures we can easily identify the PS and PMMA beads from the background. The power of the pump and Stokes

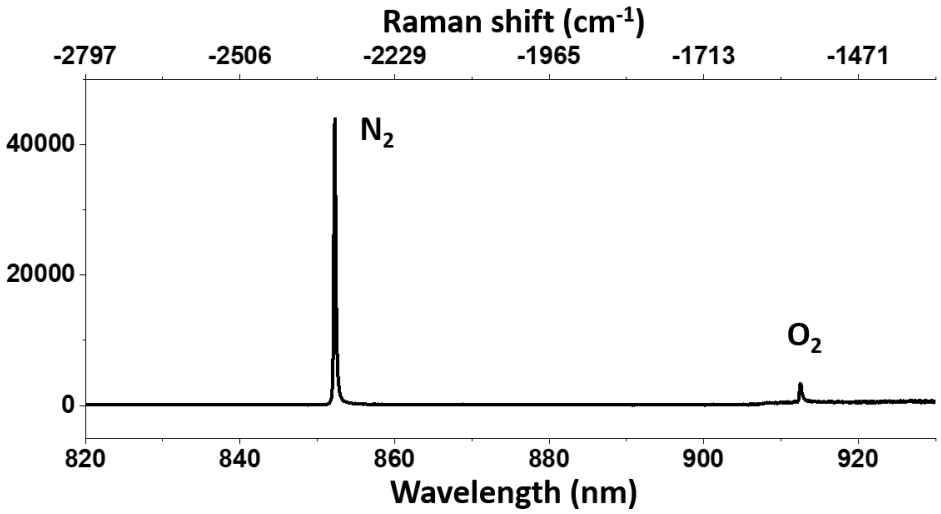

Figure 4.11: CARS signal collected from the ambient air using the picosecond SC setup, exhibiting two peaks corresponding to nitrogen (2331 cm^{-1}) and oxygen (1556 cm^{-1}) vibrational transitions.

beams were 1.9 mW and 1.3 mW, respectively, with a pixel dwell time set to 40 ms. The focusing element was an off-axis parabolic mirror which had a focal length of 15 mm, and signal was collected by an achromatic lens with 30 mm focal length. We estimate the spatial resolution to be 4 μm. We note that the selection of the dwell time was limited by the CCD shutter, which has an open/close time around 10 ms. It is possible to reduce the exposure time by adding an additional fast shutter in the laser path to make the exposure down to 10 ms or less, which is more common for multiplex CARS setup [37, 54]. We also note that there is still much space for improvement on the signal level, due to the low N.A. (0.37) focusing element used here.

We further demonstrated imaging of micron-size diamond flakes with nickel embedded in it [150]. A typical CARS spectrum of the diamond sample and the background signal is exhibited in Fig. 4.13a. The diamond signal at 1332 cm^{-1} is clearly pronounced, and the peak around 885 nm is due to nickel [150]. Again, a bright-field image of the structure captured is shown in Fig. 4.13b, and the three retrieved CARS images corresponding to the background, the nickel, and the diamond are presented in Figs. 4.13c, 4.13d, and 4.13e, respectively. Here the power of the pump and Stokes beams were 5.1 mW and 3.9 mW, respectively, with the pixel dwell time 40 ms. We

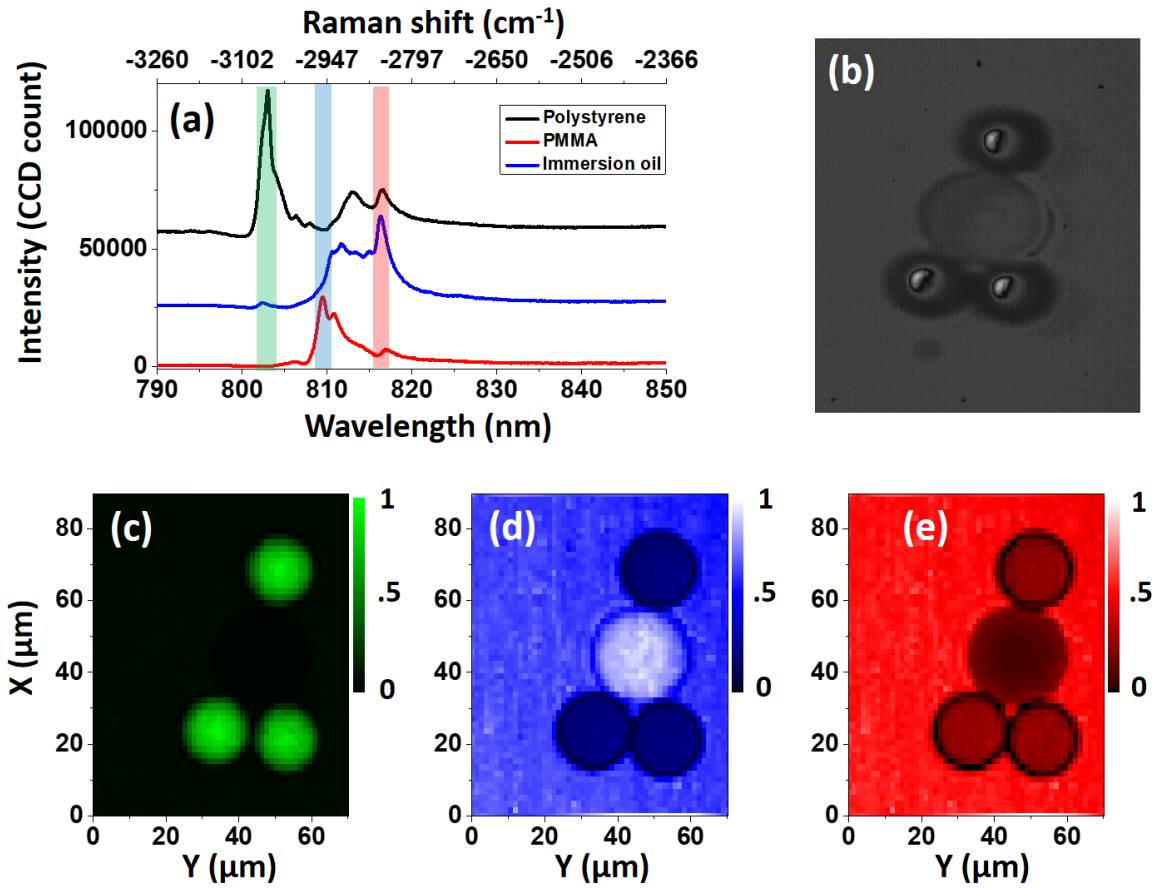

Figure 4.12: (a) CARS spectra from polystyrene (PS), poly(methyl methacrylate) (PMMA), and immersion oil. (b) Bright-field image of the captured bead structure. The retrieved image using the signal in the three bands marked in (a) are shown in (c), (d) and (e), plotted with their corresponding colors.

note that, due to the opacity of these flakes, the epi-detection CARS setup [44] could yield even higher signal level compared to the signal detected in a transmission geometry, as it was used here.

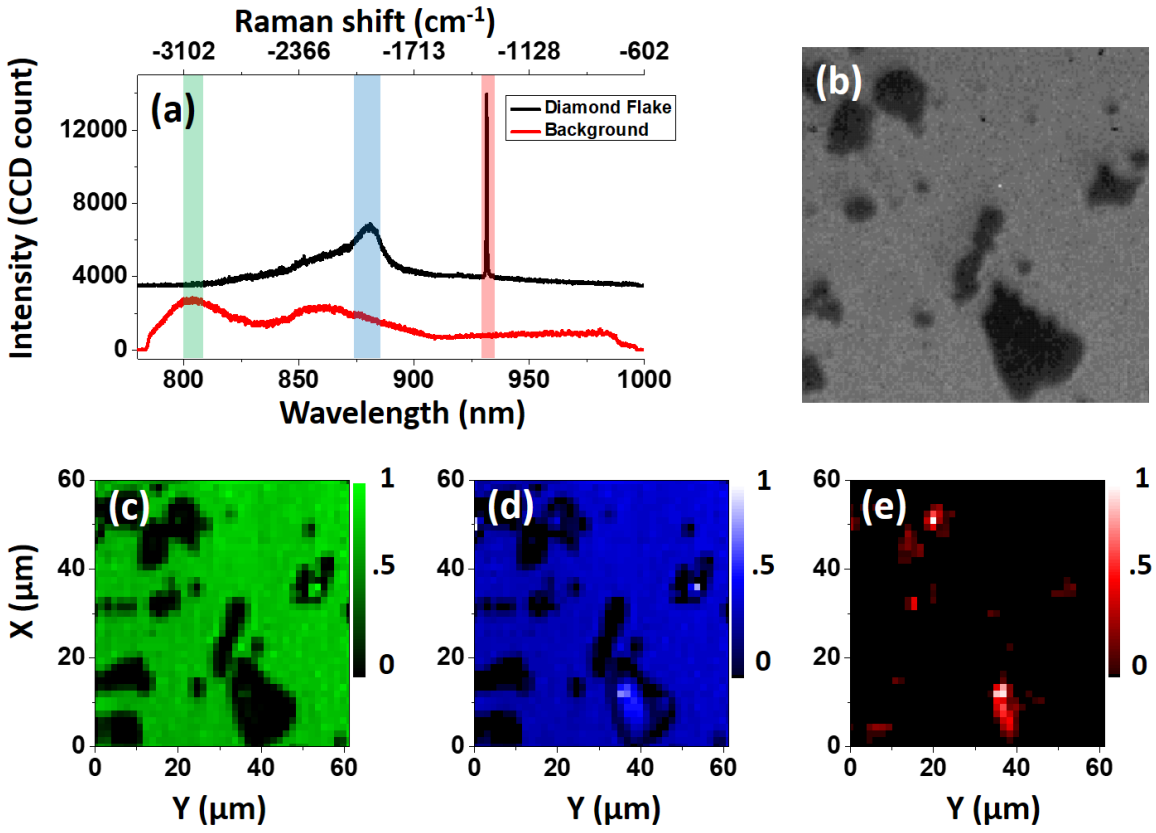

Figure 4.13: (a) CARS spectra from diamond flakes. (b) Bright-field image of the captured flake structure. The retrieved image using the signal in the three bands marked in (a) are shown in (c), (d) and (e), plotted with their corresponding colors.

4.4 Coherent anti-Stokes Raman scattering microscope construction

Following the demonstration in the previous section, we designed and constructed a microscope based on our SC source using the LMA PCF. For the main frame we used a commercial upright microscope (LV-series, Nikon). By fixing the top trinocular and incorporating a slide mirror above the epi-illuminator, easy switching between the bright-field imaging and the laser-scanning CARS imaging is achieved. Currently we use a reflective objective (LMM-40X-P01, Thorlabs)

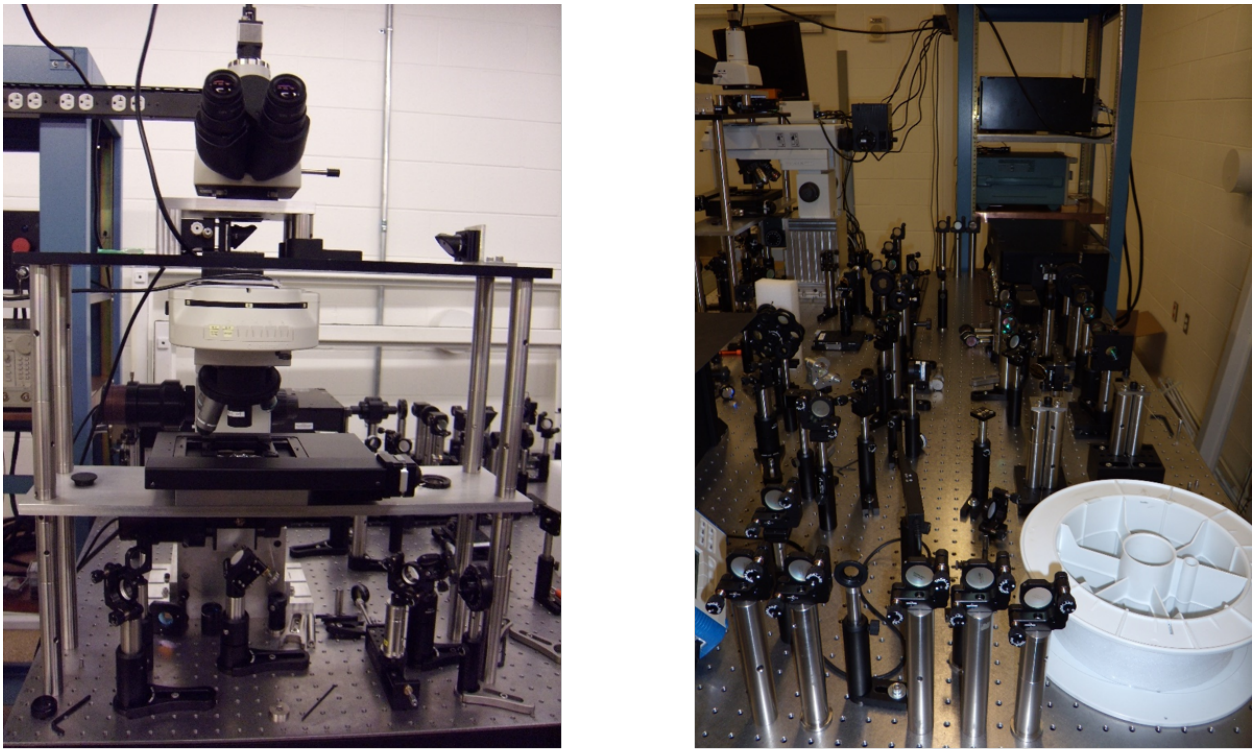

Figure 4.14: CARS microscope using the LMA-PCF-based picosecond SC source. (a) Microscope stand built using Nikon components and custom parts. (b) CARS setup layout.

to focus the incident laser beam, with a throughput $\sim$30%. The transmitted signal is collected by another objective (20X Plan Fluor, Nikon) with the same 0.5 NA. This signal is then sent to the spectrometer after proper filtering. On the other hand, the reflected signal can be collected by the focusing objective and propagates backward. A longpass filter in the beam path (FELH1000, Thorlabs) reflects this signal, and guides it to another slide mirror, which is used to switch between the forward- and the epi-detection mode. When using the epi-detection mode, forward signals are blocked, and the back-scattered light is sent to the spectrometer by the flip mirror.

We use a motorized scanning stage (OptiScan, Prior Scientific) for 2D scanning of sample in XY directions. In addition, we have mounted two z-drives (PS3H122R, Prior Scientific) on the top and bottom focusing block to move the two objectives simultaneously, so as to achieve scanning in the z-direction. This can also be achieved through a z-scanning stage on the sample. The XY-stage has a maximum travel of 100 mm in one direction, and a minimum resolution of $\sim$1 μm. The layout of the microscope and the whole CARS system are shown in Figs. 4.14a and 4.14b, respectively.

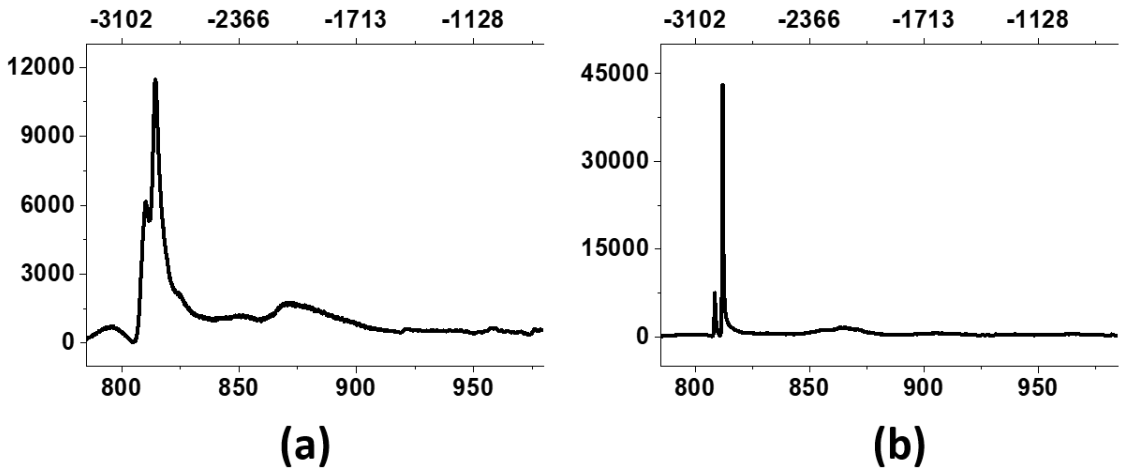

Figure 4.15: Test CARS spectra obtained from (a) glycerol liquid and (b) L-cyctine powder, using forward- and epi-detection, respectively.

We first demonstrate some test spectra acquired from standard samples. Figure 4.15a shows

the CARS spectrum of glycerol (Sigma Aldrich) obtained in the forward detection. The integration time was set to 100 ms, and the laser power on the sample were 5 mW and 4.9 mW for the pump and the Stokes beam, respectively. We can see clearly the signal in the C-H stretching region, but for those in the fingerprint region, the signal level is relatively low. We also demonstrate epi-detection capability by taking the back-scattered CARS spectrum from L-cystine powders (Sigma Aldrich) using the same power and acquisition settings, and the result is given in Fig. 4.15b.

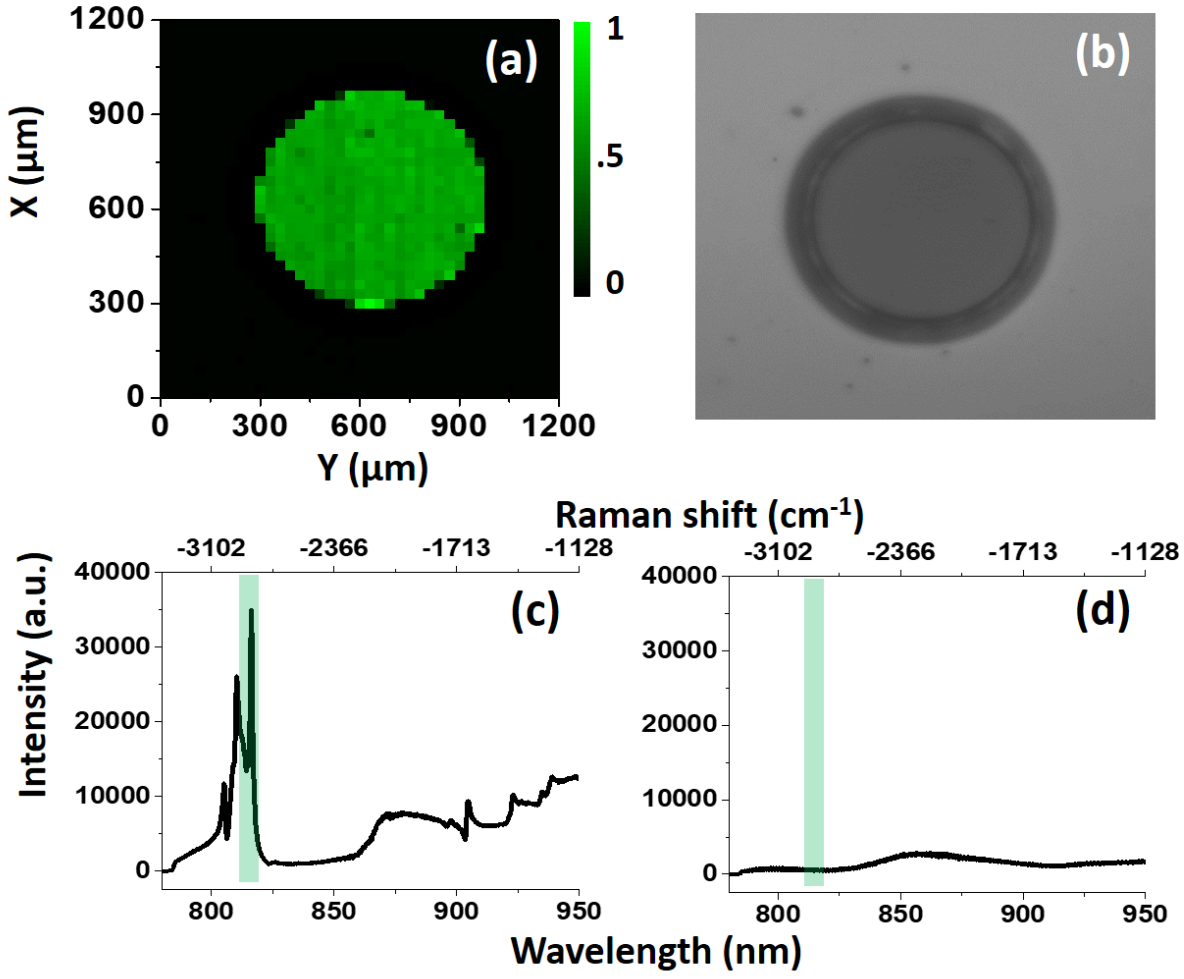

Figure 4.16: CARS microscopy of oil droplet. (a) Retrieved CARS image of the oil droplet using the aliphatic C-H stretching signal. (b) Bright-field image of the droplet. The anti-Stokes spectra of the oil signal and the background are shown in (c) and (d), respectively, with green vertical bar indicating the signal region used for image reconstruction in (a).

Next we demonstrate 2D scanning capability by imaging an oil droplet. Figure 4.16a shows the CARS image of the droplet, and Fig. 4.16b its bright-field image. Integration time was set to 100 ms, and the capture of the whole hyperspectral image took about 10 minutes. Note that the software has not been optimized, and the high signal-to-noise ratio (SNR) could allow less integration time on the order of millisecond, therefore reducing the total image time to less than a minute. In addition, we performed 3D scanning on PMMA microspheres by incorporating z-scanning, and the result is plotted in Fig. 4.17. The 3D image is reconstructed in a point cloud fashion, and each point is color-coded with the signal intensity. Benefiting from the hyperspectral data, we can obtain the signal through the unique spectral feature of PMMA— by taking the subtraction between the peak count at 2920 cm^{-1} and that at 2850 cm^{-1}. In this way, the immersion oil will give a negative signal and can be eliminated in the plot. Also notice that the glass gave a weak background and appeared in Fig. 4.17c at the top and bottom of the bead, and this can also be eliminated by setting a higher signal threshold.

4.5 Discussions

The typical coupling efficiencies for all LMA fibers in a low power regime were around 60%, mostly due to input coupling loss. Higher coupling efficiency (up to 90%) could be achieved through spatially filtering the laser mode. However, this imposes a large waste on the laser power and heating load on the spatial filter. Further improvement can be made using wavefront correction tool on the pump beam.

CCD etaloning effect during spectral acquisition was found to be significant. Because the fingerprint region is between 900 and 1010 nm, etaloning will impose serious fringing problems for back-illuminated CCD, especially when the nonresonant background is prominent. We came up with a simple solution to this challenge by utilizing a single-mode fiber for coupling into the spectrometer. If the fiber's core-size is smaller than the CCD pixel size (about 15 μm), then, by recording the spectrum of a calibrated source, say, a halogen lamp, a correction curve can be measured and the fringe on the spectrum can be suppressed through post-processing. The function of the single-mode fiber is similar to the pinhole in a confocal microscope, thus, offering additional

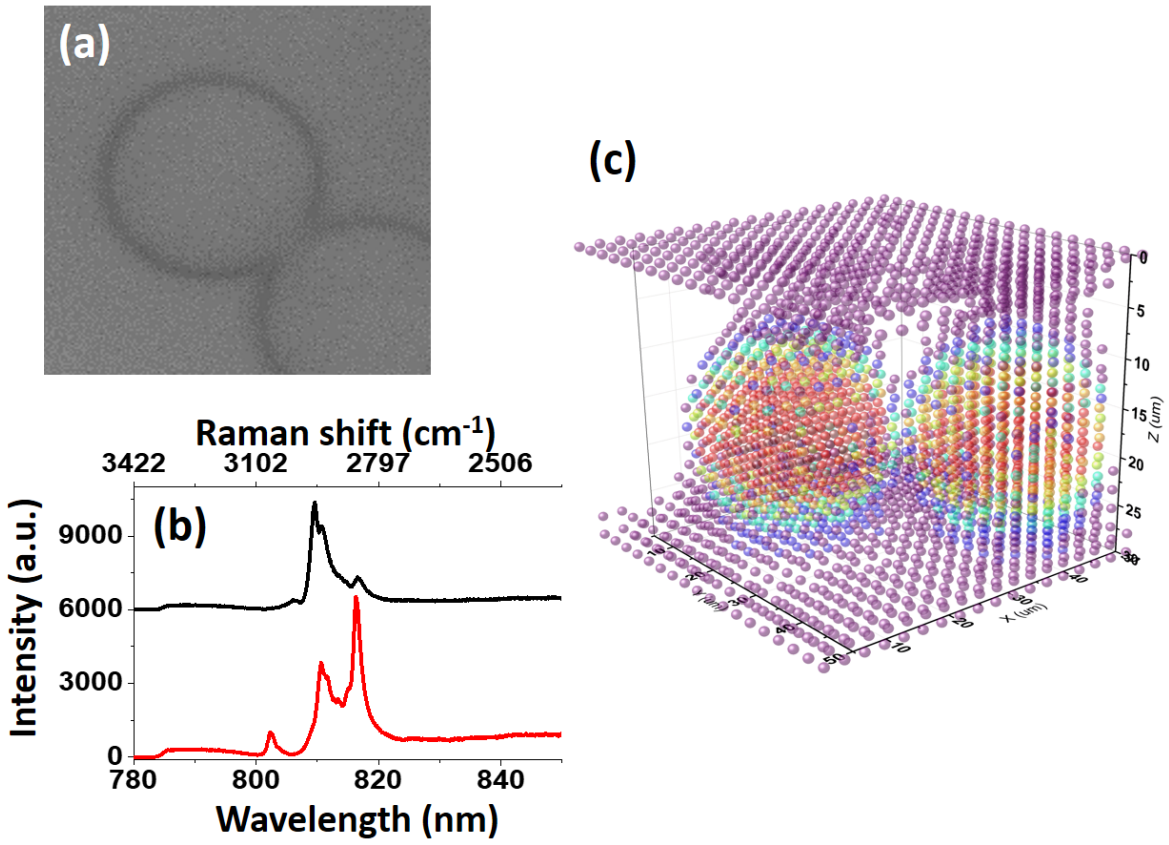

Figure 4.17: 3D CARS microspectroscopy of PMMA beads. (a) Bright-field image of the target beads. (b) CARS spectra of PMMA (black) and immersion oil (red). (c) Color-coded 3D CARS image of the PMMA beads.

advantage in spatial resolution to the microspectroscopy system.

We also note that, given the efficiency roll-off of the CCD close to and above 1000 nm, it is necessary to assign more power in the low wavenumber region so that the final CARS signal had higher signal-to-noise ratio across the detection range. In this sense, it is reasonable to use a 2-m-long fiber, which offers optimal power ratio and produces relatively insignificant group delay dispersion.

As compared to standard multiplex CARS scheme using highly nonlinear PCF, our microscope gives similar performance in the C-H stretching region. The glycerol signal from the standard setup [37] was also giving $\sim$10000 counts, with an effective integration time of 5 ms, and a laser power of 13 mW and 12 mW for the pump and the Stokes beam, respectively. For our result in Fig. 4.15a, a similar count number was reached with 20 times longer integration time, but weaker laser energy. Providing the same excitation power and same integration time, our setup can potentially yield higher count number. But it should be noted that due to the efficient intra-pulse excitation, a femtosecond multiplex CARS system offers more efficient detection in the finger-print region [37]. Further improvement on our setup include choosing appropriate focusing objective for tighter focus, as well as taking a deeper look into the SC generation in LMA fibers— for example, by pumping further into the normal dispersion region so as to form compressible high-energy SC [151].

In conclusion, we have demonstrated SC pulse generation in LMA PCF with micro-joule pulse energy and Watt-level output power. Different fiber parameters have been tested, and their effects on the spectral and temporal behavior of the generated SC were evaluated. Theoretical simulation has been carried out to provide additional insights into mechanisms of the SC generation, and showed good agreement with the experimental results. We have demonstrated CARS spectroscopy in the ambient air, as well as CARS imaging of microspheres and diamond flakes using this optimized SC source. We have also constructed a CARS microscope based on the SC source, and have shown its scanning capability. We believe this will be an alternative and preferable CARS microspectroscopy setup for biomedical and other applications [54].

5. WIDE-FIELD COHERENT ANTI-STOKES RAMAN SCATTERING MICROSCOPY USING PICOSECOND SUPERCONTINUUM *

Modern microscopic technologies such as bright-field, dark-field, phase contrast, confocal, and fluorescence microscopy has served as vital tools in material science and biology [152]. Raman scattering, as we have mentioned in the first chapter, has also seen significant development in microscopic applications, due to its capability in chemical-specific imaging. This include researches over a broad range of studies such as petrography, pharmacy, and polymer science. Commercialized Raman microscopes has also become available in the recent decades. However, the employment of Raman microscopy in practical imaging system, especially those requiring fast imaging speed and high frame rate, has been limited due to its low scattering efficiency, as well as the commonly existed autofluorescence background from the sample.

Then, benefiting from its high signal level and the automatically satisfied phase-matching condition under tight focusing [31], CARS microscopy has been adopted as the promising new tool for chemical-sensitive imaging, and implementations of CARS microscopy so far are largely based on laser scanning methods [37, 41, 128]. However, for fast imaging applications that cover a significant number of pixels, there is a severe limitation on the pixel dwell time, and so far only materials with large CARS scattering cross-sections have been used in video-rate imaging [35]. Wide-field CARS imaging, as an alternative to laser-scanning-based CARS imaging, allows simultaneous illumination and collection over a wide region, and could potentially enhance acquisition speed [44]. In this chapter, we give a brief overview on the wide-field CARS development, and present our work on wide-field CARS microscopy using the SC source based on LMA PCF described in the last chapter. Video-rate imaging of a standard polymer bead sample is demonstrated, and we discuss the advantages and limitations of our wide-field CARS system, as well as possible ways of improvements.

*Reprinted with permission from "Wide-field coherent anti-Stokes Raman scattering microscopy based on picosecond supercontinuum source" by Y. Shen, J. Wang, K. Wang, A. V. Sokolov, and M. O. Scully, 2018. *APL Photonics*, 3, 116104, Copyright [2018] by Creative Commons Attribution (CC BY) License.

5.1 Introduction to wide-field coherent anti-Stokes Raman scattering microscopy

In the wide-field CARS scheme, nonlinear image is directly obtained by using a wide-field excitation. An early wide-field CARS scheme used complicated illumination geometry to satisfy the phase-matching condition [142, 153]. In that work, the degenerate pump and probe beams were focused by a dark-field condenser, such that a ring of light was incident upon the sample at a range of angles. The Stokes beam then came from below with normal incidence. Such a beam configuration allows a phase-matched CARS signal to be generated, propagating in the direction opposite to the Stokes beam [142]. However, this exotic illumination geometry requires complicated optics, and the 10-Hz repetition rate high-energy laser used in that experiment was not suitable for fast imaging applications.

Schemes using simpler illumination geometries have also been demonstrated [154, 155], in which the pump and the Stokes beam with finite offset angle were guided onto the sample. To avoid laser damage in the collection optics, excitation beams were eliminated before entering the imaging objective. This was done using either a dark-field type collection scheme, or using a skewed illumination with large inclination angle, such that incident beam did not enter the objective [154]. Another way is to directly reject the light by a filter in front of the objective [155], but this can potentially cause image distortion or enhanced background due to the filter itself. Note that CARS signal generated in this fashion predominantly resulted from nonphase-matched scattering inside the sample [156], and therefore could lead to lower signal level as compared to the phase-matched case.

By adopting these wide-field schemes, video rate imaging and even single-shot imaging of standard and biological sample have been demonstrated [153, 154, 155, 156]. The simplification in illumination setup and enhancement in imaging frame rate has made wide-field CARS microscopy very promising for applications in high-speed biomedical imaging. Still, wide-field CARS schemes demonstrated so far are based on narrowband CARS excitation, and often require complicated wavelength extension unit like optical parametric oscillator or OPA; simpler scheme has adopted Raman shifter to produce the Stokes beam, yet here the detection band is limited by the shifter

element [154].

Here we present a wide-field CARS microscopy setup based on the multiplex CARS excitation scheme [157]. By using the broadband, high energy SC source generated through LMA PCF, multiple Raman bands can be excited over a wide region, and CARS imaging targeting at specific Raman vibrations can be achieved by applying corresponding bandpass filter during imaging. We demonstrate its chemical selectivity by imaging a mixture of PS and PMMA microspheres, as well as nanodiamond flakes. We also show its capability of video-rate imaging using the polymer bead sample, and discuss its applicability as well as limitations.

5.2 Wide-field coherent anti-Stokes Raman scattering microscopy based on supercontinuum from large-mode-area photonic crystal fiber

5.2.1 Setup description

The supercontinuum generation setup were the same as that described in the last chapter [104], and a sketch of the CARS imaging system is shown in Fig. 5.1b. In brief, the output of a picosecond laser (APLX-10, Attodyne), with 1 MHz repetition rate and 10 μJ pulse energy at 1064 nm, was divided into two parts: one was used to pump a 2-meter-long LMA PCF (LMA-20, NKT Photonics) to generate the SC light, which was used as the Stokes beam; the other part was sent through a delay stage and served as the pump beam. The Stokes beam then passed through a long-pass filter (FELH1150, Thorlabs), and recombined with the pump beam on a dichroic beam splitter (LPD02-1064RU-25, Semrock). Both were focused collinearly onto the sample using an off-axis parabolic mirror with a focal length of 100 mm. The diameter of the focal spot was measured to be 32 μm.

Figure 5.1a illustrates the illumination and the collection scheme. After the sample, the forward-scattered beam was collimated by a microscope objective (100x LE Plan, Nikon). The excitation light was blocked by spectral filters, while the CARS signal passed through. The sample image was projected onto the camera through a tube lens with focal length of 200 mm. A common short-pass filter (FESH1000, Thorlabs) was used to block the excitation light, while different bandpass fil-

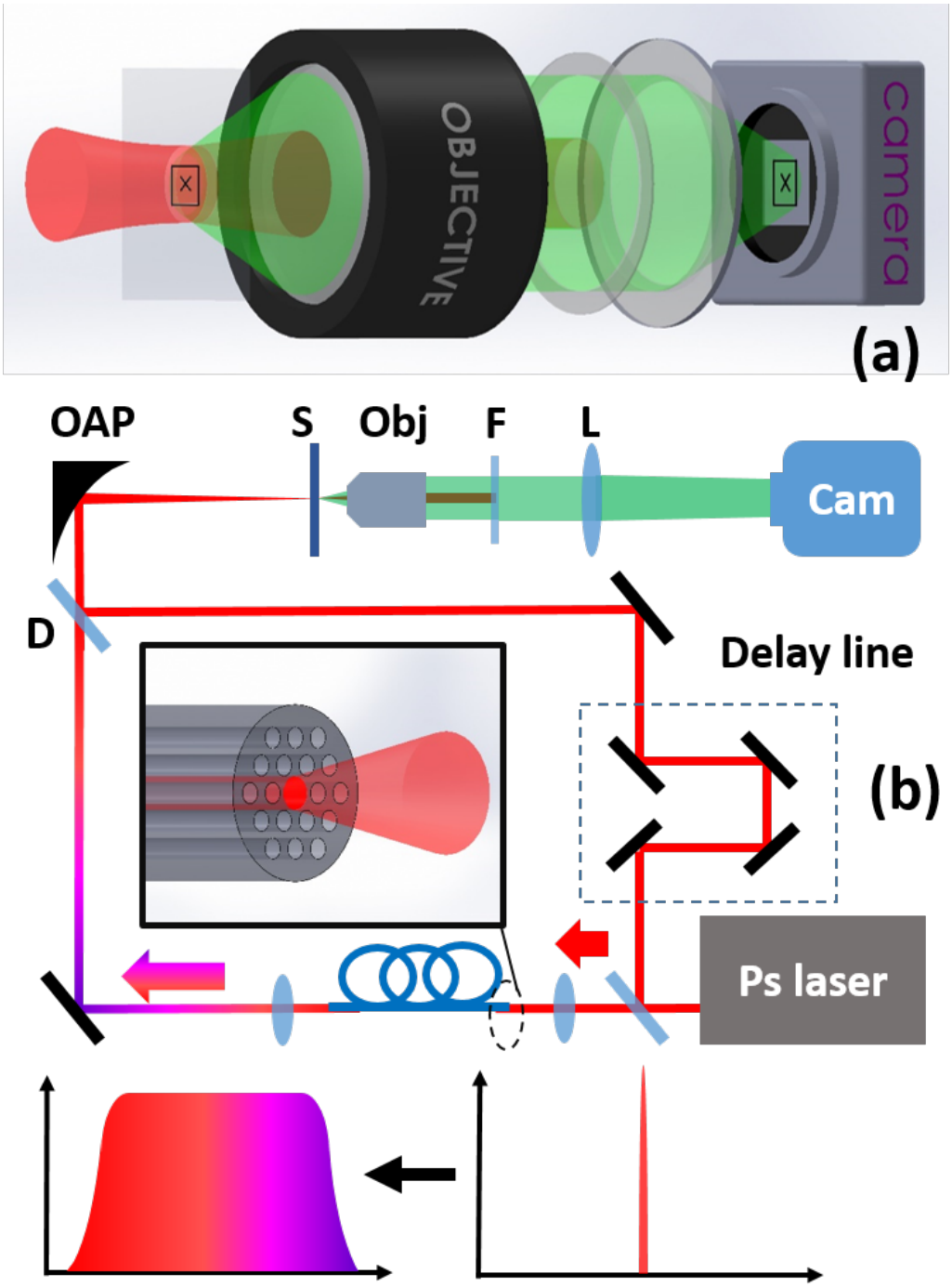

Figure 5.1: (a). Schematic drawing of the wide-field CARS imaging. Excitation beam (red) illuminates a wide area at sample plane (black rectangle), and the CARS signal (green) from a small object (black cross) is collected by the objective and imaged onto the camera after filter and tube lens. (b). Experimental setup of the wide-field CARS microscopy. D: dichroic beam splitter; OAP: off-axis parabolic mirror; S: sample; Obj: microscope objective; F: filter; L: tube lens; Cam: imaging camera. The inset sketches the PCF input coupling.

ters were used to address different Raman bands: a bandpass filter centered at 800 nm (FBH0800, Thorlabs) was used to image the aromatic C-H stretch around 3050 cm^{-1}; another bandpass filter centered at 810 nm (FBH0810, Thorlabs) was used for the aliphatic C-H stretch around 2950 cm^{-1}; a tunable bandpass filter consisted of a tunable long-pass (TLP01-995-25x36, Semrock) and a tunable short-pass (TSP01-995-25x36, Semrock) filter was used to select Raman bands in the fingerprint region. The filters chosen resulted in a spectral resolution of 140 cm^{-1} and 35 cm^{-1} when detecting in the C-H stretching region and the fingerprint region, respectively. For the imaging camera, we tested the system with both a high-end CCD (iKon934, Andor) and a scientific CMOS (sCMOS) camera (DHYANA 95, Tucsen).

PS and PMMA microsphere were obtained in the form of aqueous solutions (Sigma Aldrich), with bead sizes of 3 μm and 4 μm, respectively. The mixed sample was prepared by mixing the two solutions at 1:1 ratio and depositing the bead mixture onto a low-density polyethylene (LDPE) film (Glad Corporation). Nanodiamonds were also purchased in the form of aqueous solution (Columbus NanoWorks), and were deposited on the LDPE film to form clustered flakes. L-cystine powders (Sigma Aldrich) was deposited on a thin polyethylene terephthalate (PET) film (GoodFellow).

5.2.2 Result analysis

To demonstrate chemical selective imaging, we first show the results obtained from the PS and PMMA bead mixture. The bright-field image of the sample is shown in Fig. 5.2a, and the PS and PMMA beads can be clearly distinguished by their sizes. Figure 5.2b and 5.2c show the CARS images obtained with the 800 nm and 810 nm filter, respectively. By applying the 800 nm filter, the aliphatic C-H stretch signal from PMMA is rejected, and therefore only PS beads are visible in Fig. 5.2b. On the other hand, when applying the 810 nm filter, the PMMA bead in the center becomes bright, while the PS beads are dimmed but still visible due to the residual PS signal in this spectral region. In Fig. 5.2d we plot the CARS spectra acquired when focusing on either a PS or a PMMA bead using the home-built CARS microscope described in the previous chapter. Notice that there are also contributions from the LDPE substrate in these spectra [158], but such background signal

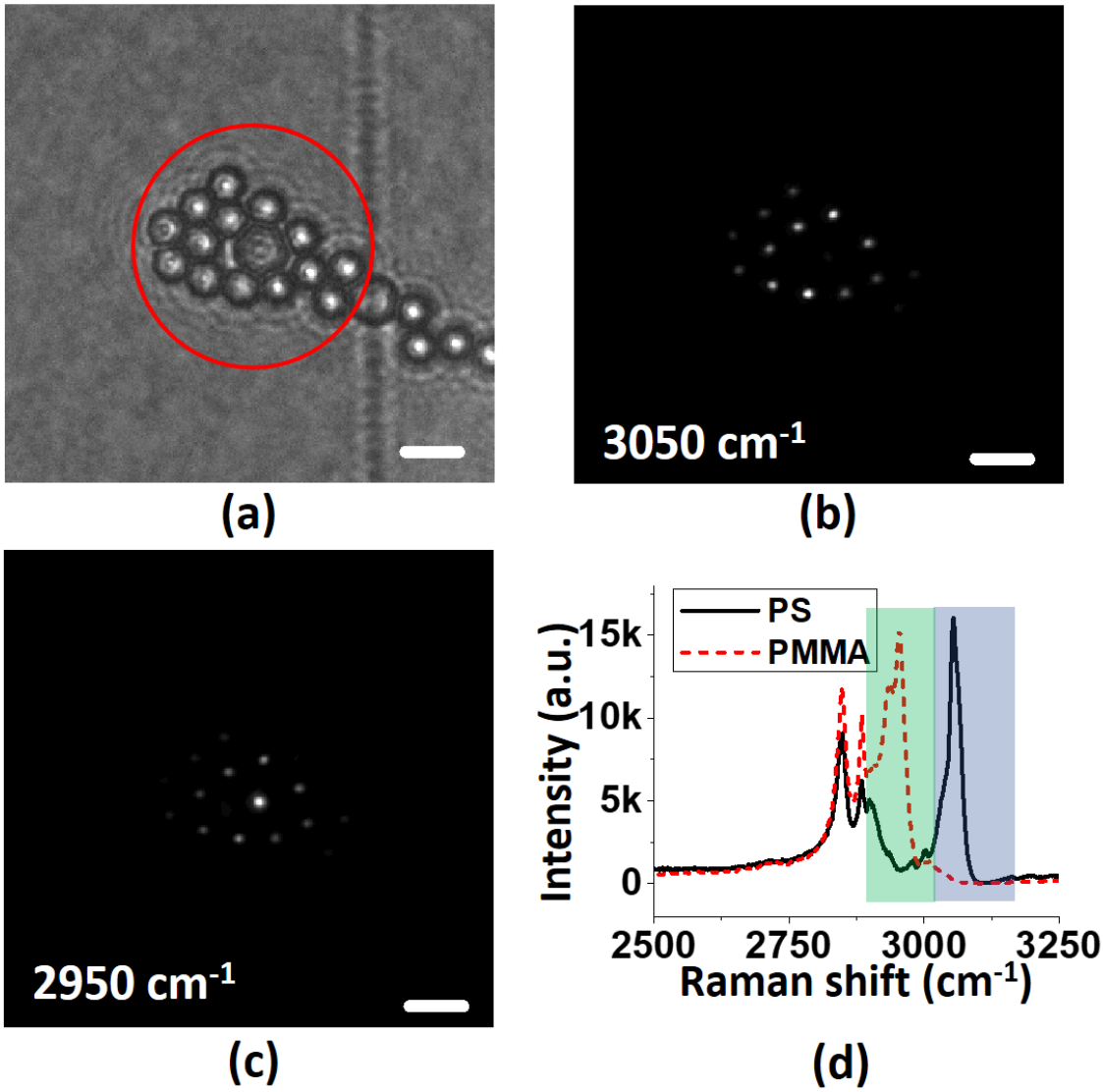

Figure 5.2: CARS images of PS and PMMA mixture captured by the CCD camera. (a) Bright-field image of the bead mixture, with red circle indicating CARS imaging area. (b) CARS image of the mixture using the 800 nm bandpass filter, corresponding to the 3050 cm^{-1} band of PS. (c) CARS image of the mixture using the 810 nm bandpass filter, corresponding to the 2950 cm^{-1} band of PMMA. (d) CARS spectra of a PS bead (black straight line) and PMMA bead (red dashed line). The bandpass region of the 800 nm and 810 nm filters are marked in blue and green, respectively. The scale bars in the figures correspond to 5 μm.

is not significant in the CARS image as the surroundings appeared to be dark, and the bead signals were dominant, with an SNR exceeding 100. However, we note that images of the beads in the wide-field CARS image in Fig. 5.2b and 5.2c appeared to be much smaller as compared to their bright-field image (Fig. 5.2a). This can be attributed to the index mismatch between the bead and the surrounding medium (air), and the beads acting effectively as micro-lenses and focusing the incident light, causing a bright center spot with a dark periphery. Here images were acquired using the CCD camera, and the integration time was set to 100 ms. The power of the pump and Stokes beam on the sample were measured to be 30 mW and 15 mW, respectively.

We also demonstrate CARS imaging in the fingerprint region using nanodiamond flakes as sample. Figure 5.3a shows the bright-field image of the clustered diamond flakes. We used the tunable bandpass filter to select the imaging wavelength. The off-resonance and on-resonance CARS images of the flakes are shown in Figs. 5.3b and 5.3c, respectively. In Fig. 5.3d we also plot the CARS spectrum acquired by the home-built CARS microscope, when focused on a single spot within the diamond cluster. By tuning to the diamond resonant peak around 1320 cm^{-1}, we can see bright spots showing up on the flake in Fig. 5.3c, while in the off-resonant case, no detailed feature is visible. The constant background signal seen in Fig. 5.3b and 5.3c was visible when tuning the bandpass filter throughout the fingerprint region; and it could be attributed to the non-resonant signal originating from the interface of diamond and the polymer substrate. Again images were acquired by the CCD camera with the same integration time and power.

Benefited from the high signal-to-noise ratio in the bead sample images, we can perform video-rate imaging using an sCMOS camera. Figures 5.4a and 5.4b show the images obtained from the PS and PMMA mixture using the sCMOS camera, with the 800 nm and 810 nm bandpass filter applied, respectively. Again we can see that PMMA beads did not show up in Fig.5.4a due to the selected imaging band. The integration time used here was 38 ms, with the power on the pump and Stokes increased to 50 mW and 40 mW, respectively. Under such settings, we can achieve a frame rate of 25 fps, with an SNR larger than 20.

As a demonstration towards practical application, we performed microscopy on L-cystine mi-

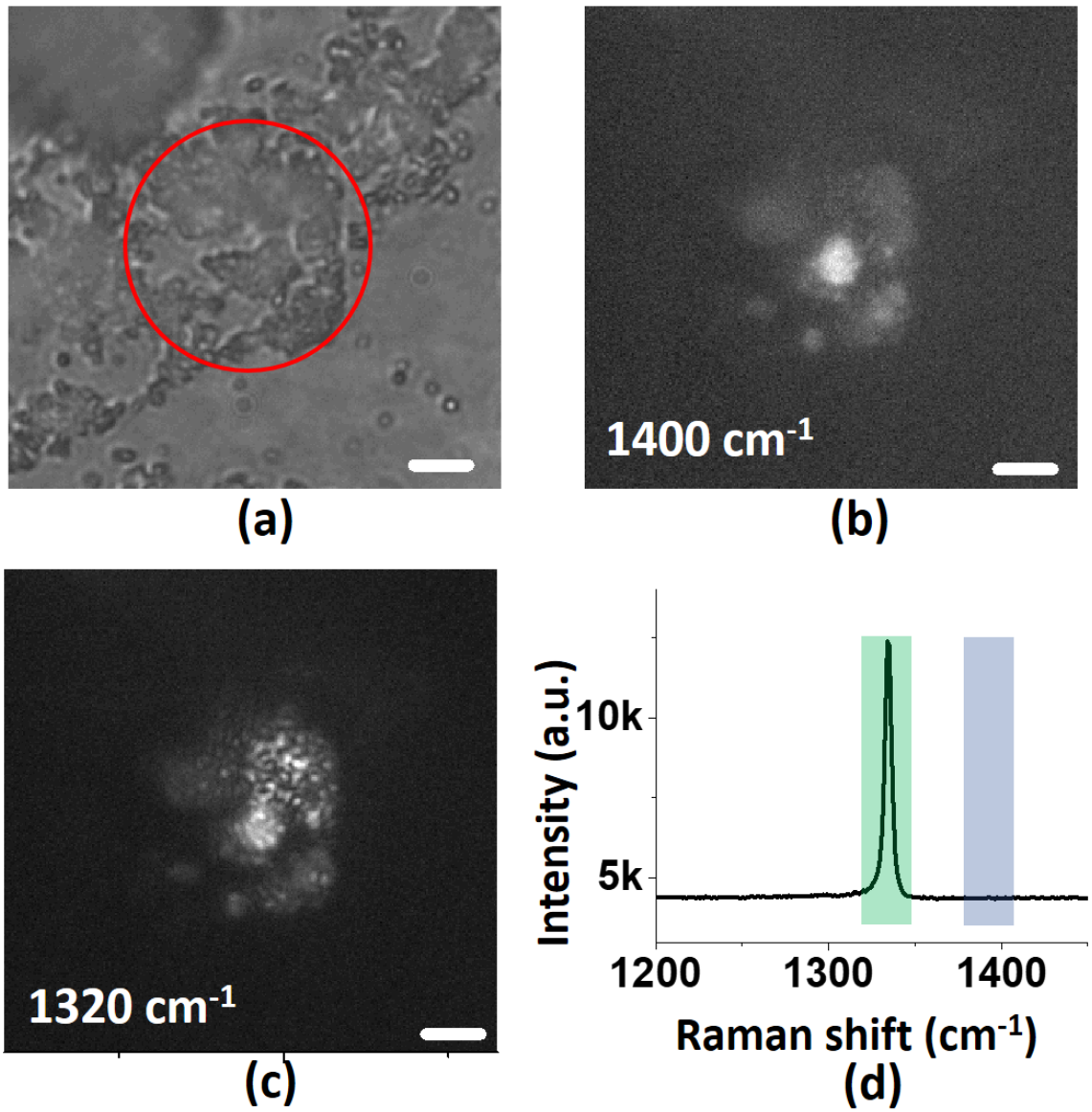

Figure 5.3: CARS images of the diamond flake captured by the CCD camera. (a) Bright-field image of the flake, with red circle indicating CARS imaging area. (b) CARS image of the flake when tuned off-resonant around 1400 cm^{-1}. (c) CARS image of the flake when tuned on-resonant at 1320 cm^{-1}. (d) CARS spectra when focused on diamond, and the bandpass region of off-resonance and on-resonance state are marked in blue and green, respectively. The scale bars in the figures represent 5 μm.

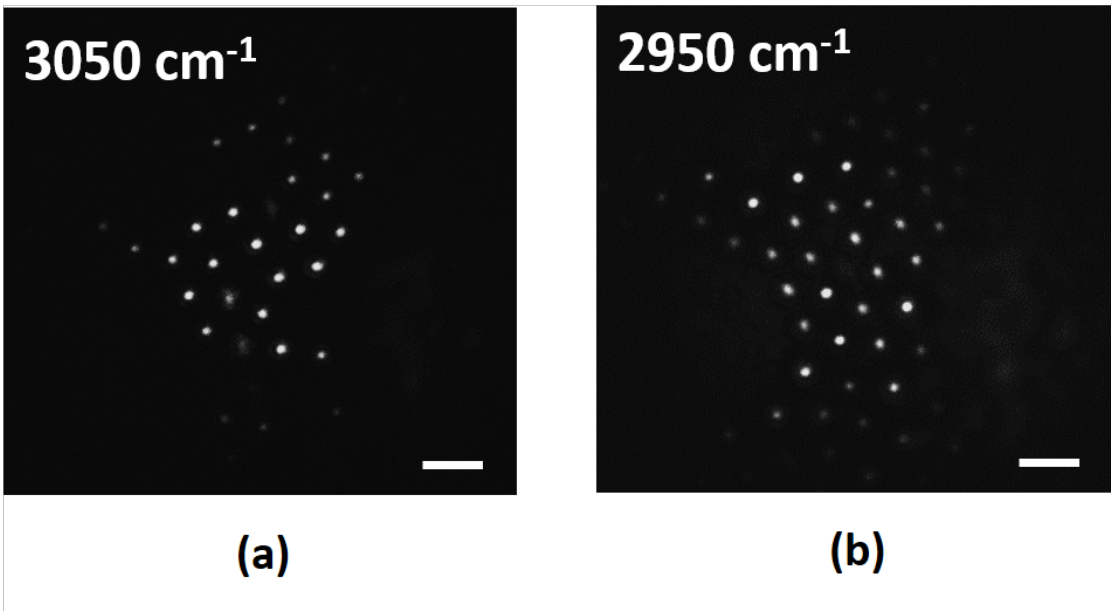

Figure 5.4: Video-rate CARS imaging of the PS and PMMA bead mixture. (a) CARS image using the 800 nm bandpass filter. (b) CARS image using the 810 nm bandpass filter. The scale bar in the figures represent 5 μm.

crocrystalline. L-cystine is an oxidized dimeric form of cysteine, and is highly concentrated in the immune system, skeletal and connective tissues, skin, digestive enzymes, and in hair [159]. Figure 5.5a shows the bright-field image of the microcrystalline, and Fig. 5.5b is the CARS image obtained by applying the 810 nm bandpass filter, corresponding to its C-H stretching signal shown in Fig. 4.15b [160]. Note that due to the non-phase-matched nature of the imaging scheme [156], signal occurred mostly in regions where internal refraction and scattering was significant. Therefore only certain spots appeared to be bright. The CARS nature of the signal was verified by switching to the 800 nm filter and noticed that the image turned completely dark. The pump and Stokes power used here were 35 mW and 30 mW, respectively, with an image integration time of 200 ms.

5.3 Discussions

The estimated average laser fluence in the current setup is 10 mJ/cm^2, which is lower compared to the system using an amplified ultrafast laser [154], but higher than that using oscillator-only

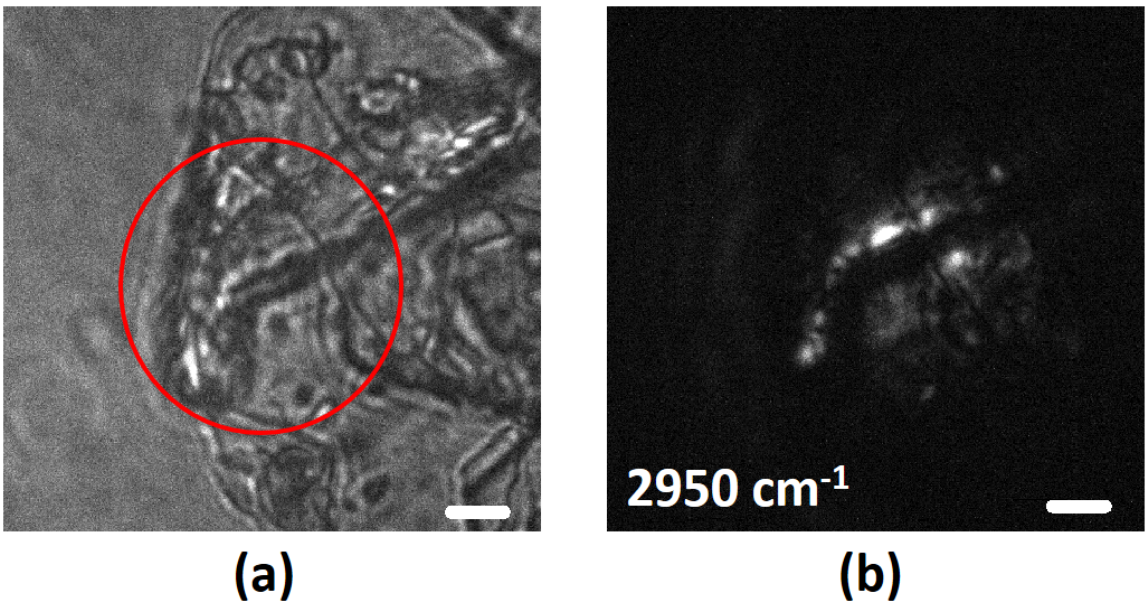

Figure 5.5: CARS imaging of L-cystine microcrystalline. (a) Bright-field image of the microcrystalline, and (b) the corresponding CARS image in the 2950 cm^{-1} region (810 nm bandpass filter). The scale bars in the figures represent 5 μm.

pulses [156]. This is reasonable due to the relatively low intensity contained in each spectral component in the SC pulse, which in turn calls for higher pulse energy to reach significant level of CARS signal. Yet the advantage of the SC excitation as compared to previous wide-field CARS microscopy schemes is that multiple bands can be stimulated simultaneously such that more information from the target could be obtained in a single collection. Such an idea of broadband wide-field excitation has been demonstrated earlier using amplified femtosecond pulses for relatively large scale gas imaging [161]. But our setup is more suitable for microscopy due to the longer wavelength, less pulse energy, and longer pulse duration used, which induce less sample damage [162]. Still, additional studies are needed to determine and to achieve optimized parameters and pulse settings that provide optimal balance between the signal level and sample damage, based on different target samples.

In terms of spectral performance, we note that the resolution of the system can be further enhanced simply by choosing filters with narrower pass band, but this has to be compensated

by the increase in integration time so as to achieve desired SNR. Also, with more Raman bands involved in imaging, significant complication to the detection system is expected. Therefore when it comes to hyperspectral imaging where many Raman bands need to be addressed simultaneously, the current scheme will be less favorable compared to laser-scanning-based CARS [37, 63]. The fundamental limit is due to the low spectral intensity in the excitation, and can be resolved with an improved SC source. On the other hand, if the sample components are known and only a few well-separated Raman bands are of interest, our setup can be a solution regarding high-speed imaging applications.

The observed bead image distortion due to refractive index mismatch has also been seen in previous wide-field CARS using non-phase-matched illumination [156, 155]. On the other hand, phase-matched wide-field CARS displayed no significant distortion on the oil droplet image, possibly due to less distortion caused by a planar object and their better sectioning capability [153]. Refractive index mismatch distortion has been reported in laser-scanning CARS imaging as well [163, 164], but showed less impact in terms of planar imaging of bead samples as compared to our wide-field CARS scheme. We expect our system to perform better on planar structures where refractive index mismatch distortion is less severe, but image correction of more complicated structures requires further research.

Other limitations of our current setup include non-uniformity in the excitation field— the Gaussian beam profile causes the center of the image to be brighter while the edge completely dark. Although numerical correction is possible by normalizing the signal to the excitation intensity profile, this will also enhance the noise level on the edge. A preferable way to flatten the field is to enhance the illumination area, which will in turn call for more power of the excitation beams, particularly the supercontinuum beam. Current setup allows a useful power of 140 mW in the Stokes beam, but higher useful power can be obtained by adjusting the length of the fiber or by using a polarization-maintaining PCF [104]. Another issue is the instability in signal, which largely arises from the nonlinear nature of the CARS process and the SC generation, and further deteriorated by other fluctuations such as the laser-pointing instability and air turbulence. It is of interest in the

future to develop a wide-field scheme that does not require nonlinear broadening [165] or is based on an all-fiber setup [129], so as to reduce such fluctuations.

We also note that the substrates were chosen to be thin films here, to minimize the background FWM signal. When depositing samples onto coverslip up to hundreds of micron thick, we noticed a strong nonresonant background appearing around the microspheres despite the phase-mismatch. This background could be generated in the vicinity of the sample-substrate interface, and due to the depth of focus of the objective, ended up in the imaging camera. A more elegant solution to this problem could be using the tunable filter and performing a frequency-modulation measurement, such that when taking the difference between two images with close-wavelength separation, the nonresonant background is eliminated and the resonant signal is enhanced [91].

Lastly, given that a majority of the spectral components are not used when imaging with a specific Raman band, it can be advantageous to put a tunable filter in the Stokes path of our setup. This will allow programmable excitation that can be rapidly switched (such as an acousto-optic tunable one [166, 167]), which is beneficial for high speed biological imaging and cytometry. Also, with the advancement in SC generation, a more powerful SC pulse with high spectral coherence could be implemented to achieve better background suppression through temporal control [40] and better sensitivity through coherent intra-pulse excitation [37].

In conclusion, we have demonstrated a multiplex wide-field CARS imaging setup. By using the high energy picosecond supercontinuum pulse for excitation, different Raman band imaging was achieved by applying corresponding filters. We were able to perform video-rate CARS imaging of standard sample. Such a scheme can be applied in cytometry, gas sensing, and other biomedical disciplines where high-frame-rate imaging of various species is required. It is also promising to combine with compressed sensing to achieve high-speed hyperspectral imaging.

6. SUMMARY AND FUTURE OUTLOOK

In the aim of developing high-speed and highly sensitive CARS microspectroscopy system for practical applications, we have reviewed major CARS development in this thesis, and have reported several experiments conducted using our home-built CARS systems. Our initial trial was based on the single-beam CARS scheme, which is considered to be relatively easy to implemente. By using only an ultrafast oscillator source and basic optical components, we were able to construct a pulse-shaper-based single-beam CARS system using spectral hole for signal retrieval. Such a system demonstrated improved epi-detection efficiency as compared to earlier experiments, and showed promising applicability in Raman band detection in the low-wavenumber region, thanks to the spatial filtering mechanism implemented in the pulse shaper.

In a later design, we further simplified the pulse shaper by adopting a folded-geometry, and incorporated FAST technique to allow probe pulse shaping and temporal delay. The resulting system showed high versatility in selecting beam layout and detection scheme. We demonstrated significant nonresonant background suppression, and showed highly sensitive detection using the collinear pump/probe beam geometry. Still, such detection requires a separate background collection stage, which slows down the overall processing speed. We resolved this issue through heterodyne detection, i.e., by precisely controlling the delay modulation of the probe pulse such that the difference between two anti-Stokes spectra with desired phase difference could be obtained. We provided the theoretical treatment of retrieving Raman mode information through such detection. We have also incorporated spectral detection in the pulse shaper design such that no external spectrometer is required, and the whole system can be made into a compact module. We demonstrated CARS microscopy using this setup, and discussed its limitations and possible improvements to enhance the detection speed.

However, with single-beam scheme based on a single laser oscillator, we are limited in the detection bandwidth. Despite earlier demonstration using ultra broadband Ti:Sapphire oscillator to achieve CARS detection of large Raman shifts [168], more common means to perform broad-

band CARS detection is to use wavelength extension unit. Therefore we exploited SC generation in LMA PCFs. We observed SC generation beyond 1600 nm, corresponding to a Raman shift of more than 3000 cm^{-1} from the pump wavelength (1064 nm). We have further constructed a CARS microspectroscopy system to verify its applicability, and demonstrated microscopy on several samples.

Taking advantage of the high pulse energy from the SC source, we have applied this system to wide-field CARS imaging. Previous demonstrations of wide-field CARS have been limited in the two-color excitation scheme such that a single Raman mode is probed at a time. By using the SC source as the Stokes beam, we can, in principle, excite and probe multiple Raman modes in a single acquisition. We have demonstrated selective imaging using polymer beads, and have shown video-rate imaging capability in the C-H stretching region. Wide-field CARS system that can take full advantage of the multiplex excitation will require more research, especially on the method for hyperspectral detection and image correction.

It would be of great interest to combine the broad spectral coverage of the SC generation with the single-beam CARS technique to achieve a simple yet useful CARS system. As we have pointed out earlier, another common disadvantage in the single-beam CARS scheme implementing narrowband probe within the broadband pulse is that the probe power is typically much weaker as compared to those in multiplex CARS schemes, indicating a low efficiency in CARS signal generation. Spectral focusing [89] can be an effective way to obtain optimal power ratio between the probe and pump beams. Another way is to directly shape a broadband pulse that contains a particular strong spectral components and can be used as the narrowband probe. Recently we have examined the self-phase modulation (SPM) of amplified femtosecond pulse through a relatively long piece of LMA PCF and found significant broadening due to SPM. This has been used previously in pulse compression [151], but with relatively short fiber length. By using LMA fibers up to 1 m, we noticed broadening up to 300 nm, as shown in Fig. 6.1. Here the input pulse was from amplified Ti:Sapphire system (Astrella, Coherent) with close to 90 fs duration measured from autocorrelation trace, and pulse energy around 100 nJ.

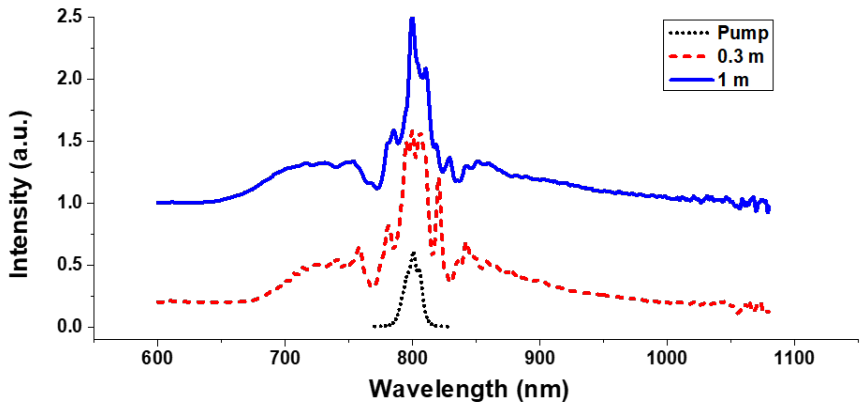

Figure 6.1: Spectral broadening of Ti:Sapphire laser pulse in LMA PCF due to self-phase modulation (SPM). The spectrum of the original pulse, broadened pulse after 0.3 m LMA-20 fiber, and that after 1-m-long LMA-20 fiber are shown in black dotted, red dashed, and blue solid lines, respectively.

Given that an effecient pulse compression method can be implemented through a prism compressor, we can directly inject this pulse into a pulse shaper, and pick a narrowband in the high power region (∼800 nm) as a probe pulse, and carry out the single-beam CARS experiment. High pulse energy can be sustained by using the LMA fibers, and compressible supercontinuum can provide sub-10 fs pulse, which in turn offers highly efficient intrapulse excitation— these are beneficial factors in enhancing CARS signals [45, 54]. It is also possible to use part of the generated SC as LO and perform heterodyne CARS [71]. On the other hand, along the line of SC generated from SPM, we can incorporate cascaded pumping by adopting a dispersion compensation stage between two LMA fibers to further increase the bandwidth of the generated SC [169].

Another possible direction of enhancing the CARS sensitivity is to embed the target molecule into hollow-core (HC) fibers. This has been demonstrated in both spontaneous Raman spectroscopy [170] and CARS [171] earlier, and the primary enhancement comes from the elongated interaction length. However, for nonlinear processes like CARS using ultrashort pulses, there will be temporal walk-off due to dispersion in the medium [46]. Therefore the dispersion in the fiber needs to be tailored to satisfy the phase-matching condition in order to enjoy such enhancement [171, 172]. Thanks to the fast development in HC PCF, there are now fibers with ultra broadband

transmission. Figure 6.2 shows such a commercial fiber with core size close to 40 μm (PMC-C-650_2000-7C, GLOphotonics), and a comparison of CARS spectra obtained by focusing in the free-space, and by passing through a 100mm-long fiber are shown in Fig. 6.2c.

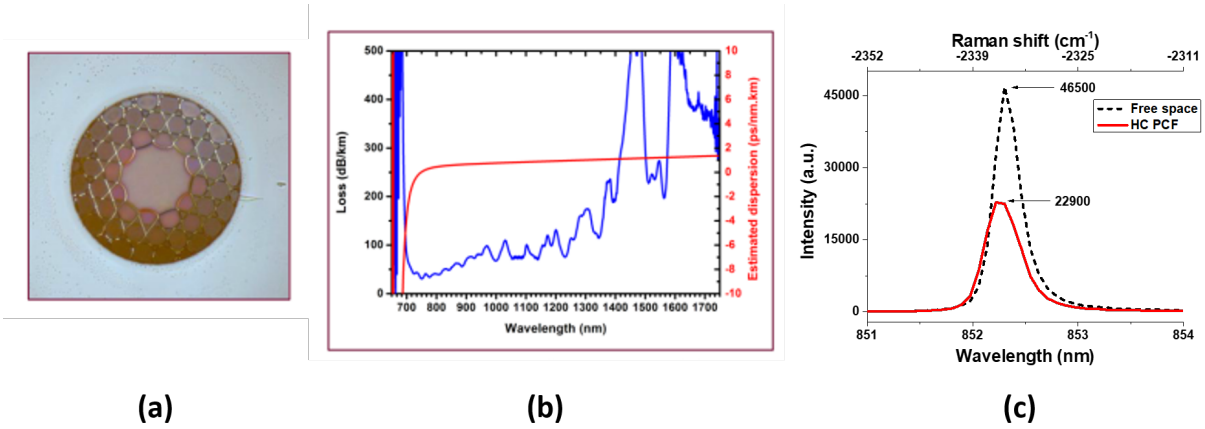

Figure 6.2: (a) Cross section of the commercial hollow-core (HC) PCF. (b) Transmission and dispersion curve of the fiber. (c) CARS peak of nitrogen obtained in free space (black dashed) and through 100mm-long HC PCF (red solid).

The pump and Stokes power used in free space detection are 143 mW and 130 mW, respectively, while that for HC PCF are 25 mW and 20 mW, respectively. Therefore, the HC PCF offered a signal enhancement of 100-times as compared to that in free space. Note that the nitrogen peak level in free-space decreased as compared to that shown in Fig. 4.11 due to the difference in CCD read-out speed setting. Such enhancement in HC PCF be further improved by adopting longer fiber, and by controlling the phase-matching condition inside the fiber through pressure control of buffer gas.

Since the start of the century, the field of CARS spectroscopy and microscopy has seen unprecedented growth— in both the available schemes and technologies, as well as in the diverse fields of applications. Previously known as only a laboratory tool for chemical analysis, nowadays CARS has evolved into a more accessible technology with less expensive instrument and refined method available to a wider range of users. We expect that it will appear in clinical applications and

even in consumer-grade products in the coming decades, and also continue to improve and rival that of fluorescence and other nonlinear microspectroscopy in chemical and biological imaging.

REFERENCES

[1] R. S. Krishnan and R. K. Shankar, "Raman Effect: History of the Discovery," *Journal of Raman Spectroscopy*, vol. 10, pp. 1–8, 1981.

[2] C. V. Raman and K. S. Krishnan, "A New Type of Secondary Radiation," *Nature*, vol. 121, pp. 501–502, 1928.

[3] A. Smekal, "Zur Quantentheorie der Dispersion. (German) [on the quantum theory of dispersion]," *Naturwissenschaften*, vol. 11, pp. 873–875, 1923.

[4] Y. Rocard, "Les nouvelles radiations diffusies. (French) [new diffused radiations]," *Comptes Rendus*, vol. 186, p. 1107, 1928.

[5] J. Cabannes, "Un nouveau phenomene d'Optique: les battements qui se produisent lorsque des molecules anisotropes en rotation et diffusent de la lumiere visible ou ultraviolette. (French) [a new optical phenomenon: the beating that occurs when anisotropic molecules rotate and diffuse visible or ultraviolet light]," *Comptes Rendus*, vol. 186, p. 1201, 1928.

[6] G. Landsberg and L. Mandelstam, "Eine neue Erscheinung bei der Lichtzerstreuung in Krystallen. (German) [a novel effect of light scattering in crystals]," *Naturwissenschaften*, vol. 16, pp. 557–558, 1928.

[7] C. V. Raman and K. S. Krishnan, "A new class of specra due to secondary radiation. part I," *Indian Journal of Physics*, vol. 2, p. 399, 1928.

[8] A. Schawlow and C. Townes, "Infrared and optical masers," *Physical Review*, vol. 112, pp. 1940–1949, 1958.

[9] T. H. Maiman, "Stimulated Optical Radiation in Ruby," *Nature*, vol. 187, pp. 493–494, 1960.

[10] S. P. S. Porto and D. L. Wood, "Ruby Optical Maser as a Raman Source," *Applied Optics*, vol. 1, pp. 139–141, 1962.

[11] F. Adar, M. Delhaye, and E. DaSilva, "Evolution of Instrumentation for Detection of the Raman Effect as Driven by Available Technologies and by Developing Applications," *Journal of Chemical Education*, vol. 84, pp. 50–60, 2007.

[12] J. L. Koenig, "Raman spectroscopy of biological molecules: A review," *Journal of Polymer Science: Macromolecular Reviews banner*, vol. 6, pp. 59–177, 1972.

[13] F. S. Parker, *Applications of infrared, Raman, and resonance Raman spectroscopy in biochemistry*. Plenum Press, 1983.

[14] J. M. Chalmers and P. R. Griffiths, *Handbook of vibrational spectroscopy*. John Wiley Press, 2002.

[15] H. Kano, H. Segawa, P. Leproux, and V. Couderc, "Linear and nonlinear raman microspectroscopy: History, instrumentation, and applications," *Optical Review*, vol. 21, pp. 752–761, 2014.

[16] T. Dieing, O. Hollricher, and J. Toporski, *Confocal Raman Microscopy*. Springer Press, 2011.

[17] F. C. Thorley, K. J. Balwin, D. C. Lee, and D. N. Batchelder, "Dependence of the raman spectra of drug substances upon laser excitation wavelength," *Journal of Raman Spectroscopy*, vol. 37, p. 335, 2006.

[18] A. C. Ferrari and D. M. Basko, "Raman spectroscopy as a versatile tool for studying the properties of graphene," *Nature Nanotechnology*, vol. 8, pp. 235–246, 2013.

[19] S. Bernard, O. Beyssac, and K. Benzerara, "Raman mapping using advanced line-scanning systems: Geological applications," *Applied Spectroscopy*, vol. 62, pp. 1180 – 1188, 2008.

[20] C. Lofrumento, A. Zoppi, M. Ricci, E. Cantisani, and T. Fratini, "The first spectroscopic analysis of ethiopian prehistoric rock painting," *Journal of Raman Spectroscopy*, vol. 43, p. 1663, 2012.

[21] F. R. Perez and J. Martinez-Frias, "Raman spectroscopy goes to mars," *Spectroscopy Europe*, vol. 18, pp. 18–21, 2006.

[22] J. Jehlička, A. Culka, P. Vandenabeele, and H. G. M. Edwards, "Critical evaluation of a handheld raman spectrometer with near infrared (785 nm) excitation for field identification of minerals," *Spectrochimica Acta Part A: Molecular and Biomolecular Spectroscopy*, vol. 80, pp. 36–40, 2011.

[23] S. Steward, R. J. Priore, M. P. Nelson, and P. J. Treado, "Raman imaging," *Annual Review of Analytical Chemistry*, vol. 5, pp. 337–360, 2012.

[24] P. D. Maker and R. W. Terhune, "Study of optical effects due to an induced polarization third order in the electric field strength," *Physical Review*, vol. 137, pp. 801–818, 1965.

[25] R. F. Begley, A. B. Harvey, and R. L. Byer, "Coherent anti-stokes raman spectroscopy," *Applied Physics Letters*, vol. 25, p. 387, 1974.

[26] W. M. Tolles, J. W. Nibler, J. R. McDonald, and A. B. Harvey, "A Review of the Theory and Application of Coherent Anti-Stokes Raman Spectroscopy (CARS)," *Applied Spectroscopy*, vol. 31, pp. 253–271, 1977.

[27] M. D. Duncan, J. Reintjes, and T. J. Manuccia, "Scanning coherent anti-stokes raman microscope," *Optics Letters*, vol. 7, pp. 350–352, 1982.

[28] M. Aldén, h. Edner, and S. Svanberg, "Coherent anti-stokes raman spectroscopy (cars) applied in combustion probing," *Physica Scripta*, vol. 27, pp. 29–38, 1983.

[29] M. D. Duncan, J. Reintjes, and T. J. Manuccia, "Imaging biological compounds using the coherent anti-stokes raman scattering microscope," *Optical Engineering*, vol. 24, p. 242352, 1985.

[30] A. Y. Chikishev, G. W. Lucassen, N. I. Koroteev, C. Otto, and J. Greve, "Polarization sensitive coherent anti-stokes raman scattering spectroscopy of the amide i band of proteins in solutions," *Biophysical Journal*, vol. 63, pp. 976–985, 1992.

[31] A. Zumbusch, G. Holtom, and X. S. Xie, "Three-dimensional vibrational imaging by coherent-anti-stokes raman scattering," *Physical Review Letters*, vol. 82, pp. 4142–4145, 1999.

[32] M. Müller and J. M. Schins, "Imaging the thermodynamic state of lipid membranes with multiplex cars microscopy," *The Journal of Physical Chemistry B*, vol. 106, pp. 3715–3723, 2002.

[33] T. W. Kee and M. T. Cicerone, "Simple approach to one-laser, broadband coherent anti-stokes raman scattering microscopy," *Optics Letters*, vol. 29, pp. 2701–2703, 2004.

[34] H. Kano and H.-O. Hamaguchi, "Ultrabroadband (>2500 cm^{-1} multiplex coherent anti-stokes raman scattering microspectroscopy using a supercontinuum generated from a photonic crystal fiber," *Applied Physics Letters*, vol. 86, p. 121113, 2005.

[35] C. L. Evans, E. O. Potma, M. Puoris'haag, D. Côté, C. P. Lin, and X. S. Xie, "Chemical imaging of tissue in vivo with video-rate coherent anti-stokes raman scattering microscopy," *Proceedings of the National Academy of Sciences of the United States of America*, vol. 102, pp. 16807–16812, 2005.

[36] M. Jurna, J. P. Korterik, C. Otto, and H. L. Offerhaus, "Shot noise limited heterodyne detection of cars signals," *Optics Express*, vol. 15, pp. 15207–15213, 2007.

[37] C. H. C. Jr., Y. J. Lee, J. M. Heddleston, C. M. Hartshorn, A. R. H. Walker, J. N. Rich, J. D. Lathia, and M. T. Cicerone, "High-speed coherent raman fingerprint imaging of biological tissues," *Nature Photonics*, vol. 8, pp. 627–634, 2014.

[38] J. X. Cheng, L. D. Book, and X. S. Xie, "Polarization coherent anti-stokes raman scattering microscopy," *Optics Letters*, vol. 26, pp. 1341–1343, 2001.

[39] D. Oron, N. Dudovich, and Y. Silberberg, "Femtosecond phase-and-polarization control for background-free coherent anti-stokes raman spectroscopy," *Physics Review Letters*, vol. 90, p. 213902, 2003.

[40] D. Pestov, R. K. Murawski, G. O. Ariunbold, X. Wang, M. Zhi, A. V. Sokolov, V. A. Sautenkov, Y. V. Rostovtsev, A. Dogariu, Y. Huang, and M. O. Scully, "Optimizing the laser-pulse configuration for coherent raman spectroscopy," *Science*, vol. 316, pp. 265–268, 2007.

[41] C. L. Evans and X. S. Xie, "Coherent anti-stokes raman scattering microscopy: chemical imaging for biology and medicine," *Annual Review of Analytical Chemistry*, vol. 1, pp. 883–909, 2008.

[42] S. Roy, J. R. Gord, and A. K. Patnaik, "Recent advances in coherent anti-stokes raman scattering spectroscopy: Fundamental developments and applications in reacting flows," *Progress in Energy and Combustion Science*, vol. 36, pp. 280–306, 2010.

[43] J. Koivistoinen, P. Myllyperkiö, and M. Pettersson, "Time-resolved coherent anti-stokes raman scattering of graphene: dephasing dynamics of optical phonon," *The Journal of Physical Chemistry Letters*, vol. 8, pp. 4108–4112, 2017.

[44] J.-X. Cheng and X. S. Xie, *Coherent Raman Scattering Microscopy*. CRC Press, 2012.

[45] C. H. C. Jr. and M. T. Cicerone, "Chemically sensitive bioimaging with coherent raman scattering," *Nature Photonics*, vol. 9, pp. 295–305, 2015.

[46] R. W. Boyd, *Nonlinear Optics*. Academic Press, 2010.

[47] S. E. Harris and A. V. Sokolov, "Broadband spectral comb generation with refractive index control," *Physical Review A*, vol. 55, pp. R4019–R4022, 1997.

[48] M. D. Levenson and S. S. Kano, *Introduction to Nonlinear Laser Spectroscopy*. Academic Press, 1988.

[49] E. O. Potma, D. J. Jones, J. X. Cheng, X. S. Xie, and J. Ye, "High-sensitivity coherent anti-stokes raman scattering microscopy with two tightly synchronized picosecond lasers," *Optics Letters*, vol. 27, pp. 1168–1170, 2002.

[50] N. Dudovich, D. Oron, and Y. Silberberg, "Single-pulse coherently controlled nonlinear raman spectroscopy and microscopy," *Nature*, vol. 418, pp. 512–514, 2002.

[51] J. M. Dudley, G. Genty, and S. Coen, "Supercontinuum generation in photonic crystal fiber," *Reviews of Modern Physics*, vol. 78, p. 1135, 2006.

[52] H. A. Rinia, M. Bonn, M. Muller, and E. M. Vartiainen, "Quantitative cars spectroscopy using the maximum entropy method: The main lipid phase transition," *ChemPhysChem*, vol. 8, pp. 279–287, 2007.

[53] Y. Liu, Y. J. Lee, and M. T. Cicerone, "Broadband cars spectral phase retrieval using a time-domain kramers-kronig transform," *Optics Letters*, vol. 34, pp. 1363–1365, 2009.

[54] T. Gottschall, T. Meyer, M. Baumgartl, C. Jauregui, M. Schmitt, J. Popp, J. Limpert, and A. Tünnermann, "Fiber-based light sources for biomedical applications of coherent anti-stokes raman scattering microscopy," *Laser & Photonics Reviews*, vol. 9, pp. 435–451, 2015.

[55] W. Rock, M. Bonn, and S. H. Parekh, "Near shot-noise limited hyperspectral stimulated raman scattering spectroscopy using low energy lasers and a fast cmos array," *Optics Express*, vol. 21, pp. 15113–15120, 2013.

[56] W. Rock, M. Bonn, and S. H. Parekh, "Near shot-noise limited hyperspectral stimulated raman scattering spectroscopy using low energy lasers and a fast cmos array," *Optics Express*, vol. 21, pp. 15113–15120, 2013.

[57] A. Volkmer, L. D. Book, and X. S. Xie, "Time-resolved coherent anti-stokes raman scattering microscopy: imaging based on raman free induction decay," *Applied Physics Letters*, vol. 80, p. 1505, 2002.

[58] Y. J. Lee, S. H. Parekh, Y. H. Kim, and M. T. Cicerone, "Optimized continuum from a photonic crystal fiber for broadband time-resolved coherent anti-stokes raman scattering," *Optics Express*, vol. 18, pp. 4371–4379, 2010.

[59] J. D. Miller, M. N. Slipchenko, and T. R. Meyer, "Probe-pulse optimization for nonresonant suppression in hybrid fs/ps coherent anti-stokes raman scattering at high temperature," *Optics Express*, vol. 19, pp. 13326–13333, 2011.

[60] J. P. Ogilvie, E. Beaurepaire, A. Alexandrou, and M. Joffre, "Fourier-transform coherent anti-stokes raman scattering microscopy," *Optics Letters*, vol. 31, pp. 480–482, 2006.

[61] M. Cui, j. Skodack, and J. P. Ogilvie, "Chemical imaging with fourier transform coherent anti-stokes raman scattering microscopy," *Applied Optics*, vol. 47, pp. 5790–5798, 2008.

[62] K. Hashimoto, M. Takahashi, T. Ideguchi, and K. Goda, "Broadband coherent raman spectroscopy running at 24000 spectra per second," *Scientific Reports*, vol. 6, p. 21036, 2016.

[63] A. S. Duarte, C. Schnedermann, and P. Kukura, "Wide-field detected fourier transform cars microscopy," *Scientific Reports*, vol. 6, p. 37516, 2016.

[64] A. M. Weiner, *Ultrafast Optics*. John Wiely & Sons Publications, 2011.

[65] M. Y. Shverdin, D. R. Walker, D. D. Yavuz, G. Y. Yin, and S. E. Harris, "Generation of a single-cycle optical pulse," *Physical Review Letters*, vol. 94, p. 033904, 2005.

[66] S. A. Diddams, L. Hollberg, and V. Mbele, "Molecular fingerprinting with the resolved modes of a femtosecond laser frequency comb," *Nature*, vol. 445, pp. 627–630, 2007.

[67] L. Sherman, J. Y. Ye, O. Albert, and T. B. Norris, "Adaptive correction of depth-induced aberrations in multiphoton scanning microscopy using a deformable mirror," *Journal of Microscopy*, vol. 206, pp. 65–71, 2002.

[68] A. Cartella, S. Bonora, M. Först, G. Cerullo, A. Cavalleri, and C. Manzoni, "Pulse shaping in the mid-infrared by a deformable mirror," *Optics Letters*, vol. 39, pp. 1485–1488, 2014.

[69] A. M. Weiner, "Femtosecond pulse shaping using spatial light modulators," *Review of Scientific Instruments*, vol. 71, p. 1929, 2000.

[70] A. M. Weiner, "Ultrafast optical pulse shaping: A tutorial review," *Optics Communications*, vol. 284, pp. 3669–3692, 2011.

[71] B. von Vacano, T. Buckup, and M. Motzkus, "Highly sensitive single-beam heterodyne coherent anti-stokes raman scattering," *Optics Letters*, vol. 31, pp. 2495–2497, 2006.

[72] B. von Vacano and M. Motzkus, "Time-resolved two color single-beam cars employing supercontinuum and femtosecond pulse shaping," *Optics Communications*, vol. 264, pp. 488–493, 2006.

[73] S.-H. Lim, A. G. Caster, and S. R. Leone, "Fourier transform spectral interferometric coherent anti-stokes raman scattering (ftsi-cars) spectroscopy," *Optics Letters*, vol. 32, pp. 1332–1334, 2007.

[74] S.-H. Lim, A. G. Caster, O. Nicolet, and S. R. Leone, "Chemical imaging by single pulse interferometric coherent anti-stokes raman scattering microscopy," *Journal of Physical Chemistry B*, vol. 110, pp. 5196–5204, 2006.

[75] A. Wipfler, T. Buckup, and M. Motzkus, "Multiplexing single-beam coherent anti-stokes raman spectroscopy with heterodyne detection," *Applied Physics Letters*, vol. 100, p. 071102, 2012.

[76] O. Katz, A. Natan, Y. Silberberg, and S. Rosenwaks, "Standoff detection of trace amounts of solids by nonlinear raman spectroscopy using shaped femtosecond pulses," *Applied Physics Letters*, vol. 92, p. 171116, 2008.

[77] P. J. Wrzesinski, D. Pestov, V. V. Lozovoy, B. Xu, S. Roy, J. R. Gord, and M. Dantus, "Binary phase shaping for selective single-beam cars spectroscopy and imaging of gas-phase molecules," *Journal of Raman Spectroscopy*, vol. 42, pp. 393–398, 2011.

[78] A. Natan, O. Katz, S. Rosenwaks, and Y. Silberberg, "Single-pulse standoff nonlinear raman spectroscopy using shaped femtosecond pulses," *Proceedings of Ultrafast Phenomena XVI*, vol. 92, pp. 985–987, 2009.

[79] O. Katz, J. M. Levitt, E. Grinvald, and Y. Silberberg, "Single-beam coherent raman spectroscopy and microscopy via spectral notch shaping," *Optics Express*, vol. 18, pp. 22693–22701, 2010.

[80] A. Natan, J. M. Levitt, L. Graham, O. Katz, and Y. Silberberg, "Stand-off detection via single-beam spectral notch filtered pulses," *Applied Physics Letters*, vol. 100, p. 051111, 2012.

[81] Y. Shen, D. V. Voronin, A. V. Sokolov, and M. O. Scully, "Low wavenumber efficient single-beam coherent anti-stokes raman scattering using a spectral hole," *Optics Letters*, vol. 40, pp. 1223–1226, 2015. Reproduced with the permission of OSA Publishing.

[82] H. Li, D. A. Harris, B. Xu, P. J. Wrzesinski, V. V. Lozovoy, and M. Dantus, "Coherent mode-selective raman excitation towards standoff detection," *Optics Express*, vol. 16, pp. 5499–5504, 2008.

[83] H. Li, D. A. Harris, B. Xu, P. J. Wrzesinski, V. V. Lozovoy, and M. Dantus, "Standoff and arms-length detection of chemicals with single-beam coherent anti-stokes raman scattering," *Applied Optics*, vol. 48, pp. B17–B22, 2009.

[84] R. L. Fork, O. E. Martinez, and J. P. Gordon, "Negative dispersion using pairs of prisms," *Optics Letters*, vol. 9, pp. 150–152, 1984.

[85] L. Polachek, D. Oron, and Y. Silberberg, "Full control of the spectral polarization of ultrashort pulses," *Optics Letters*, vol. 31, pp. 631–633, 2006.

[86] K. R. Hall, R. C. Wilhoit, A. M. Ferguson, and L. B. Beach, *TRC Spectral Raman Data*. Thermodynamics Research Center, the Texas A& M University System, 1983.

[87] B. von Vacano, W. Wohlleben, and M. Motzkus, "Single-beam cars spectroscopy applied to low-wavenumber vibrational modes," *Journal of Raman Spectroscopy*, vol. 37, pp. 404–410, 2006.

[88] P. A. Mosier-Boss, S. H. Lieberman, and R. Newbery, "Fluorescence rejection in raman spectroscopy by shifted-spectra, edge detection, and fft filtering techniques," *Applied Spectroscopy*, vol. 49, pp. 630 – 638, 1995.

[89] L. Brückner, T. Buckup, and M. Motzkus, "Exploring the potential of tailored spectral focusing," *Journal of the Optical Society of America B*, vol. 33, pp. 1482–1491, 2016.

[90] J.-X. Cheng, A. Volkmer, L. D. Book, and X. S. Xie, "An epi-detected coherent anti-stokes raman scattering (e-cars) microscope with high spectral resolution and high sensitivity," *Journal of Physical Chemistry B*, vol. 105, pp. 1277–1280, 2001.

[91] F. Ganikhanov, C. L. Evans, B. G. Saar, and X. S. Xie, "High-sensitivity vibrational imaging with frequency modulation coherent anti-stokes raman scattering (fm cars) microscopy," *Optics Letters*, vol. 31, pp. 1872–1874, 2006.

[92] M. O. Scully, G. W. Kattawar, R. P. Lucht, T. Opatrný, H. Pilloff, A. Rebane, A. V. Sokolov, and M. S. Zubairy, "Fast cars: Engineering a laser spectroscopic technique for rapid identification of bacterial spores," *Proceedings of the National Academy of Sciences of the United States of America*, vol. 99, pp. 10994–11001, 2002.

[93] Y. Shen, D. V. Voronine, A. V. Sokolov, and M. O. Scully, "A versatile setup using femtosecond adaptive spectroscopic technique for coherent anti-stokes raman scattering," *Review of Scientific Instruments*, vol. 86, p. 083107, 2015. Reproduced with the permission of AIP Publishing.

[94] Y. Shen, D. V. Voronine, A. V. Sokolov, and M. O. Scully, "Single-beam heterodyne fast cars," *Optics Express*, vol. 24, pp. 21652–21662, 2016. Reproduced with the permission of OSA Publishing.

[95] T. Suzuki and K. Misawa, "Efficient heterodyne cars measurement by combining spectral phase modulation with temporal delay technique," *Optics Express*, vol. 19, pp. 11463–11470, 2011.

[96] P. Dhamelincourt, F. Allart, M. Leclercq, A. T. N'Guyen, and D. O. Landon, "Laser raman molecular microprobe (mole)," *Analytical Chemistry*, vol. 51, pp. 414A–421A, 1979.

[97] M. T. Bremer, P. J. Wrzesinski, N. Butcher, V. V. Lozovoy, and M. Dantus, "Highly selective standoff detection and imaging of trace chemicals in a complex background using single-beam coherent anti-stokes raman scattering," *Applied Physics Letters*, vol. 99, p. 101109, 2011.

[98] D. V. Voronine, A. M. Sinyukov, X. Hua, K. Wang, P. K. Jha, E. Munusamy, S. E. Wheeler, G. Welch, A. V. Sokolov, and M. O. Scully, "Time-resolved surface-enhanced coherent sensing of nanoscale molecular complexes," *Scientific Reports*, vol. 2, p. 891, 2012.

[99] B. Li, W. S. Warren, and M. C. Fischer, "Phase-cycling coherent anti-stokes raman scattering using shaped femtosecond laser pulses," *Optics Express*, vol. 18, pp. 25825–25832, 2010.

[100] B. C. Chen and S. H. Lim, "Optimal laser pulse shaping for interferometric multiplex coherent anti-stokes raman scattering microscopy," *Journal of Physical Chemistry B*, vol. 12, pp. 3653–3661, 2008.

[101] F. L. Galeener, R. A. Barrio, E. Martinez, and R. J. Elliott, "Vibrational decoupling of rings in amorphous solids," *Physical Review Letters*, vol. 53, p. 2429, 1984.

[102] P. D. Chowdary, Z. Jiang, E. J. Chaney, W. A. Benalcazar, D. L. Marks, M. Gruebele, and S. A. Boppart, "Molecular histopathology by spectrally reconstructed nonlinear interferometric vibrational imaging," *Cancer Research*, vol. 70, pp. 9562–9569, 2010.

[103] C.-S. Liao, M. N. Slipchenko, P. Wang, J. Li, S.-Y. Lee, R. A. Oglesbee, and J.-X. Cheng, "Microsecond scale vibrational spectroscopic imaging by multiplex stimulated raman scattering microscopy," *Light: Science & Applications*, vol. 4, p. e265, 2015.

[104] Y. Shen, A. A. Voronin, A. M. Zheltikov, S. P. O'Connor, V. V. Yakovlev, A. V. Sokolov, and M. O. Scully, "Picosecond supercontinuum generation in large mode area photonic crystal fibers for coherent anti-stokes raman scattering microspectroscopy," *Scientific Reports*, vol. 8, p. 9526, 2018. Licensed under a Creative Commons Attribution 4.0 International License.

[105] P. D. Maker, R. W. Terhune, and C. M. Savage, "Intensity-dependent changes in the refractive index of liquids," *Physical Review Letters*, vol. 12, pp. 507–509, 1964.

[106] G. A. Askaryan, "Effects of the gradient of a strong electromagnetic beam on electrons and atoms," *Journal of Experimental and Theoretical Physics*, vol. 15, pp. 1088–1090, 1962.

[107] R. L. Carman, R. Y. Chiao, and P. L. Kelly, "Observation of degenerate stimulated four-photon interaction and four-wave parametric amplification," *Physical Review Letters*, vol. 17, pp. 1281–1283, 1966.

[108] G. Eckhardt, R. W. Hellwarth, F. J. McClung, S. E. Schwarz, D. Weiner, and E. J. Woodbury, "Stimulated raman scattering from organic liquids," *Physical Review Letters*, vol. 9, pp. 455–457, 1962.

[109] R. R. Alfano and S. L. Shapiro, "Emission in the region 4000 to 7000 Å via four-photon coupling in glass," *Physical Review Letters*, vol. 24, pp. 592–594, 1970.

[110] R. R. Alfano, *The Supercontinuum Laser Source*. Springer, 2006.

[111] A. Hasegawa, "Generation of a train of soliton pulses by induced modulational instability in optical fibers," *Optics Letters*, vol. 9, pp. 288–290, 1984.

[112] E. M. Dianov, P. V. Mamyshev, A. M. Prokhorov, and V. N. Serkin, *Nonlinear Effects in Optical Fibres*. Harwood Academic Publishers, 1989.

[113] J. K. Ranka, R. S. Windeler, and A. J. Stentz, "Visible continuum generation in air-silica microstructure optical fibers with anomalous dispersion at 800 nm," *Opticsl Letters*, vol. 25, pp. 25–27, 2000.

[114] J. C. Knight, "Photonic crystal fibres," *Nature*, vol. 424, pp. 847–851, 2003.

[115] J. M. Dudley and J. R. Taylor, *Supercontinuum generation in optical fibers*. Cambridge University Press, 2010.

[116] A. B. Rulkov, M. Y. Vyatkin, S. V. Popov, J. R. Taylor, and V. P. Gapontsev, "High brightness picosecond all-fiber generation in 525-1800 nm range with picosecond yb pumping," *Optics Express*, vol. 13, pp. 377–381, 2005.

[117] J. M. Stone and J. C. Knight, "Visibly "white" light generation in uniform photonic crystal fiber using a microchip laser," *Optics Express*, vol. 16, pp. 2670–2675, 2008.

[118] J. H. V. Price, T. M. Monro, H. Ebendorff-Heidepriem, F. Poletti, P. Horak, V. Finazzi, J. Y. Y. Leong, P. Petropoulos, J. C. Flanagan, G. Brambilla, X. Feng, and D. J. Richardson, "Mid-ir supercontinuum from nonsilica microstructured optical fibers," *IEEE Journal of Selected Topics in Quantum Electronics*, vol. 13, pp. 738–749, 2007.

[119] A. Bozolan, C. J. S. deMatos, C. M. B. Cordeiro, E. M. dos Santos, and J. C. Travers, "Supercontinuum generation in a water-core photonic crystal fiber," *Optics Express*, vol. 16, pp. 9671–9676, 2008.

[120] P. S. J. Russell, P. Hölzer, W. Chang, A. Abdolvand, and J. C. Travers, "Hollow-core photonic crystal fibre for gas-based nonlinear optics," *Nature Photonics*, vol. 8, pp. 278–286, 2014.

[121] G. P. Agrawal, *Nonlinear Fiber Optics*. Academic Press, 2013.

[122] D. J. Jones, S. A. Diddams, J. K. Ranka, A. Stent, R. S. Windeler, J. L. Hall, and S. T. Cundiff, "Carrier-envelope phase control of femtosecond mode-locked lasers and direct optical frequency synthesis," *Science*, vol. 288, pp. 635–639, 2000.

[123] T. Udem, R. Holzwarth, and T. W. Hänsch, "Optical frequency metrology," *Nature*, vol. 416, pp. 233–237, 2002.

[124] H. Tu and S. A. Boppart, "Coherent fiber supercontinuum for biophotonics," *Laser Photonics Review*, vol. 7, pp. 628–645, 2013.

[125] H. Tu and S. A. Boppart, "Coherent anti-stokes raman scattering microscopy: overcoming technical barriers for clinical translation," *Journal of Biophotonics*, vol. 7, pp. 9–22, 2014.

[126] H. N. Paulsen, K. M. Hilligsøe, J. Thøgersen, S. R. Keiding, and J. J. Larsen, "Coherent anti-stokes raman scattering microscopy with a photonic crystal fiber based light source," *Optics Letters*, vol. 28, pp. 1123–1125, 2003.

[127] S. O. Konorov, D. A. Akimov, E. E. Serebryannikov, A. A. Ivanov, M. V. Alfimov, and A. M. Zheltikov, "Cross-correlation frequency-resolved optical gating coherent anti-stokes raman

scattering with frequency-converting photonic-crystal fibers," *Physical Review E*, vol. 70, p. 057601, 2004.

[128] A. F. Pegoraro, A. Ridsdale, D. J. Moffatt, Y. Jia, J. P. Pezacki, and A. Stolow, "Optimally chirped multimodal cars microscopy based on a single ti:sapphire oscillator," *Optics Express*, vol. 17, pp. 2984–2996, 2009.

[129] A. F. Pegoraro, A. Ridsdale, D. J. Moffatt, J. P. Pezacki, B. K. Thomas, L. Fu, L. Dong, M. E. Fermann, and A. Stolow, "All-fiber cars microscopy of live cells," *Optics Express*, vol. 17, pp. 20700–20706, 2009.

[130] M. Baumgartl, M. Chemnitz, C. Jauregui, T. Meyer, B. Dietzek, J. Popp, J. Limpert, and A. Tünnermann, "All-fiber laser source for cars microscopy based on fiber optical parametric frequency conversion," *Optics Express*, vol. 20, pp. 4484–4493, 2012.

[131] C. W. Freudiger, W. Yang, G. R. Holtom, N. Peyghambarian, X. S. Xie, and K. Q. Kieu, "Stimulated raman scattering microscopy with a robust fiber laser source," *Nature Photonics*, vol. 8, pp. 153–159, 2014.

[132] R. Selm, M. Winterhalder, A. Zumbusch, G. Krauss, T. Hanke, A. Sell, and A. Leitenstorfer, "Ultrabroadband background-free coherent anti-stokes raman scattering microscopy based on a compact er:fiber laser system," *Optics Letters*, vol. 35, pp. 3282–3284, 2010.

[133] H. Wang, T. B. Huff, and J.-X. Cheng, "Coherent anti-stokes raman scattering imaging with a laser source delivered by a photonic crystal fiber," *Optics Letters*, vol. 31, pp. 1417–1419, 2006.

[134] M. Balu, G. Liu, Z. Chen, B. J. Tromberg, and E. O. Potma, "Fiber delivered probe for efficient cars imaging of tissues," *Optics Express*, vol. 18, pp. 2380–2388, 2010.

[135] G. Genty, T. Ritari, and H. Ludvigsen, "Supercontinuum generation in large mode-area microstructured fibers," *Optics Express*, vol. 13, pp. 8625–8633, 2005.

[136] A. V. Mitrofanov, A. A. Ivanov, M. V. Alfimov, A. A. Podshivalov, and A. M. Zheltikov, "Microjoule supercontinuum generation by stretched megawatt femtosecond laser pulses in

a large-mode-area photonic-crystal fiber," *Optics Communications*, vol. 280, pp. 453–456, 2007.

[137] R. Cherif, M. Zghal, I. Nikolov, and M. Danailov, "High energy femtosecond supercontinuum light generation in large mode area photonic crystal fiber," *Optics Communications*, vol. 283, pp. 4378–4382, 2010.

[138] V. G. Savitski, K. V. Yumashev, V. L. Kalashnikov, V. S. Shevandin, and K. V. Dukel'skii, "Infrared supercontinuum from a large mode area pcf under extreme picosecond excitation," *Optical and Quantum Electronics*, vol. 39, pp. 1297–1309, 2007.

[139] R. Arora, G. I. Petrov, J. Liu, and V. V. Yakovlev, "Improving sensitivity in nonlinear raman microspectroscopy imaging and sensing," *Journal of Biomedical Optics*, vol. 16, p. 021114, 2011.

[140] V. P. Mitrokhin, A. B. Fedotov, A. A. Ivanov, M. V. Alfimov, and A. M. Zheltikov, "Coherent anti-stokes raman scattering microspectroscopy of silicon components with a photonic-crystal fiber frequency shifter," *Optics Letters*, vol. 32, pp. 3471–3473, 2007.

[141] G. I. Petrov and V. V. Yakovlev, "Enhancing red-shifted white-light continuum generation in optical fibers for applications in nonlinear raman microscopy," *Optics Express*, vol. 13, pp. 1299–1306, 2005.

[142] C. Heinrich, S. Bernet, and M. Ritsch-Marte, "Wide-field coherent anti-stokes raman microscopy," *Applied Physics Letters*, vol. 84, pp. 816–818, 2004.

[143] A. A. Voronin and A. M. Zheltikov, "Subcycle solitonic breathers," *Physical Review A*, vol. 90, p. 043807, 2014.

[144] "Large mode area photonic crystal fibers." https://www.nktphotonics.com/lasers-fibers/product/large-mode-area-photonic-crystal-fibers/, 2018.

[145] A. A. Voronin and A. M. Zheltikov, "Nonlinear dynamics of high-power ultrashort laser pulses: exaflop computations on a laboratory computer station and subcycle light bullets," *Physics-Uspekhi*, vol. 59, pp. 869–877, 2016.

[146] G. I. Petrov, V. V. Yakovlev, and N. I. Minkovski, "Broadband continuum-generation of the output of high-energy diode-pumped picosecond laser," *Optics Communications*, vol. 229, pp. 441–445, 2004.

[147] N. Ishii, C. Y. Teisset, S. Köhler, E. E. Serebryannikov, T. Fuji, T. Metzger, F. Krausz, A. Baltuška, and A. M. Zheltikov, "Widely tunable soliton frequency shifting of few-cycle laser pulses," *Physical Review E*, vol. 74, p. 036617, 2006.

[148] B. Wetzel, A. Stefani, L. Larger, P. A. Lacourt, J. M. Merolla, T. Sylvestre, A. Kudlinski, A. Mussot, G. Genty, F. Dias, and J. M. Dudley, "Real-time full bandwidth measurement of spectral noise in supercontinuum generation," *Scientific Reports*, vol. 2, p. 882, 2012.

[149] R. P. Lucht, "Three-laser coherent anti-stokes raman scattering measurements of two species," *Optics Letters*, vol. 12, pp. 78–80, 1987.

[150] J. O. Orwa, I. Aharonovich, F. Jelezko, G. Balasubramanian, P. Balog, M. Markham, D. J. Twitchen, A. D. Greentree, and S. Prawer, "Nickel related optical centres in diamond created by ion implantation," *Journal of Applied Physics*, vol. 107, p. 093512, 2010.

[151] T. Ganz, V. Pervak, A. Apolonski, and P. Baum, "16 fs, 350 nj pulses at 5 mhz repetition rate delivered by chirped pulse compression in fibers," *Optics Letters*, vol. 36, pp. 1107–1109, 2011.

[152] J. H. Richardson, *Handbook for the light microscope*. Noyes Publications, 1991.

[153] C. Heinrich, A. Hofer, A. Ritsch, C. Ciardi, S. Bernet, and M. Ritsch-Marte, "Selective imaging of saturated and unsaturated lipids by wide-field cars microscopy," *Optics Express*, vol. 16, pp. 2699–2708, 2008.

[154] I. Toytman, D. Simanovskii, and D. Palanker, "On illumination schemes for wide-field cars microscopy," *Optics Express*, vol. 17, pp. 7339–7347, 2009.

[155] A. Silve, N. Dorval, T. Schmid, L. M. Mir, and B. Attal-Tretout, "A wide-field arrangement for single-shot cars imaging of living cells," *Journal of Raman Spectroscopy*, vol. 43, pp. 644–650, 2012.

[156] M. Lei, M. Winterhalder, R. Selm, and A. Zumbusch, "Video-rate wide-field coherent anti-stokes raman scattering microscopy with collinear nonphase-matching illumination," *Journal of Biomedical Optics*, vol. 16, p. 021102, 2011.

[157] Y. Shen, J. Wang, K. Wang, A. V. Sokolov, and M. O. Scully, "Wide-field coherent anti-stokes raman scattering microscopy based on picosecond supercontinuum source," *APL Photonics*, vol. 3, p. 116104, 2018. Licensed under a Creative Commons Attribution (CC BY) license.

[158] H. Lei, Z. Liu, C. He, S.-C. Zhang, Y.-Q. Liu, C.-J. Hua, X.-M. Li, F. Li, C.-M. Chen, and R. Cai, "Graphene enhanced low-density polyethylene by pretreatment and melt compounding," *Royale Society of Chemistry Advances*, vol. 6, p. 101492, 2016.

[159] "The human metabolome database." http://www.hmdb.ca/metabolites/HMDB0000192, 2018.

[160] M. Okuno, H. Kano, P. Leproux, V. Couderc, and H. Hamaguchi, "Quantitative coherent anti-stokes raman scattering microspectroscopy using a nanosecond supercontinuum light source," *Optical Fiber Technology*, vol. 18, pp. 388–393, 2012.

[161] A. Bohlin and C. J. Kliewer, "Single-shot hyperspectral coherent raman planar imaging in the range 0-4200 cm^{-1}," *Applied Physics Letters*, vol. 105, p. 161111, 2014.

[162] J. N. Bixler, B. H. Hokr, M. L. Denton, G. D. Noojin, A. D. Shingledecker, H. T. Beier, R. J. Thomas, B. A. Rockwell, and V. V. Yakovlev, "Assessment of tissue heating under tunable near-infrared radiation," *Journal of Biomedical Optics*, vol. 19, p. 070501, 2014.

[163] N. Djaker, D. Gachet, N. Sandeau, P.-F. Lenne, and H. Rigneault, "Refractive effects in coherent anti-stokes raman scattering microscopy," *Applied Optics*, vol. 45, pp. 7005–7011, 2006.

[164] J. van der Kolk, A. C. Lesina, and L. Ramunno, "Effects of refractive index mismatch on srs and cars microscopy," *Optics Express*, vol. 24, pp. 25752–25766, 2016.

[165] E. Ploetz, B. Marx, T. Klein, R. Huber, and P. Gilch, "A 75 mhz light source for femtosecond stimulated raman microscopy," *Optics Express*, vol. 21, pp. 18612–18620, 2009.

[166] Z. Meng, G. I. Petrov, and V. V. Yakovlev, "Pure electrical, highly-efficient and sidelobe free coherent raman spectroscopy using acousto-optics tunable filter (aotf)," *Scientific Reports*, vol. 6, p. 20017, 2016.

[167] M. Zhi, K. Wang, X. Hua, and A. V. Sokolov, "Pulse-shaper-assisted phase control of a coherent broadband spectrum of raman sidebands," *Optics Letters*, vol. 36, pp. 4032–4034, 2011.

[168] J. Rehbinder, L. Brückner, A. Wipfler, T. Buckup, and M. Motzkus, "Multimodal nonlinear optical microscopy with shaped 10 fs pulses," *Optics Express*, vol. 22, pp. 28790–28797, 2014.

[169] B. Schenkel, J. Biegert, U. Keller, C. Vozzi, M. Nisoli, G. Sansone, S. Stagira, S. D. Silvestri, and O. Svelto, "Generation of 3.8-fs pulses from adaptive compression of a cascaded hollow fiber supercontinuum," *Optics Letters*, vol. 28, pp. 1987–1989, 2003.

[170] A. Knebl, D. Yan, J. Popp, and T. Frosch, "Fiber enhanced raman gas spectroscopy," *TrAC Trends in Analytical Chemistry*, vol. 103, pp. 230–238, 2018.

[171] A. B. Fedotov, S. O. Konorov, V. P. Mitrokhin, E. E. Serebryannikov, and A. M. Zheltikov, "Coherent anti-stokes raman scattering in isolated air-guided modes of a hollow-core photonic-crystal fiber," *Physical Review A*, vol. 70, p. 2004, 2004.

[172] B. M. Trabold, R. J. R. Hupfer, A. Abdolvand, and P. S. J. Russell, "Broadband high-resolution multi-species cars in gas-filled hollow-core photonic crystal fiber," *Optics Letters*, vol. 42, pp. 3283–3286, 2017.